Title
The Effectiveness of EMIC Wave-Driven Relativistic Electron Pitch Angle Scattering in Outer Radiation Belt Depletion

Author
Adair, Lydia

Publication Date
2021

UNIVERSITY OF CALIFORNIA
Los Angeles

The Effectiveness of EMIC Wave-Driven Relativistic Electron Pitch Angle Scattering in Outer Radiation Belt Depletion

A dissertation submitted in partial satisfaction
of the requirements for the degree
Doctor of Philosophy in Geophysics and Space Physics

by

Lydia Alexandra Adair

2021

ABSTRACT OF THE DISSERTATION

The Effectiveness of EMIC Wave-Driven Relativistic Electron Pitch Angle Scattering in Outer Radiation Belt Depletion

by

Lydia Alexandra Adair
Doctor of Philosophy in Geophysics and Space Physics
University of California, Los Angeles, 2021
Professor Vassilis Angelopoulos, Chair

The dynamic variability of Earth's outer radiation belt is due to the competition among various particle transport, acceleration, and loss processes. The following dissertation investigates electron resonance with Electromagnetic Ion Cyclotron (EMIC) waves as a potentially dominant mechanism driving relativistic electron loss from the radiation belts. EMIC waves have been previously studied as contributors to relativistic electron flux depletion. However, assumed limitations on the pitch angle and energy ranges within which scattering takes place leave uncertainties regarding the capability of the mechanism to explain sudden loss of core electron populations of the outer radiation belt. By introducing new methods to analyze EMIC wave-driven scattering signatures and relativistic electron precipitation events through a multi-point observation approach, this dissertation reveals the effectiveness of EMIC waves to drive losses of outer radiation belt electrons with a new resolution.

The research that composes this dissertation focuses on three key areas of the EMIC wave-relativistic electron relationship. A chapter comparing a single EMIC wave event with a pitch angle scattering signature shows that these waves can cause scattering of electrons at energies and pitch angles predicted by the wave-particle resonance condition. This initial study establishes the motivation and methodological groundwork for a statistical study which provides evidence for the common occurrence of these scattering signatures and shows that the energies and pitch angles affected by EMIC waves are often within the core radiation belt population.

A subsequent study then links scattering signatures to observations of relativistic electron precipitation events, revealing a significant coincidence rate between EMIC waves and precipitation events.

These three investigations together provide the first quantifiable tracing of relativistic electron precipitation events back to the driving EMIC wave, through verified scattering signatures. The results support EMIC wave-relativistic electron resonant interaction theory and provide strong quantitative evidence that EMIC waves can effectively drive losses of core radiation belt electrons.

The new knowledge gained here benefits the space physics community by informing space weather modelers and forecasters of the conditions that increase the efficiency of EMIC wave-driven radiation belt losses, and by introducing new and effective ways of identifying and analyzing EMIC wave-driven scattering to be used in future investigations.

The dissertation of Lydia Alexandra Adair is approved.

Marco Velli

Jacob Bortnik

Christopher Russell

Vassilis Angelopoulos, Committee Chair

University of California, Los Angeles

2021

To Nick, may we keep dreaming together

TABLE OF CONTENTS

LIST OF FIGURES

LIST OF TABLES

ACKNOWLEDGMENTS

The list of individuals whom, whether directly or indirectly, played a role in my educational journey culminating with this completed dissertation is innumerable. My gratitude is immense. First, my advisor, Vassilis Angelopoulos, is credited for granting me the opportunity to study and research with him. Vassilis's support was instrumental in helping me achieve my goals. Throughout the years, Vassilis encouraged me to pursue my scientific interests, challenged me to improve my research capabilities, and was a consistent advocate for my success. I was incredibly fortunate to learn from him, as well as from each member of my committee. I thank Professor Christopher Russell for being an inspirational and entertaining educator, who had me excited to attend his lectures and journal clubs. I always knew that by sitting in a room with Professor Russell I had an opportunity to learn something new that I did not expect, whether it be a story about a successful space mission or a little fact about our solar system that I wouldn't find in a textbook. I similarly looked forward to my classes with Professor Marco Velli, who gave me one of the best pieces of advice throughout my entire education: to work on my math skills. While it sounds an obvious piece of advice, it was an encouraging turning point for me to have Marco take the time and effort to discover where I needed help as a student and then communicate it to me. My appreciation also goes to Professor Jacob Bornik, whose passion and excitement for my research topic was great encouragement. Jacob's feedback on all my seminar presentations and papers was priceless.

My education in space physics continued outside the classroom, and I had many teachers of many formats. One of my favorite experiences in graduate school was studying for my qualifying exam with Ray Walker. Being quizzed on every possible space physics topic with just a dry erase marker and a whiteboard in front of me was terrifying, but Ray's positive energy and understanding got me through it (and I'll never forget the generalized Ohm's Law ever again). Much of my education came from Xiaojia Zhang, who gave me some much-needed IDL tutoring, and helped me to early on sort through the vast literature on EMIC waves to see where my work might fit in. I also learned a great deal from David Sibeck when I went to work with him each summer at NASA's Goddard Space Flight Center. While his endless advice, the introductions he made for me to others at GSFC, and his proofreading of my papers, likely were of most benefit to me, I think what I will be most fond of from my time at NASA was his delicious blueberry and blackberry cobbler. My time at NASA served as a springboard, getting me to dive into my research and make important connections to other researchers. It was during my first trip that I met Alexa Halford, who helped me draft my first paper and got me excited about where my thesis would go next. Back at UCLA, I am grateful to all the EPSS students that I had the fortune to study with. I am convinced that part of the mental fortitude needed to finish a PhD dissertation comes from an odd sense of shared pain, anxiety, and frustration that you have with your classmates. I am especially appreciative to Emily Hawkins who so patiently explained graduate division processes, gave advice for my exams, and let me vent for many more hours than was reasonably productive.

I don't suppose it happens very often that one can pinpoint a moment in their life that they can look back at and think "If this had happened a fraction of a second later, I wouldn't be where I am today," but I definitely can. It was April 2014, and I hadn't yet figured out what my path would be when I finished my bachelor's degree. I'd be lying if I said that lack of certainty only made me slightly nervous. I was walking down a hall in the Geology building, heading to my part-time job, when an old friend of mine that I hadn't seen or spoken to in at least a year (probably more), stepped outside of one of the rooms. Chris Shaffer saw me, and seemingly unprompted said to me "Hey Lydia, want to build a satellite?" Long story short, I joined UCLA's first student-led satellite project, ELFIN, became the Mission Operations Lead, and later the Project Manager, working under Vassilis Angelopoulos. So, my thanks go to Chris, for stepping out of the EPSS Main Office at the precise moment that I was heading down the hall and shouting an incredibly random question at me. Besides for introducing me to my future graduate advisor, my time at ELFIN found me some lifelong friends that helped keep my sanity intact throughout working on my dissertation. Anthony Gildemeister was single-handedly responsible for keeping me caffeinated during my first two years of graduate school, making sure to drag me away from my computer regularly and take me to SEAS Café. For the caffeine, for the talks, for keeping an eye out for my emotional and mental well-being, Anthony was truly part of my critical support structure.

One of the greatest blessings in my life is that I have always had a family support structure. It may not have always been conventional, or simple, and it has shifted, adjusted, and moved around, but I have always had exactly what I've needed through each phase of my life. I recognize that my accomplishments are in part due to the love, guidance, and support of these individuals. I thank my dad, Craig, for igniting my passion for space and science. I cherish my memories of star gazing, looking through a telescope at the Milky Way, and talking for hours upon hours about black holes, space travel, and the terrifying vastness of the universe with him. I thank him for pushing me to sign up for AP Physics in high school, when all my teachers told me not to. I thank him for not being disappointed when I came home with a B+ in pre-calculus, but instead telling me he knew I could do better. I thank him for suggesting I look into studying Astrophysics at university, even though I had no idea what that was. I don't know why my dad thought that the daughter of two liberal arts educators would excel in science, but the greatest thing he ever gave me was the confidence that he was correct. That confidence was also developed with help from my older brother, Ford. While growing up together, he always had a unique way of lifting me up, while keeping me grounded. He'd made it known to me that he believed I had endless potential, but in the next breath would make fun of me for being a dork. As a young child, much of what I ever wanted was for my cool, smart, talented older brother to be proud of me, which proved to be a great motivator for my early academic pursuits. As I began my graduate work, I learned the priceless lesson that with some challenges, motivation isn't enough. Sometimes one needs to stop being stubbornly independent and learn to rely on others. When this happens, one couldn't do better than to have an Adair in their corner. My father-in-law, Warren Adair, and mother-in-law, Tomi Adair, are the definition of dependable. When I had to start commuting to campus, Warren helped me navigate buying my first car, and then took it in for countless car washes, oil changes, and tune-ups so that I could focus on my research and not worry so much about mundane chores. When I was stressed, Tomi encouraged me to take guilt free girl time, took care of my laundry, and brought me Starbucks. When I was sick, both Tomi and Warren dropped everything without question to get me the help I needed, so I could heal and get back to my dissertation. More times than I could count, the Adair's lent me a hand when mine were full, and I cannot express my gratitude enough. Another lesson I learned throughout my graduate adventure was the importance of fun. On occasion, stepping away from work for a half an hour, or a weekend, is actually a good thing! I was begrudgingly forced by Jeff Green to do this from time to time. In between exams, research papers, and seminars, Jeff made sure my time was filled with Go Kart races, Krav Maga lessons, cooking challenges, Nerf battles, giant chess, pickleball, and cheesy movies. I thank Jeff for teaching me that it's okay to continue being a kid while navigating becoming an adult. Because of him, when I look back at my time working on my dissertation, the memories of laughter and fun will outshine those of hours of studying and stressing. For these adventures, I am grateful to Jeff and of course, his partner-in-crime, my mother, Anne Green. Because of her, I understand what is meant by the word unconditional. For spending hours reading my chapters and teaching me how to use commas and apostrophes, I am appreciative. For picking up every phone call (no matter how early in the morning), for every piece of life advice, and for every hug I needed but never asked for, I am thankful. For the unconditional love throughout this journey, I am grateful. Finally, I'd like to thank my best friend and husband, Nick Adair, who deserves so much credit for helping me complete this dissertation. From cups of tea for calming my anxiety before exams, and words of encouragement when I couldn't see the light at the end of the tunnel, to holding on to faith in my capabilities when I started to lose that faith myself, Nick never stopped pushing me towards my goal. I may be biased, but I know with complete certainty that I am the most fortunate woman on Earth to be married to a man who cares so much about my dreams, that he makes them his own as well.

This dissertation was supported by NASA Grant NNX17AB67H. I acknowledge the support of Van Allen Probes and THEMIS for online access of data and analysis tools. Specifically, we acknowledge Van Allen Probe REPT and MagEIS data obtained from http://www.rbsp-ect.lanl.gov/data_pub/ and EMFISIS data obtained from

https://emfisis.physics.uiowa.edu/data/index, as well as THEMIS FGM data obtained at http://themis.ssl.berkeley.edu/themisdata/. Data access and processing was done using SPEDAS V3.1, see (Angelopoulos et al., 2019). I also thank W. Kurth at University

of Iowa for access to Van Allen Probe EMFISIS data, and G. Reeves at LANL for access to LANL/GOES data (https://rbsp-ect.lanl.gov/data_pub/LANL-GEO/), as well as D. Baker, B. Blake and C. Kletzing for Van Allen Probe Data. Finally, I thank the Space Physics Data Facility at NASA Goddard for providing OMNI data used in this study (https://omniweb.gsfc.nasa.gov/).

Chapter 2 is a version of Bingley et al. (2019), The Evolution of a Pitch-Angle Bite Out Scattering Signature Caused by EMIC Activity: A Case Study, Journal of Geophysical Research: Space Physics, 124. DOI: 10.1029/2018JA026292.

Chapter 3 is a version of Adair et al. (2020), A Statistical Examination of EMIC Wave-Driven Electron Pitch Angle Scattering Signatures, submitted to Journal of Geophysical Research: Space Physics.

Chapter 4 is a version of Adair et al. (2021), Relativistic Electron Precipitation Associated with Equatorial EMIC Wave-Driven Scattering Signatures, to be submitted to Journal of Geophysical Research: Space Physics.

VITA

2015	Bachelor of Science in Astrophysics, University of California, Los Angeles, California, USA.
2016-2020	Aeronautics Scholarship and Advanced STEM Training and Research Fellow, National Aeronatics and Space Administration
2019	Master of Science in Geophysics and Space Physics, University of California, Los Angeles, California, USA

PUBLICATIONS

Adair, L., Angelopoulos, V., Sibeck, D., Zhang, X. (2020). A Statistical Examination of EMIC Wave-Driven Electron Pitch Angle SCattering Signatures. Submitted to: Journal of Geophysical Research: Space Physics.

Angelopoulos, V., Tsai, E., **Bingley, L.** et al. The ELFIN Mission. Space Sci Rev 216, 103 (2020). https://doi.org/10.1007/s11214-020-00721-7

Bingley, L., Angelopoulos, V., Sibeck, D., Zhang, X., & Halford, A. (2019). The evolution of a pitch-angle "bite-out" scattering signature caused by EMIC wave activity: A case study. Journal of Geophysical Research: Space Physics, 124. https://doi.org/10.1029/2018JA026292.

Bingley, L., Angelopoulos, V., Sibeck, Baker, D., Spence, H., Kletzing, C. (2019). SM44B-05: Characterization of Relativistic Electron Scattering Signatures Caused by EMIC Waves. American Geophysical Union 2019 Fall Meeting, San Francisco CA, USA. Oral Presentation.

Bingley, L., Angelopoulos, V., Sibeck, D., Zhang, X., Halford, A. (2018). SM43D-3597: The Effectiveness of Relativistic Electron Pitch-Angle Scattering by EMIC Waves. American Geophysical Union 2018 Fall Meeting, Washington DC, USA. Poster Presentation.

Bingley, L., Angelopoulos, V., Sibeck, D., Zhang, X., Halford, A. (2017). SM51B-2443: A Statistical Examination of the Effect of EMIC Waves on Relativistic Electron Pitch-Angle Distributions. American Geophysical Union 2017 Fall Meeting, New Orleans LA, USA. Poster Presentation.

CHAPTER 1

Introduction

1.1 Motivation

As human exploration expands into the cosmos, the importance of understanding the near-Earth space environment to a point of accurate space weather forecasting has grown considerably. Since the mid-20th century, the region between the edge of Earth's atmosphere and the outer boundary of the magnetosphere[1] has become home to a multitude of spacecraft serving a variety of purposes. Many of these, including critically important Global Positioning System (GPS) satellites, communication satellites, Earth observing platforms, and various national defense assets, reside in or traverse the region of damaging high energy plasma known as the Van Allen Radiation Belts. The increased reliance on these space-based technologies, composed of electronics that are highly susceptible to risks introduced by unpredictable space weather, demands improved understanding of the physical processes driving the space environment.

The Van Allen Radiation Belts are important to investigate because they undergo significant variation in particle flux, intensity, and boundary location in response to different drivers. This variability is somewhat unpredictable, owing to a complex balance of particle acceleration, transport, and loss processes (Baker et al., 1986, 1994; Reeves, 1998; Reeves et al., 2003; Miyoshi & Kataoka, 2005; Turner et al., 2012). Of particular importance is the loss of relativistic electrons (the so called "killer" electrons), which are notorious for causing single event effects (SEEs) often leading to partial or total spacecraft system fail-

---

[1] The magnetosphere is the region of space where the dominant magnetic field is due to Earth's magnetic dipole.

ure. Electromagnetic ion cyclotron (EMIC) waves have been investigated as a likely major contributor to relativistic electron flux depletion due to their ability to resonate with and scatter $\geq$˜0.5 MeV relativistic electrons, causing them to be lost from the radiation belts (Thorne & Kennel, 1971; Horne & Thorne, 1998). While much progress has been made in characterizing the occurrence of EMIC waves in relation to radiation belt flux depletion events, much about the effectiveness of this process remains unknown.

Quantitatively characterizing relativistic electron loss by EMIC waves is necessary for improved resolution of radiation belt dynamics. The work presented in this dissertation contributes new understanding regarding the effectiveness of EMIC waves in influencing radiation belt electron loss by both identifying and characterizing scattering signatures and resultant precipitation caused by them. A comprehensive understanding of this loss process can greatly improve space weather modelling and forecasting capabilities which will inform current and future protection systems for critical space, air, and ground assets.

This chapter provides a background to EMIC wave-driven relativistic electron loss and introduces the concepts that are central to the mechanisms explored throughout this dissertation. First, the Van Allen Radiation Belts are described along with the physical principles that govern them. Second, the plasma phenomenon of the electromagnetic ion cyclotron wave is introduced, including a summary of the wave generation mechanism and typical wave characteristics. Third, a review of current understanding of the connection between EMIC waves and the radiation belts is included.

1.2 Background

1.2.1 The Radiation Belts

The structure of high energy particles trapped by Earth's magnetosphere was first observed in 1958 by the Pioneer 3 spacecraft (Van Allen & Frank, 1959), and has since been the subject of intense scientific interest. Separated by an empty slot region are two toroidal "belts" of particles (see Figure 1.1): an inner belt that is typically located below an altitude of 2.5 Earth radii (RE) and is mainly composed of multi-megaelectronvolt (MeV) energy protons and kiloelectronvolt (keV) electrons, and an outer belt between 3 and 7 RE, which is dominated by MeV electrons. The McIlwain L-parameter (McIlwain, 1961), or L-shell (see Equation 1.1 and Figure 1.4), is used to describe a region of the magnetosphere described by the magnetic field lines.

$$R = L \cos^2 \lambda \tag{1.1}$$

In contrast to the relatively stable inner belt (Baker et al., 2007), the outer radiation belt has been characterized as highly variable, with particle fluxes and intensities changing drastically on timescales ranging from hours to days (Williams & Smith, 1965; Paulikas & Blake, 1979; Reeves et al., 2003). While the outer belt contains both high energy protons and electrons spanning a large energy range, the core populations are often considered to be electrons with an energy of ≤ 2 MeV (Vette, 1991). The locations and intensities of these belts are controlled by a competition between particle acceleration, transport, and loss processes. Scattering of relativistic electrons by EMIC waves is just one of the different ways a particle can become lost.

From the fundamentals of electromagnetism, it is known that a charged particle will have its path influenced by a surrounding magnetic field. The Lorentz force, given by Equation 1.2, describes how a particle with charge q and velocity v is influenced by the surrounding electromagnetic field. Its trajectory can be described by the angle between the background magnetic field, $\hat{B}$, and the particle's velocity vector (see Figure 1.3, Equation 1.3).

$$F = q\left(E + v \times B\right) \tag{1.2}$$

$$\tan \alpha = \frac{v_\perp}{v_\parallel} \tag{1.3}$$

For radiation belt electrons, the Earth's magnetic field governs three periodic motions: gyromotion around magnetic field lines, bounce motion between magnetic mirror points, and drift motion due to the curvature of the Earth's magnetic field (see Figure 1.2). These motions are preserved if changes to the background magnetic field occur on time scales and

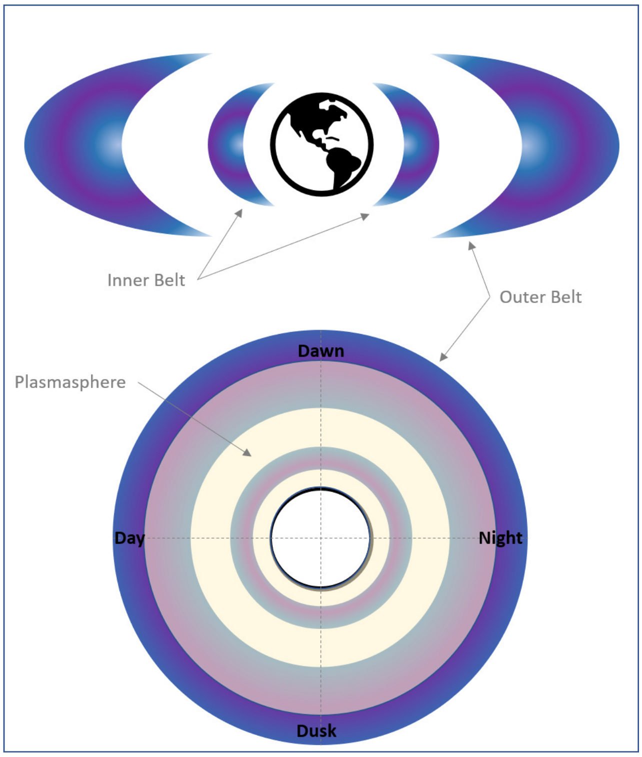

Figure 1.1: (Top) Side view representation (not to scale) of inner and outer radiation belts. (Bottom) Top view representation (not to scale) of inner and outer radiation belts, showing the overlap with the plasmasphere (yellow shaded region).

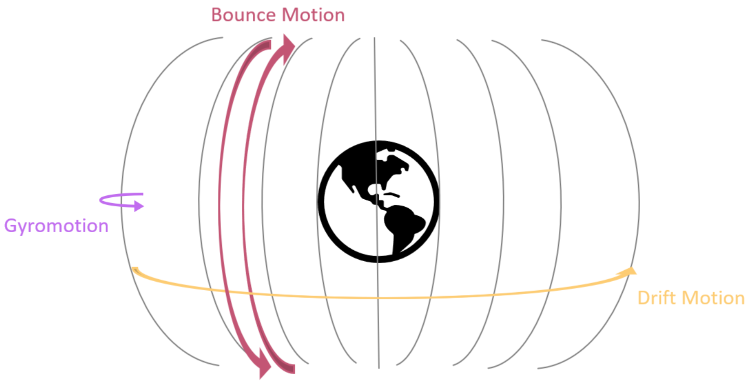

Figure 1.2: Three governing periodic motions of particles in the radiation belts: gyromotion around the magnetic field line, bounce motion between the magnetic poles, and azimuthal drift.

spatial scales greater than the periodic motion of the particle, resulting in the three adiabatic invariants: the magnetic moment, μ; the longitudinal invariant, J; and the total magnetic flux enclosed by a drift path, ϕ. Irreversible changes in the total particle flux content of the radiation belts can occur when one or more of these is not preserved. Thorne and Kennel (1971) proposed the gyroresonant interaction of electromagnetic ion cyclotron (EMIC) waves with relativistic electrons as a potential mechanism for rapid relativistic electron precipitation from the radiation belts due to a violation of the first adiabatic invariant. The change in μ occurs because the particle observes the magnetic field component of the EMIC wave on timescales shorter than the gyromotion (Tsurutani & Lakhina, 1997). During this gyroresonant interaction, the electron experiences a $v \times B$ Lorentz force, resulting in a change in the pitch angle. This pitch angle scattering can cause trapped particles to become removed from the radiation belts on short timescales (Summers & Thorne, 2003; Summers et al., 2007a; Omura & Zhao, 2012, 2013), which can contribute to the global variability of the radiation belts.

1.2.2 EMIC Wave Excitation and Occurrence

EMIC waves are left handed (L-mode) circularly polarized transverse electromagnetic waves that become excited in the magnetosphere due to hot ($>$ 100 eV) anisotropic ($T_{\parallel} > T_{\perp}$)

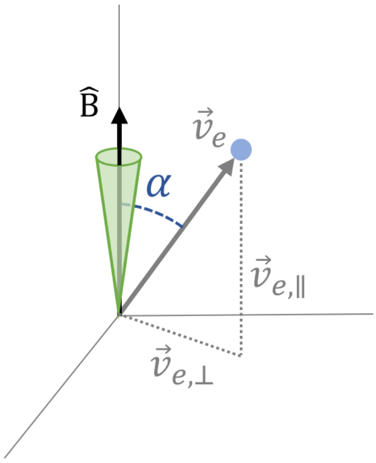

Figure 1.3: A particle's pitch angle, α, is the angle between the particle's velocity $\vec{v}_e$, composed of parallel ($\vec{v}_{e,\|}$) and perpendicular ($\vec{v}_{e,\perp}$) components, and the background magnetic field, $\hat{B}$. The loss cone (green) is the set of pitch angles that will result in loss from the magnetosphere.

proton distributions. These anisotropic distributions are often driven by injection of plasma from the magnetotail (Remya et al., 2020), but can also be driven by dayside magnetospheric compressions as a result of increased solar wind pressure (Cornwall, 1965; Thorne et al., 1974; Fraser et al., 2006; Remya et al., 2018). The waves can be generated in three frequency bands, hydrogen (H+), helium (He+), and oxygen (O+), each defined as the frequency region below the local ion gyrofrequency. Though typically generated near the magnetic equator, the waves can propagate down to lower latitudes, where they are detectable by ground magnetometers as Pc1-2[2] geomagnetic pulsations (Pickett et al., 2010). EMIC wave propagation is often described by cold plasma theory, which assumes a cold (few eV) uniform plasma. In this case, a parallel propagating wave in a multi-species plasma is represented by the dispersion relation (Equation 1.4), where $\omega_{(pe,j)}$ and $\Omega_{(e,j)}$ represent the species plasma frequency and gyrofrequency, respectively, and ω is the wave frequency with wave vector k. This dispersion relation describes the excitation of EMIC waves in three distinct frequency bands, separated by stop-bands around the ion gyrofrequencies where wave propagation is

---

[2] Pc1-2 waves have frequencies $f = 0.1 - 5$ Hz(Jacobs et al., 1964).

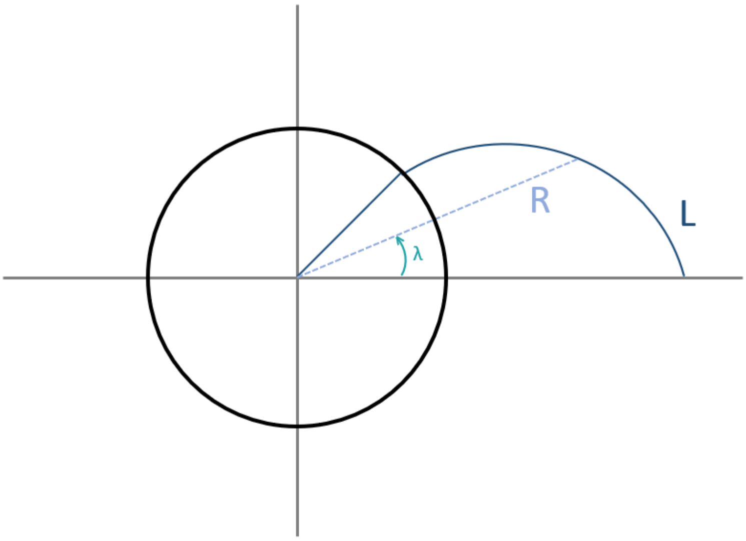

Figure 1.4: L-shell describes a set of magnetic field lines described by R, the radial distance of the field line and λ, the geomagnetic latitude.

not allowed. As the frequency of an EMIC wave approaches the ion gyrofrequency, the wave vector k approaches infinity. This description of the generation and propagation of EMIC waves is complicated by the presence of hot plasma, which can lead to inaccuracies in the cold plasma approximation (CPA)[3](Jordanova et al., 1996; Chen et al., 2011; Silin et al., 2011; Chen et al., 2013).

While the probability of EMIC wave occurrence extends over a wide range of magnetic local times (MLT) and L-shells (Halford et al., 2010, 2016; Min et al., 2012; D. Wang et al., 2015), the pre-midnight to dusk plasmapause (see Figure 1.1) is often considered the preferred region for EMIC wave excitation (Fraser et al., 1996; Meredith et al., 2003; Yuan et al., 2010). This region is where cold dense plasma in a relatively low background magnetic field overlaps with hot anisotropic ions being injected from the tail region of the magnetosphere, supporting growth of the plasma instability (Cornwall et al., 1970; Horne & Thorne, 1993; Morley et al., 2009; Fraser & Nguyen, 2001). Statistical surveys have revealed that EMIC waves are most often excited in the He+ and H+ bands, and the occurrence rate

---

[3] see Appendix A: Supplemental Information for a discussion about using the CPA.

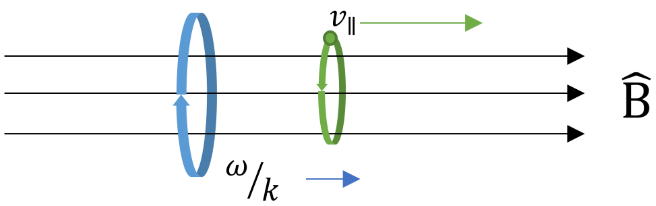

Figure 1.5: Anomalous gyroresonance between electrons and EMIC waves occurs when the electron has a parallel velocity $v_\parallel$ greater than the wave phase velocity $\frac{\omega}{k}$ so that the electron overtakes the wave.

and intensities of these waves are higher during geomagnetic storms than during quiet times (Halford et al., 2010; Fraser et al., 2010; Keika, 2013; H. Wang et al., 2019). In fact, sudden losses of radiation belt electrons have frequently occurred during geomagnetic storms, linking these loss events to EMIC waves (Bortnik et al., 2006).

$$\frac{c^2k^2}{\omega^2} = 1 - \frac{\omega_{pe}^2}{\omega(\omega + |\Omega_e|)} - \sum_{j=1}^{3} \frac{\omega_{pj}^2}{\omega(\omega - \Omega_j)} \tag{1.4}$$

1.2.3 Gyroresonant Interaction and Particle Scattering

In a plasma, charged particles can exchange energy with electromagnetic waves through resonant interactions. These interactions can occur when a particle that is gyrating about a background magnetic field observes the electric field component of a wave rotating at its own frequency and at the same rotational sense (polarization) (Gendrin, 1983). This standard gyroresonance occurs between EMIC waves and ions that have energies in the tens of keV range. As electrons gyrate in a right-handed sense, and EMIC waves have a left-handed polarization (L-mode), standard gyroresonance does not occur. If, however, electrons have relativistic energies such that electrons have a large enough velocity parallel to the background magnetic field to overtake the wave (see Figure 1.5), they experience the wave in a right-handed sense in the particle rest frame. This allows for a second type of gyroresonance called “anomalous gyroresonance”. It is through this mechanism that relativistic electrons can resonate with EMIC waves.

The condition that allows a population of electrons to gyroresonate with a parallel propagating EMIC wave with wave frequency ω and wave vector k, is given by Equation 1.5, where $v_{\parallel}$ is the electron velocity component parallel to the ambient magnetic field, and Ω_e is the electron cyclotron frequency. For the set of $v_{\parallel}$ and $v_{\perp}$ that satisfy Equation 1.5 where the relativistic factor, γ, is mathematically represented by Equation 1.6, the minimum energy, E_{min}, for an electron to be in resonance with the EMIC wave occurs when $v_{\perp} = 0$ and is given by Equation 1.7.

$$\omega - kv_{\parallel} = \frac{(-\Omega_e)}{\gamma} \tag{1.5}$$

$$\gamma = \left[1 - \frac{(v_{\parallel}^2 + v_{\perp}^2)}{c^2}\right]^{-1/2} \tag{1.6}$$

$$E_{min} = \left(1 + \frac{\Omega_e^2}{c^2 k^2}\right)^{1/2} - 1 \tag{1.7}$$

$$\omega_{pe}/\Omega_{ce} = \left(\frac{4\pi N_0 e^2}{m_e}\right) / \frac{eB_0}{m_e c} \tag{1.8}$$

As this condition occurs when the electron has a pitch angle near $\alpha = 0°$, as the energy of the particle increases above E_{min}, gyroresonance is satisfied for an increasing range of pitch angles. Theoretically, a particle needs only to be relativistic (have an energy near 0.5 MeV (Meredith et al., 2003)) to achieve anomalous resonance with an EMIC wave. In the magnetosphere, the minimum resonant energy might often be greater than 2.0 MeV. A number of studies have suggested that a minimum resonant energy of below 2.0 MeV is likely to occur only where the ratio of the electron plasma frequency to the electron gyrofrequency (Equation 1.8) is greater than 10 (Meredith et al., 2003; Summers & Thorne, 2003; Sandanger et al., 2007). This condition corresponds to regions of the magnetosphere where there is high plasma density and/or low magnetic field strength, such as the outer plasmasphere. The high plasma density can play the role of encouraging wave growth through reducing the phase velocity, and the low magnetic field resulting in lower magnetic energy per particle, lowers the energy needed to satisfy ion cyclotron resonance (Horne & Thorne, 1993, 1997; Cornwall et al., 1970) encouraging wave growth.

As a result of the gyroresonance (which violates the first adiabatic invariant) the particle exchanges energy with the wave, causing the particle to change pitch angle (i.e. the particle is scattered). This scattering is a diffusive process wherein the energy exchange along the diffusion curve is far less than the pitch angle diffusion Summers et al. (1998). The rate of pitch angle diffusion by EMIC waves is often considered to approach the strong diffusion limit, defined by Kennel and Petscheck (1966) as a loss rate such that the pitch angle distribution within the loss cone remains nearly isotropic, and that the precipitation rate is limited by the size of the loss cone. Some studies, such as Shprits et al. (2009), have demonstrated that strong diffusion should lead to increased losses where EMIC waves are preferentially excited.

When resonant electron populations are scattered and lost, a pitch angle and energy dependence may theoretically be observed in the particle distributions, revealing scattering signatures unique to EMIC wave interaction. In reality, the appearance of these scattering signatures can be quite complicated. In quasilinear pitch angle diffusion theory, the scattering signature is heavily dependent on the minimum resonant energy, which in the cold plasma approximation is sensitively controlled by the cold plasma density, the hot ion composition, and wave spectral properties. While often difficult to identify and examine, these signatures provide important insight into the scattering process. A novel approach to examine properties of EMIC wave scattering using wave properties derived from cold plasma theory is presented in Chapters 2 and 3.

Analysis of the pitch angle diffusion coefficients has suggested that EMIC waves are capable of scattering electrons in the strong diffusion regime, resulting in electron lifetimes of less than a quarter bounce period (less than about one second) (Kennel, 1969; Summers & Thorne, 2003). These scattered electrons result in rapid precipitation into the atmosphere that can be observed by low altitude polar orbiting spacecraft.

1.2.4 Precipitation

Particles may precipitate into the atmosphere and become lost from the radiation belts when their pitch angle is within the loss cone, $\alpha \leq \alpha_{LC}$. The equatorial loss cone is defined as the set of pitch angles within which the magnetic mirror point[4] lies below an altitude ($\sim$ 100 km) where collision with an atmospheric neutral particle is a statistical likelihood (Kennel, 1969) (Equation 1.9). The size of the loss cone where EMIC waves are more common is approximated to be $3.9° \leq \alpha_{LC} \leq 11.1°$.

$$\sin^2 \alpha_0 = B_{eq}/B_D(100km) \tag{1.9}$$

Relativistic electron precipitation (REP) events, which may be responsible for radiation belt flux depletions of several orders of magnitude across short timescales, commonly occur during the main phase of geomagnetic storms (Morley et al., 2010), linking them to the conditions favorable for intense EMIC wave activity. However, the extent to which EMIC waves are responsible for these events considering the known limitations of the interaction mechanism is unclear. Additionally, observations of low coincidence rates between the two types of events suggest that certain conditions must be met for EMIC waves to cause significant radiation belt depletion. As EMIC waves are also capable of scattering ions with energies on the order of tens of keV via standard gyroresonance, coincident precipitation of ions and electrons in the appropriate energy ranges can be used as an indicator of EMIC wave activity. This concurrent precipitation is used as evidence of EMIC wave activity in Chapter 4.

1.2.5 Limitations of the pitch angle scattering mechanism

Observational studies involving the direct relationship between EMIC waves and relativistic electrons have been difficult to conduct owing to the elusive nature of EMIC waves. Not only do these waves tend to be highly localized in L and MLT, but they are also limited in duration ($\leq\sim$ 30 minutes) as measured *in situ* (Clausen et al., 2011; Jun et al., 2019). Though direct evidence of this wave-particle interaction is lacking, many recent observational studies have reported coincident EMIC activity and relativistic electron precipitation events (Blum et al., 2015; X. Li et al., 2014). Several proxies for EMIC wave scattering have also

---

[4] the magnetic mirror point is the location along the magnetic field line where a particle reverses direction, or “bounces”, to travel back towards the equator. See Figure 1.2

been identified. For instance, Spasojević et al. (2004) and Spasojevic and Fuselier (2009), investigated the link between a detached subauroral proton arc and a plasmaspheric plume to suggest that the precipitating protons resulted from resonant interaction with EMIC waves amplified in the plume. Sandanger et al. (2007) showed that relativistic electron precipitation is almost always co-located with regions of proton anisotropy, where EMIC growth is preferred, thus concluding that concurrent precipitation of these protons and electrons are indications of EMIC wave resonant interactions. Additionally, numerous modeling efforts have demonstrated that the inclusion of EMIC waves is necessary to reproduce observed electron flux and pitch angle distributions (Shprits et al., 2016; Ma et al., 2015) in the outer belt.

While theoretical and observational evidence support EMIC wave-driven rapid relativistic electron scattering, limitations on the wave-particle interaction bring into question the effectiveness of the mechanism over broad enough energy and pitch angle ranges to have a significant impact on core electron populations (≤ 2.0 MeV) of the outer radiation belt. The interaction is restricted by the minimum resonant energy criterion, which has been suggested to be typically above 2.0 MeV in the outer radiation belt (Meredith et al., 2003; X. Cao et al., 2017), and limited to particles with a significant share of their total energy along the field-aligned velocity component (Albert, 2003) (small pitch angle). This limitation has been investigated using theory and modelling and has been supported observationally. Usanova et al. (2014) used computed pitch angle diffusion coefficients and relativistic electron precipitation data to demonstrate that pitch angle scattering by EMIC waves was confined to low pitch angles for energies above 2.0 MeV. Additionally, Shprits et al. (2016, 2017) demonstrated through modelling that while EMIC waves are involved in rapid relativistic electron loss, the energy range was restricted to multi-MeV electrons (ultrarelativistic). The emphasis on scattering of ultrarelativistic energies has been supported by works such as Cao et al. (2017) and Zhang et al. (2016).

It has been shown, however, that under specific conditions (i.e. regions of high cold plasma density and/or low magnetic field[5]) the minimum resonant energy can drop below 2.0 MeV (Meredith et al., 2003; Ukhorskiy et al., 2010). Some recent observations of EMIC-related electron precipitation involving energies in the keV range (Hendry et al., 2017, 2019) suggest that additional observational evidence is needed to definitively understand the electron populations that can be affected by EMIC waves. The likelihood of this drop to lower energies and the associated pitch angle ranges of electrons that can be scattered has yet to be thoroughly observationally investigated. Related, quantitative observational evidence of electron pitch angle scattering and resultant precipitation in relation to the driving EMIC wave activity is lacking. Using a multi-point observational approach through both case studies and statistical surveys, this dissertation addresses these deficits.

1.3 Dissertation Overview

This dissertation addresses three fundamental questions regarding the effectiveness of EMIC wave activity in driving electron pitch angle scattering and loss from Earth's outer radiation belt:

1) How is EMIC wave activity related to outer radiation belt relativistic electron pitch angle distributions and observed fluxes?

2) Do EMIC waves drive scattering signatures of core populations of outer radiation belt electrons, and what are the preferred conditions to influence this scattering?

3) To what extent are EMIC wave-driven scattering signatures associated with relativistic electron precipitation events and what are the intensities of these precipitation events?

Investigating these questions is achieved by developing and utilizing new methods to both quantitatively and qualitatively compare *in situ* electron distributions with the responsible wave activity. By expanding these methods to an ensemble of events and comparing scattering signatures with observed precipitation into the atmosphere, the extent to which this wave-particle interaction process can impact the variability of the radiation belts is investigated.

---

[5] $\omega_{pe}/\Omega_e > 10$

The format of this dissertation is as follows. Chapter 2 uses a case study to demonstrate that EMIC waves can have an immediate and verifiable impact on relativistic electron pitch angle distributions. Often, this impact takes the form of a “bite-out” scattering signature which can be qualitatively described by an apparent minimum resonant energy (as evident by a lack of scattering below a certain electron energy) and a deepening bite-out signature with increasing energy. Following this qualitative description, Chapter 3 develops a quantitative criterion for attributing electron pitch angle scattering signatures to EMIC wave activity and validates the methodology using example events. It is shown that scattering signatures co-located with the responsible EMIC wave activity can be identified quantitatively. Chapter 3 then expands on these methods and statistically examines the occurrence of co-located EMIC wave-driven scattering signatures, as well as the typical pitch angle and energy ranges associated with these signatures. The results of this survey demonstrate that EMIC waves can impact core electrons in a statistically significant percentage of events. Chapter 4 presents the results of searching for electron precipitation events associated with the EMIC wave events and scattering signatures uncovered in Chapter 3. The precipitation events are quantified and analyzed to determine the leading factors that influence relativistic electron precipitation. To close, Chapter 5 summarizes and concludes this work and discusses the significance of the new knowledge gained here to the field of radiation belt dynamics and space weather.

CHAPTER 2

EMIC Wave “Bite-Out” Scattering Signatures

2.1 Introduction

Electromagnetic ion cyclotron (EMIC) waves may theoretically be a dominant driver of relativistic electron loss from Earth’s radiation belts; however, additional observational evidence is needed to quantify their impact. Gyroresonant wave-particle interaction theory predicts that the condition allowing an EMIC wave to interact with and scatter an electron is dependent on the electron’s pitch angle and energy.

This condition should result in a distinct energy-dependent scattering signature in the normalized (to the flux at $\alpha = 90^\circ$) flux distribution of electrons as they are scattered into the loss cone. This signature is also referred to as a bite-out, named for the apparent shape of the distribution. Such signatures are identified along with the responsible EMIC waves captured *in situ* on 15–16 February 2017. From the wave properties and local plasma conditions, the expected shape of the electron scattering signature is estimated and compared with observation. This chapter describes the first direct observation of this.

The close conjunction between the Van Allen Probes and Time History of Events and Macroscale Interactions during Substorms (THEMIS) mission during this time is employed to explore the temporal and spatial evolution of the scattering signature, as well as the surrounding wave activity. It is found that the scattering signature formed during continued wave activity over a period of less than a day. These results are consistent with wave-particle interaction theory and support the hypothesis that EMIC waves are capable of driving rapid (on a timescale of minutes) relativistic electron loss from the radiation belts. Additionally, the findings presented in this chapter provide compelling evidence that EMIC waves can have an immediate and verifiable impact on relativistic electron pitch angle distributions, improving the opportunity for investigating the gyroresonant interaction and motivating the expansion of this investigation to a statistical scale.

2.2 Data and Methods

The observation presented in this chapter was identified by taking advantage of a unique conjunction between the Van Allen Probes and THEMIS missions during February 2017, when the five spacecraft have their apogee in the midnight sector. Both sets of spacecraft are in orbits that are nearly equatorial and highly elliptical, passing through the outer radiation belts with substantial spatial coverage to traverse the likely excitation region of EMIC waves. The configuration of the spacecraft during this interval provide extensive *in situ* measurements and avoid spatial and temporal ambiguities related to wave propagation from the wave source region that accompany remote, ground-based evidence of EMIC wave activity. Also utilized are observations from the Los Alamos National Laboratory satellites (LANL/GEO) for conjunctive observations of protons and electrons at geosynchronous orbits. Abrupt flux enhancements observed at those spacecraft can provide further evidence of (often localized) injections that supply the free-energy source for EMIC wave excitation. Figure 2.1 presents the orbital configuration of the spacecraft during this observation.

2.2.1 Van Allen Probes

The Van Allen Probes mission (formerly the Radiation Belt Storm Probes, RBSP) consisting of two spacecraft (from here on referred to as RBSP-A and RBSP-B) was launched in 2012 with a stated objective to “provide understanding, ideally to the point of predictability, of how populations of relativistic electrons and penetrating ions in space form or change in response to variable inputs of energy from the sun” (Mauk et al., 2012). Carrying instruments designed for the purpose of addressing this objective, the Van Allen Probes mission provides an ideal laboratory for exploring the interaction of EMIC waves with relativistic electrons. Pitch angle resolved electron flux data over a broad range of energies is provided by the En-

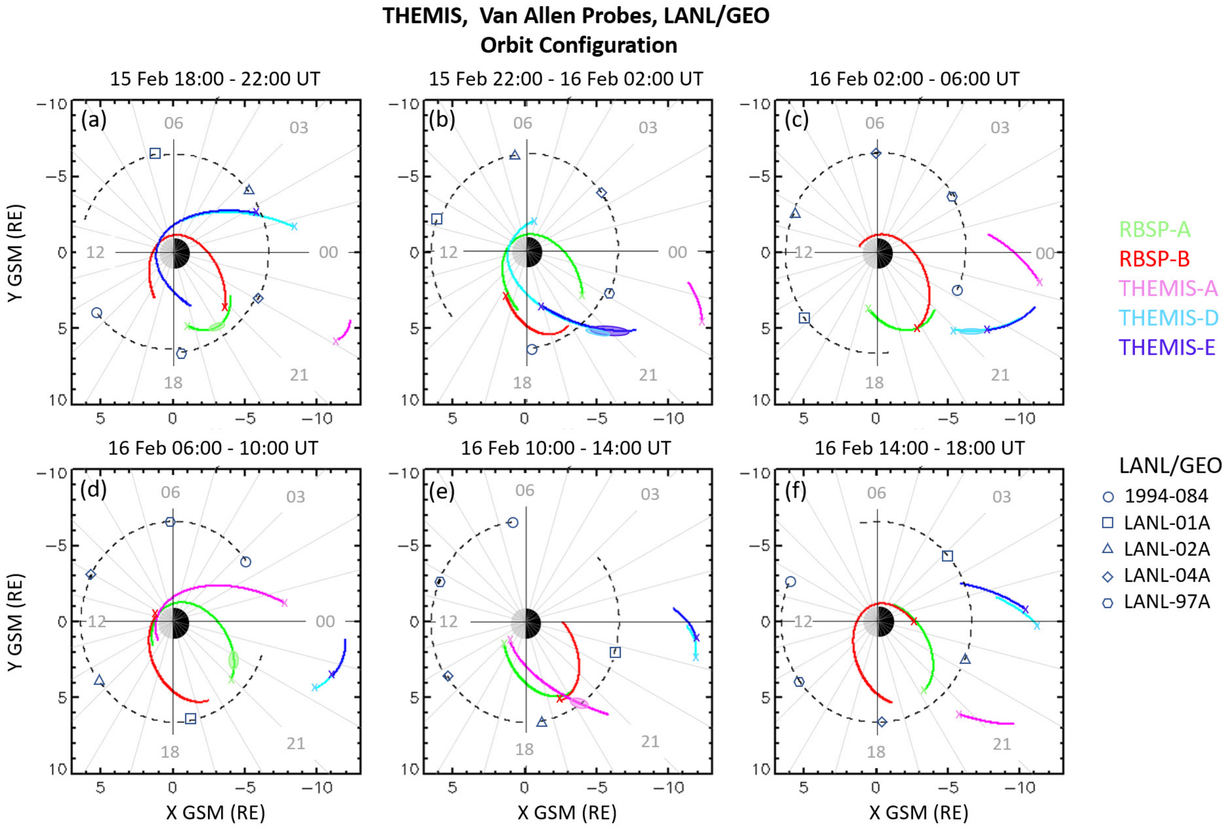

Figure 2.1: Spacecraft orbits projected onto the XY-GSM plane for a period of 24 hours around the scattering event. Spacecraft position at the beginning of the interval is marked by “x.” ovals along the trajectory highlight the times when He-band electromagnetic ion cyclotron (EMIC) activity was observed. He-band EMIC waves were persistent in the region of interest until around 16 February 2017 07:00 UT. Panels (a), (b), (d) and (e) represent spacecraft orbits during which wave activity is present but not simultaneously accompanied by a scattering signature. The simultaneous EMIC wave and scattering signature took place in panel (c). Panel (f) shows spacecraft orbits once wave activity had diminished.

ergetic Particle, Composition, and Thermal Plasma (ECT) instrument suite (Spence et al., 2013). For energies below 1.80 MeV, data comes from the Magnetic Electron Ion Spectrometer (MagEIS) (Blake et al., 2013), and for energies at and above 1.80 MeV, data from the Relativistic Electron-Proton Telescope (REPT) (Baker et al., 2012) is used. High-resolution magnetometer data from the Electric and Magnetic Field Instrument Suite and Integrated Science (EMFISIS) (Kletzing et al., 2013) is used to identify and deduce properties of EMIC wave activity. Finally, the Helium, Oxygen, Proton, and Electron (HOPE) instrument is used to determine local ion temperature anisotropies. The two RBSP spacecraft orbit Earth inclined approximately 10 degrees off the equator with an apogee that takes the spacecraft through the outer radiation belt. These data sets allow for the examination of EMIC waves in their excitation region, thus enabling direct observation of the impacts these waves have on outer radiation belt fluxes and pitch angle distributions.

2.2.2 Time History of Events and Macroscale Interactions during Substorms

The three inner THEMIS probes (Angelopoulos et al., 2008) (referred to as THEMIS-A, THEMIS-D, and THEMIS-E), are used to explore the extent of EMIC wave activity during the interval of interest. The conjunction between THEMIS and Van Allen Probes during this time provides additional observational evidence of continued EMIC activity in the dusk sector. This wave activity is surveyed using low-resolution (four samples per second) magnetic field measurements from the Fluxgate Magnetometer (FGM) onboard THEMIS (Auster, 2008).

2.2.3 Los Alamos National Laboratory - Geosynchronous Data

The Los Alamos National Laboratory has a historical dataset of radiation belt particles from spacecraft in geosynchronous orbit (LANL/GEO). This data includes measurements from the Synchronous Orbit Particle Analyzer (SOPA) (Belian et al., 1992) and Energy Spectrometer for Particles (ESP) (Meier et al., 1996) detectors and provides evidence of substorm injection which drives EMIC wave activity.

2.3 Observations

This observation is constrained to a 24-hour period during which geomagnetic conditions favor sustained EMIC activity. The relativistic electron pitch angle distributions observed during this time are found to contain the distinct scattering signatures expected as a result of this wave activity. Figure 2.2 (top panel) shows the solar wind and geomagnetic conditions during this time interval obtained from the OMNI database[1]. Blue dashed lines indicate the timing of various EMIC observations, and the shaded box represents the period during which pitch angle bite-out scattering signatures are present.

Table 2.1 presents the full time sequence of events. The observations begin on 15 February 2017 at 15:18:00 UT when the interplanetary magnetic field (IMF) turns southward, marking the beginning of an interval of preferable conditions for EMIC wave growth. Following the southward IMF turning, the auroral electrojet (AE) index begins to rise at 17:21:00 UT, suggesting increased substorm activity. Accompanying the rise in the AE index are injection signatures evident in LANL/GEO electron and proton omnidirectional flux spectrograms (see Figure 2.2 bottom panel). These injections are accompanied by an increase in the temperature anisotropy ($T_\perp/T_\parallel > 1$), which is captured with the Helium Oxygen Proton Electron (HOPE) mass spectrometer on board the (nearby) Van Allen Probes (Funsten et al., 2013) for protons below 50 keV. Intervals of peaked temperature anisotropy, such as those presented in Figure 2.2, likely provide the free-energy source for wave excitation. The bottom panels in Figure 2.2 suggest that temperature anisotropy increases are present in the region where EMIC waves were frequently observed. From these observations it is understood that increased substorm activity beginning late on 15 February 2017 acts to support the excitation of EMIC activity in the premidnight sector.

---

[1] OMNI space weather data, provided by the Space Physics Data Facility at NASA Goddard (https://omniweb.gsfc.nasa.gov/)

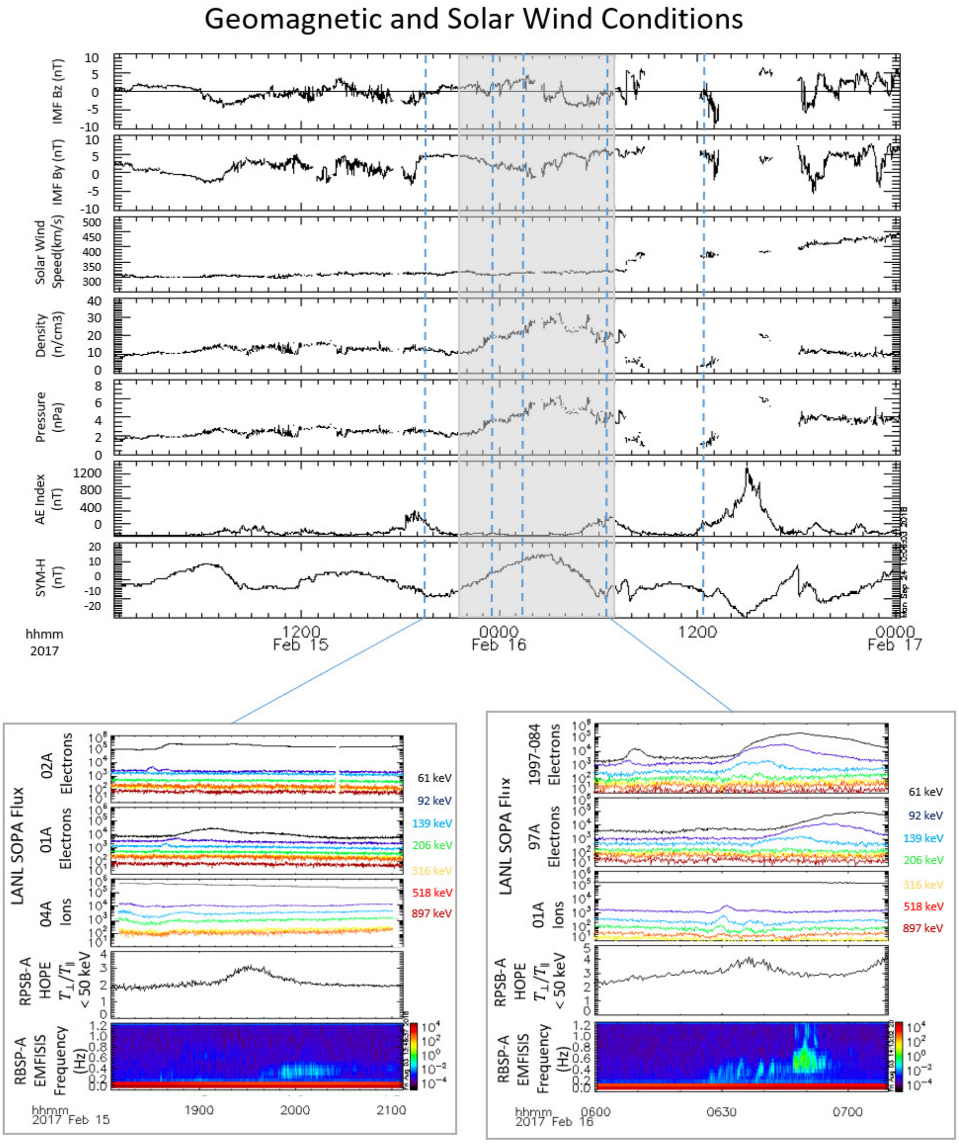

Figure 2.2: (Top) Solar wind and geomagnetic conditions. Blue dashed lines indicate the times of electromagnetic ion cyclotron wave observations, and the gray shaded box indicates the interval when the scattering signature was present in the electron pitch-angle distribution. (Bottom) Two examples of injection signatures followed by proton temperature anisotropy of < 50-keV protons from Helium Oxygen Proton Electron (HOPE), and a He-band electromagnetic ion cyclotron wave late 15 February 2017 and early 16 February 2017. EMFISIS = Electric and Magnetic Field Instrument Suite and Integrated Science; LANL = Los Alamos National Laboratory; SOPA = Synchronous Orbit Particle Analyzer.

Table 2.1: Sequence of Events

Date (DD-MM-YY)	Time (UT) (hh:mm:ss)	Observation
$15-02-17$	$15:18:00$	IMF Turns Southward
	$17:21:00$	AE Index Beings to Rise
	$18:31:30$	LANL-02A observes Electron Injection, MLT=2.98
	$18:33:10$	LANL-01A observes Electron Injection, MLT=7.28
	$18:42:00$	LANL-04A observes Proton Injection, MLT=22.84
	$18:51:30$	AE Index Peak at 400 nT
	$19:27:00$	LANL-97A observes proton injection, MLT=19.79
	$19:32:30$	RBSP-A HOPE observes peak in proton $T_{\perp}/T_{\parallel}$, MLT=19.60
	$19:38:00$	RBSP-A EMFISIS, He-Band EMIC Activity, MLT=19.68, L*=5.5
	$21:03:20$	LANL-04A observes electron injection, MLT=1.15
	$21:38:00$	LANL-97A observes proton injection, MLT=21.98
	$21:38:40$	RBSP-A HOPE observes peak in proton $T_{\perp}/T_{\parallel}$, MLT=21.00
	$21:39:58$	RBSP-A REPT, scattering signature between L*=5.0 $\pm$ 0.1
	$23:45:20$	THEMIS-E observes He-Band EMIC Wave, MLT=20.89
$16-02-17$	$01:23:00$	THEMIS-D observes He-band EMIC wave, MLT=20.86
	$01:29:20$	LANL-084 observes proton injection, MLT=21.9
	$02:40:00$	IMF Turns Southward
	$03:09:20$	RBSP-B REPT, scattering signature, MLT 21.00
	$03:13:00$	RBSP-B HOPE observes peak in proton $T_{\perp}/T_{\parallel}$
	$03:15:20$	LANL-01A observes small proton injection, MLT=15.9
	$06:07:28$	LANL-084 observes electron injection MLT=2.27
	$06:26:00$	AE Index Peaks at 330 nT
	$06:29:56$	LANL-01A observes proton injection, MLT 19.10
		RBSP-A observes peak in proton $T_{\perp}/T_{\parallel}$
		RBSP-A observes scattering signature, MLT=21.95
		RBSP-A EMFISIS captures strong He-band EMIC, MLT=21.95
	$11:56:30$	LANL-01A observes small electron injection, MLT=0.72
	$12:07:40$	RBSP-B observes new electron distribution
	$12:14:40$	THEMIS-A observes faint He-Band wave, MLT=20.19

2.3.1 Simultaneous Pitch Angle Bite-Out and EMIC Wave Activity

On 16 February 2017 at 06:29:56 UT during an inbound pass through the premidnight outer radiation belt (Figure 2.1c), RBSP-A captured a strong helium-band EMIC wave near 22:00 Magnetic Local Time (MLT) (Figure 2.3i). The wave persisted until 16 February 06:55:30 UT and had a peak wave power at approximately 0.6 Hz (0.75 times the equatorial helium gyrofrequency). Accompanying this wave was a distinct pitch angle bite-out scattering signature in the normalized electron distribution (Figures 2.3c-h). The pitch angle bite-out develops in an electron distribution already characterized by a flux minimum around $\alpha = 90°$. This distribution may have resulted from drift shell splitting and magnetopause shadowing leading to a loss of equatorially mirroring electrons, a process that is common in the outer belt (Fritz et al., 2003; Gannon et al., 2007; Turner et al., 2012). Alternatively, the flux minimum around $\alpha = 90°$ may also be due to electron interaction with magnetosonic waves, which are capable of rapid interaction with electrons near an L of 5.0 (J. Li et al., 2016). While field aligned electron losses accompanying a flux minimum around $\alpha = 90°$, forming a butterfly distribution similar to what appears in Figure 2.3, can be associated with the combined effects of magnetopause shadowing and drift shell splitting (J. Li et al., 2016; Selesnick & Blake, 2002), these processes can be effective for a broad range of energies. Therefore, the bite-out distribution that is created at $L^* = 5.0 \pm 0.2$ is distinctive as a result of EMIC wave interaction and not another process related to butterfly distributions. First, the signature has a noticeable energy dependence; below 1.80 MeV there is no scattering of field-aligned populations, indicating the existence of a minimum resonant energy. Second, the bite-out signature extends closer to $\alpha = 90°$ with increasing energy, indicative of a progressively larger pitch angle range in resonance with the wave. Such energy and pitch angle-dependent electron losses are consistent with EMIC wave-induced scattering (Usanova et al., 2014; Zhang et al., 2016).

Figure 2.3i shows that the EMIC wave spectrum is not uniform throughout the observation: the wave frequency slowly increases, and the wave power peaks sharply near 16 February 06:49:40 UT. In cold plasma theory, the minimum resonant energy for electrons to be scattered by EMIC waves is highly sensitive to the wave's spectral properties (Ukhorskiy et al., 2010); as such, the shape of the bite-out signature is expected to respond to the change in wave frequency. This is tested by calculating the maximum pitch angle scattered by the wave as it evolves. Eight points throughout the wave observation (denoted in Figure 2.3i by white dots) are used to calculate the minimum resonant energy at each point. In solving the cold plasma dispersion relation, the ion density ratio of [H+: 0.7, He+: 0.2, O+: 0.1] is used as an approximate to the typical duskside ratio (Lee & Angelopoulos, 2014b). The result reveals a minimum resonant energy that began near 3.30 MeV at the time when the wave was first observed, decreased to 1.8 MeV at 16 February 06:49:40, and increased slightly thereafter to 2.60 MeV until the wave disappeared. The average minimum resonant energy during the observation was found to be 2.36 MeV. With the minimum resonant energy determined for each point, the maximum pitch angle scattered by the wave at energies between 1.80 and 4.20 MeV is solved (the noise of 5.20-MeV channel was too high to allow quantitative comparison of a scattering bite-out, although flux variations are still suggestive of such an effect), as marked by the horizontal black curves in Figures 2.3c through 2.3g. The strong correlation between the calculated maximum pitch angle and the observed bite-out signature provides compelling evidence for the wave-induced losses.

2.3.2 Spatial and Temporal Evolution

Previous studies (Usanova et al., 2014) have demonstrated that pitch angle bite-outs may persist and evolve on multiday time scales. The next phase of this study investigates the evolution of this individual bite-out scattering signature at a specific energy (3.40 MeV) where the feature is prominent and considers how the distribution changes over time. This is possible by examining the pitch angle distributions observed by both Van Allen Probes as they pass through the electron drift paths between L* = 5.2 and L* = 4.8 (the region of interest), on consecutive orbits before and after the EMIC observation interval presented in Figure 2.3. This is based on the assumption that relativistic electrons drift along their paths on short enough time scales that a localized change in the pitch angle distribution is observable at any other location along the drift path within seconds of the local change.

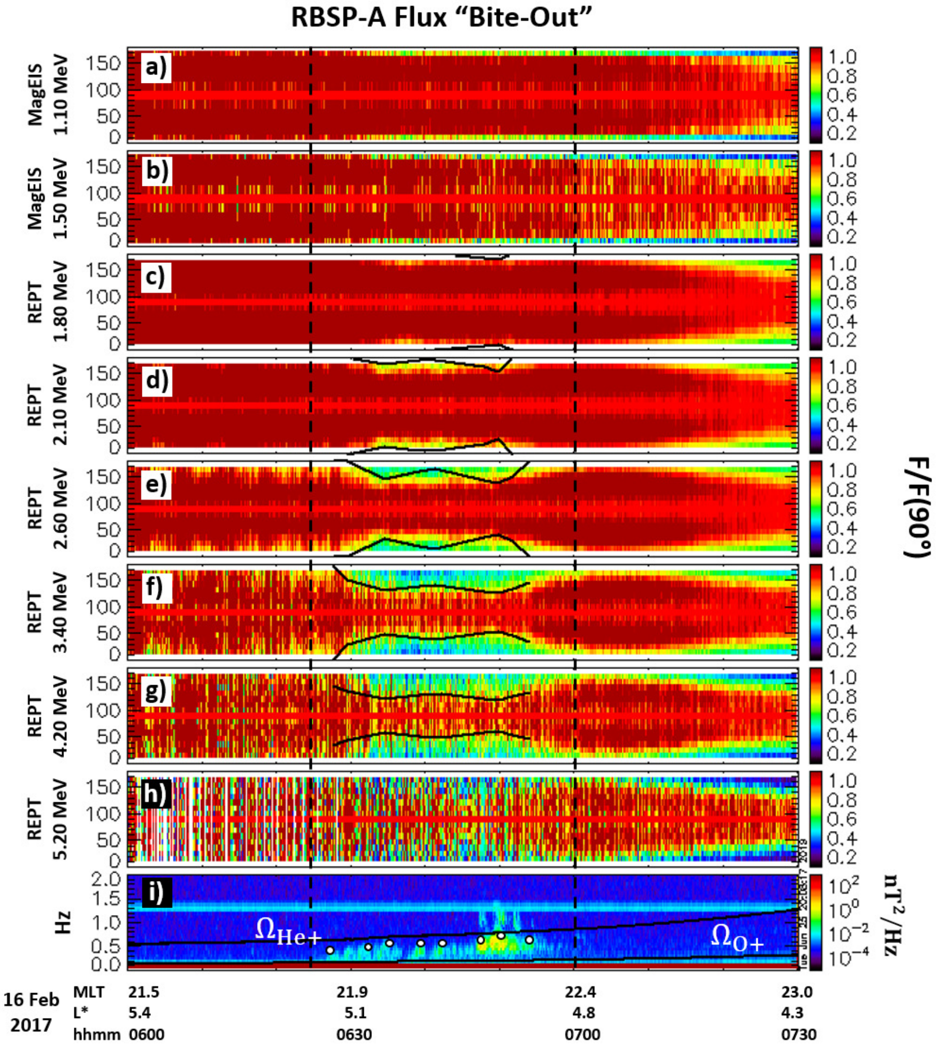

Figure 2.3: Energetic electron pitch angle distribution observed with Relativistic Electron Proton Telescope (REPT) and Magnetic Electron Ion Spectrometer (MagEIS) onboard RBSP-A, normalized to the flux at 90°. The region of interest (L* = 5.2 to L* = 4.8) is confined by the black dashed lines. He-band electromagnetic ion cyclotron wave (i) observed by RBSP-A. Particle scattering bite-out feature begins forming near 1.8 MeV (b) and deepens with increasing energy. Black curves in c–g show the estimated maximum pitch angle scattered based off observed wave and plasma parameters. MLT = magnetic latitude; REPT = Relativistic Electron Proton Telescope.

These observations are presented for five consecutive inbound passes (top to bottom, at spacecraft times indicated in the ordinate) through the region of interest (denoted by vertical dashed lines) in Figure 2.4. The panels on the left (Figures 2.4a through 2.4e) show the local pitch angle distribution for direct comparison to our primary observation. The panels on the right (Figures 2.4f through 2.4j) show the pitch angle fluxes mapped to the equator using an equatorial field produced with the OP77Q model (Olson & Pfitzer, 1982), to avoid the ambiguity of comparing electron data from two spacecraft at slightly different magnetic latitudes. In the mapped plots, the electron fluxes are normalized to the electron population with pitch angle closest to 90° where data were continuously available. Figures 2.4a and 2.4f show that there was no electron bite-out along the drift path of interest (between $L^* = 5.2$ and $L^* = 4.8$) 15 hours before the simultaneous EMIC observation presented in Figure 2.3. As RBSP-A passed through this region a few hours later, around 21:30 UT on 15 February, a shallow bite-out starts to form (Figures 2.4b and 2.4g). The bite-out broadens toward $\alpha = 90°$ pitch angles as RBSP-B follows RBSP-A to pass through this region at 02:45 UT on 16 February and becomes most prominent in Figure 2.4d, which corresponds to the primary observation detailed in Figure 2.3. Finally, in the last panels (Figures 2.4e and 2.4j), the distinct bite-out signature is no longer observed, replaced by a distribution that peaks closer to $\alpha = 90°$ pitch angle than the previous signatures, and extends far beyond the L* of interest where EMIC waves are seen. This apparent elimination of the bite-out signature is discussed in Section 2.3.4. From Figure 2.4 it is inferred that the scattering signature is a localized, in space (to the L* region of 5.0 ± 0.2), response to the wave activity. It begins forming at least 9 hours (but no more than 15 hours) before the simultaneous observation of EMIC waves and the strong bite-out feature. This is likely an indication that the spacecraft passed through the drift path of interest ($L^* = 4.8$ to 5.2) to observe the electron feature but were just outside of the magnetic latitude or MLT where the EMIC activity was taking place; it may not have been until pass 4 when RBSP-A entered the correct spatial region to observe the wave activity and electron scattering simultaneously. Additionally, the fact that this feature is present in both the local and equatorially mapped populations indicates that its appearance is not an artifact of measurements at different magnetic latitudes but a real

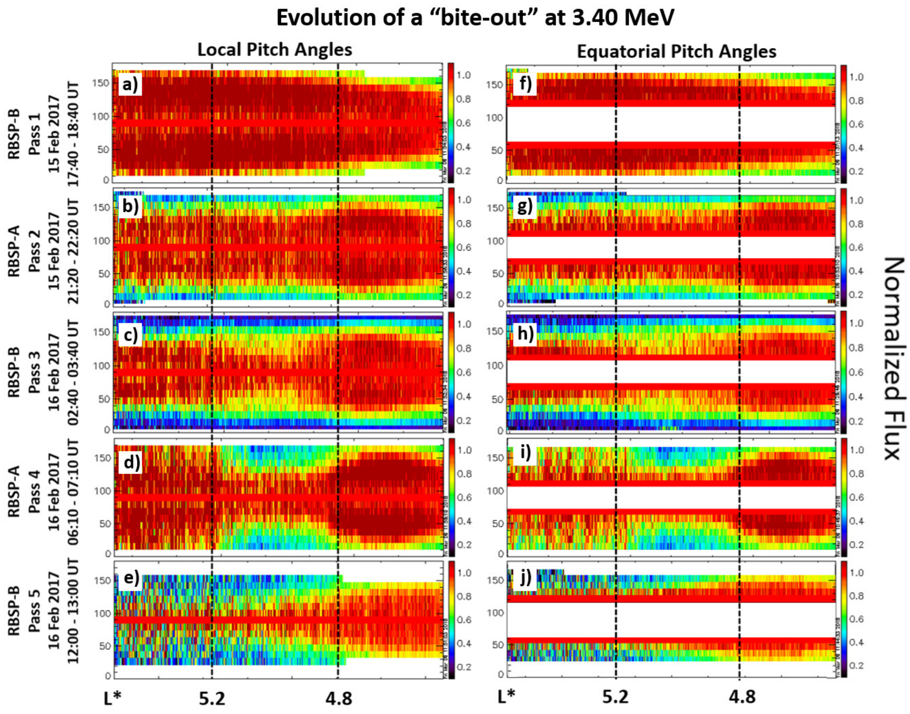

Figure 2.4: Comparison of the development of the local (left) pitch angle distribution through five consecutive passes through the region of L* = 4.8 to L* = 5.2 and the equatorial (right) pitch angle distribution.

loss of electrons at low pitch angles.

2.3.3 Extent of EMIC Wave Activity

As discussed in the previous section, the pitch angle scattering signature is present in the range of $L^* = 5.0 \pm 0.2$ for at least 9 hours, first appearing on 15 February at 21:39:58 UT and disappearing after 16 February 06:55:30 UT, even when the responsible EMIC wave activity is not captured simultaneously. This demands that EMIC wave activity must be present to sustain the scattering signature. The conjunction between THEMIS and Van Allen Probes during this time is used to survey the dusk region for evidence of EMIC wave activity during the evolution of the scattering signature. The orbit locations highlighted with ovals in Figure 2.1 indicate that indeed helium-band activity was observed by the THEMIS and Van Allen spacecraft during the interval surveyed.

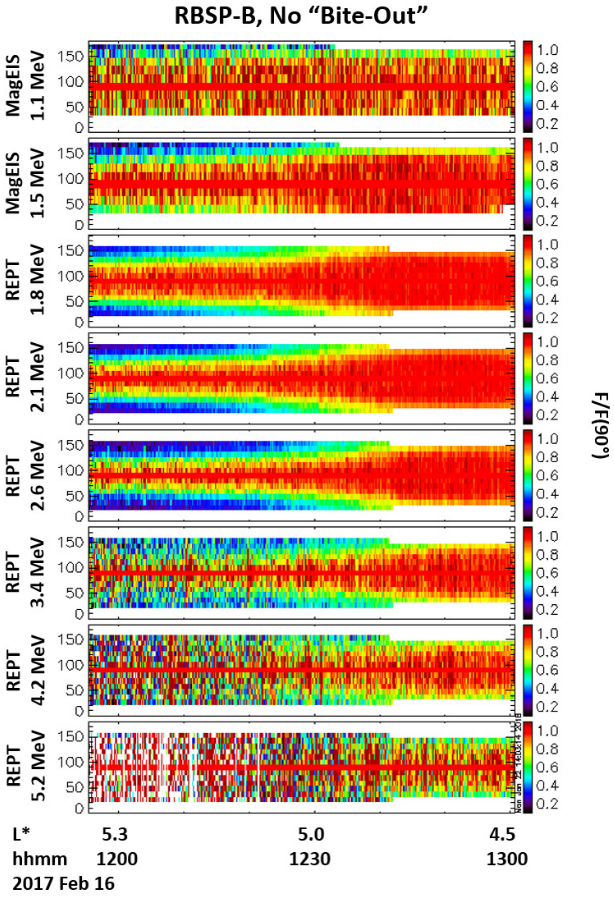

Figure 2.5: Normalized electron pitch angle distribution observed by Relativistic Electron Proton Telescope (REPT) and Magnetic Electron Ion Spectrometer (MagEIS) on RBSP-B just a few hours after the bite-out feature was observed by RBSP-A (Figure 2.3).

Activity was first observed on 15 February at 19:38:00 UT by RBSP-A, approximately 1 hour before the first bite-out scattering signature (see Table 2.1), following a substorm injection captured by multiple LANL/GEO spacecraft as well as a peak in the local temperature anisotropy for < 50keV protons (Figure 2.2, bottom left panel). Shortly after, at 15 February 23:45:20 UT, THEMIS-E captured similar EMIC activity as it passed through the same MLT region, closely followed by a nearly identical observation with THEMIS-D. The next He-band EMIC observation was the event described in Figure 2.3, which was accompanied by substorm injection and local proton temperature anisotropy (Figure 2.2, bottom right panel). The final EMIC observation of interest was captured by THEMIS-A and occurred at 16 February 12:14:40 UT. While this activity's location was consistent with previous observations (MLT 20.19), it is noted that its duration was significantly shorter in time and its spectral power noticeably decreased compared to previous EMIC observations. Though EMIC activity was not observed simultaneously with bite-out scattering signatures in passes 2 and 3, as it was for pass 4 (Figure 2.4), it is reasonable to infer that the responsible wave activity is present along the appropriate drift shell ($L^* = 5.2$–4.8), but is located just outside the view of the spacecraft. This inference stems from two observations. First, the initial Van Allen Probes EMIC observation was associated with a substorm injection and subsequent increase in the local proton temperature anisotropy, suggesting that the local plasma conditions supported wave growth as a response to the injection. Though passes 2 and 3 did not capture EMIC waves, they were both associated with substorm injection signatures and temperature anisotropy increases, which likely excited EMIC waves (see Table 2.1). Second, THEMIS-E and THEMIS-D captured He-band EMIC waves near the same MLT that bite-outs were observed within 2 hours of a bite-out signature, demonstrating that wave activity was in fact present, even if not captured by the Van Allen Probes.

This observation suggests that continued EMIC activity, driven by substorm injections and increases in local proton temperature anisotropy, acted to sustain the bite-out scattering signature for at least 9 hours. After 16 February 06:55:30 UT, the scattering signature is no longer observed, likely as a result of changing magnetospheric conditions.

2.3.4 Elimination of Bite-Out Signatures

The evolution of the electron scattering signature responds not only to EMIC activity but also to changing magnetospheric conditions. The pitch angle bite-out that developed between pass 2 (15 February 21:39:58 UT) and pass 4 (16 February 06:29:56 UT) in Figure 2.4 formed during relatively steady geomagnetic and solar wind conditions. As shown in Figure 2.2, there was no evidence of a geomagnetic storm, the solar wind speed remained steady around 300 km/s, and the magnitude of the southward component of the IMF (Bz) was small (< 5 nanoTesla (nT)). In addition, while substorm activity was present, the peak AE index was moderate (< 400 nT). Following the observation of the coincident wave and bite-out scattering signature presented in Figure 2.3 (pass 4, 16 February 06:29:56 UT), there is a sudden magnetospheric decompression, indicated by a drop in solar wind dynamic pressure (from 7 to 1 nanoPascal (nP)). The decompression was accompanied by a jump in solar wind speed on 16 February 07:42:20 to nearly 400 km/s, an increase in IMF Bz magnitude (>6 nT), and eventually a significant increase in the AE index to nearly 1,200 nT at 16 February 14:58:30 UT. These changes in solar wind and geomagnetic parameters indicate that the conditions that were previously preferable for EMIC growth and relativistic electron scattering have been disrupted. This is evidenced by the new electron distribution feature apparent in pass 5 in Figure 2.4 (16 February 12:07:40 UT), which no longer resembles the characteristic bite-out signature seen in previous orbits. Two observations suggest that this new electron distribution is a response to plasmaspheric reconfiguration due to changing solar wind and geomagnetic conditions, rather than a response to the observed EMIC activity. First, the new distribution is observed across a wide MLT (19.29 to 22.04) and across many L* (at least 4.5–5.6, as evident in Figure 2.4e), whereas the range of the scattering signatures in passes 2–4 was limited to between an MLT of 20.75 and 21.95, and an L* of 5.0 ± 0.2, corresponding to the narrow region of EMIC observations. Since the observed EMIC wave activity was seen to act on the electron populations in highly localized (in L*) regions, it is unlikely that the same He-band wave activity was responsible for a change this widespread. Additionally, widespread EMIC wave activity that might account for a bite-out of this spatial (in L*) scale was not observed on THEMIS or the Van Allen Probes. Second, the new distribution appears to have no energy dependence (as can be seen in Figure 2.5), in contrast to the previous scattering, and is also seen for ions (not shown here), not just electrons. In fact, the decrease in flux of field-aligned electrons compared to that of equatorially mirroring electrons extends to energies well below 1.50 MeV, which is inconsistent with the minimum resonant energy determined from the EMIC wave activity. From these observations it is inferred that the new electron distribution is likely the result of a global response to changing solar wind and geomagnetic conditions. It is also noted, however, that the new electron distribution observed during pass 5 corresponds to a significant decrease in the local plasma density as derived from Electric and Magnetic Field Instrument Suite and Integrated Science data. While previous passes took place when the local density was near $370cm^{-3}$, the density during pass 5 had dropped below $10cm^{-3}$, suggesting the observation took place outside of the plasmasphere. The exit to the plasma trough[2] is additional evidence of a global reconfiguration of the magnetosphere, which may move the active EMIC wave region and affected electron drift shells to another location or quench it altogether.

2.4 Discussion and Conclusion

The wave and electron observations presented in this chapter provide clear evidence for relativistic electron scattering by EMIC wave activity, capturing both the scattering signature and the responsible wave activity simultaneously. The presence of a minimum resonant energy and a widening range of pitch angles for electron loss with increasing energy are consistent with the wave-particle interaction theory. By expanding the investigation of the pitch angle distribution to additional time periods to observe the growth of this feature, it is concluded that it is a localized response to continuous EMIC activity in the dusk sector supported by moderate substorm activity. The scattering feature developed between L* = 5.2 and 4.8 and continued for at least 9 hours.

As demonstrated in Figure 2.1, wave activity persisted in the MLT region where the bite-out forms for the duration of the scattering period (gray-shaded region in Figure 2.2)

---

[2] The region between the plasmasphere and the plasma plume

and was captured by the Van Allen Probes and THEMIS spacecraft. The first observation of EMIC activity occurs about 1 hour before the first indication of a developing bite-out.

Approximately 5 hours after the bite-out observation at 16 February 06:29:56 UT, EMIC activity is no longer observed in the region, and after 16 February 06:55:30 UT the bite-out is also no longer observed. This further indicates that the bite-out scattering signature is a direct result of the observed EMIC activity. By pass 5 (16 February 12:07:40 UT) the scattering signature is eliminated, at least in that region of the magnetosphere, likely by the changing solar wind and geomagnetic conditions.

As discussed in Section 2.3.3, scattering signatures were present in electron data even when the EMIC wave was not directly observed. This can be explained by the rapid drift of relativistic electrons, allowing the signature to propagate from the scattering region along drift shells, so it is detectable by spacecraft crossing these drift shells at other local times. This suggests that EMIC wave activity may be remotely detected by identifying such scattering signatures.

Such studies may demand the investigation of scattering events in the context of a multiday orbit averaged flux observation to easily observe many different but consecutive events. Figure 2.6 applies this technique to the current case study to determine the feasibility of observations on a larger scale. The data are obtained from RBSP-A and are restricted to the regions between the drift shells of interest, $L^* = 5.0 \pm 0.2$. The colored arrows indicate the first appearance of the bite-out signature (black, pass 2), the simultaneous bite-out and EMIC observation (green, pass 4), and the new global distribution (red, pass 5), respectively. In this representation, a few issues with the multiday orbit averaged technique become apparent. First, it is understood from Figure 2.4 that the bite-out signature began during pass 2 (black arrow in Figure 2.6), but it is not immediately obvious that this is the case in Figure 2.6. Close inspection of the distribution at the black arrow suggests there may be some scattering of near field-aligned electrons obeying an energy dependence. The electron distributions at 1.10 and 1.50 MeV appear nearly identical, while a slight narrowing begins to take place at 1.80 MeV. These features, however, are easy to miss when in contrast with the very clear narrowing during the next orbit (green arrow). Here, scattering starts at

1.8 MeV and the distribution becomes narrower with increasing energy. Finally, the global distribution (red arrow) appears as a continuation of the bite-out distribution from the prior orbit and gives the impression that EMIC wave scattering continues well into the following orbit. In fact, as discussed in the previous section, the necessary energy dependence is not present in this interval, and narrowing is observed below 1.8 MeV, unlike the previous orbits. Therefore, with the multiday orbit averaged view alone, one might misinterpret the evolution of a scattering signature.

A comparison between the instantaneous scattering bite-out in Figure 2.3 and the multiday orbit averaged study in Figure 2.6 suggests that scattering events may happen on time scales that are too quick to be revealed by multiday observations, as the true scattering signature may only be present for one or two orbits. While bite-out signatures that appear in long term, time-averaged pitch angle distribution observations may indicate EMIC activity, responses to global magnetospheric changes may also be present that are difficult to disentangle from wave-particle interactions with this representation alone. Therefore, it is reasonable to suggest that observations on short time scales (hours or minutes) are more reliable if trying to correlate features in the electron distributions with expectation from the wave-particle interactions.

This study investigated the correlation between EMIC wave activity (captured by the THEMIS and Van Allen Probes) and local relativistic electron pitch angle distributions. The main points are summarized below:

a. This chapter presents the first direct observation of the formation and evolution of a pitch angle bite-out scattering signature along with the responsible EMIC wave activity, consistent with wave-particle interaction theory. Two clear indications of EMIC wave scattering were identified: the presence of a minimum resonant energy and the narrowing of the distribution toward $\alpha = 90^\circ$. Further evidence of the relationship between the wave and scattering signature resulted by using cold plasma theory to determine the minimum resonant energy and estimate the range of pitch angles scattered. The pitch angle range estimate and electron observations were in close agreement, providing compelling evidence for the wave-particle interaction.

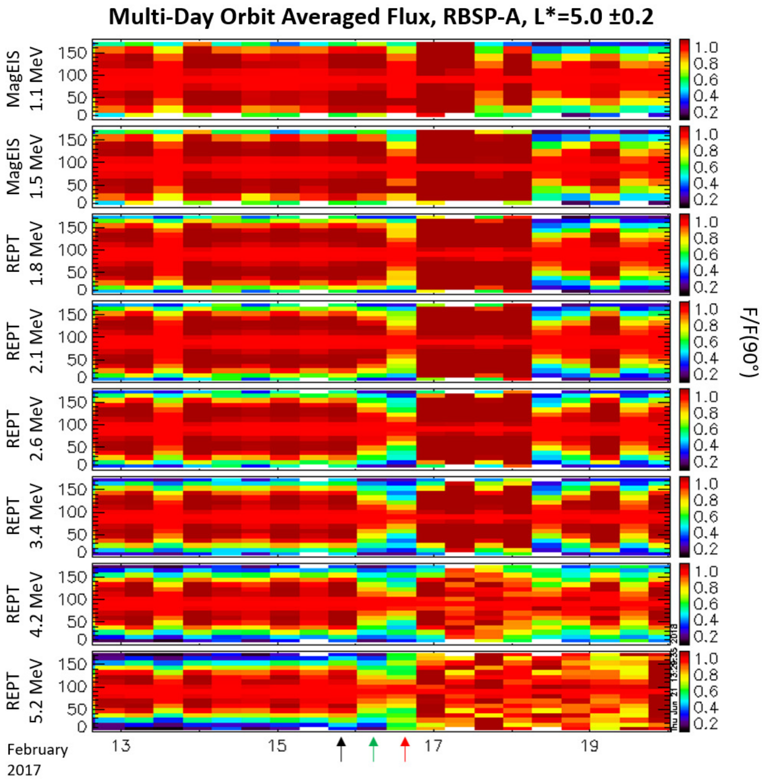

Figure 2.6: Normalized electron pitch-angle distribution observed by RBSP-A over a period of 8 days in February 2017. Only fluxes between $L^* = 5.0 \pm 0.2$ are considered, and the flux is orbit averaged. The black arrow indicates the time associated with the first indication of a bite forming (pass 2) presented in Figure 2.3. The green arrow indicates the simultaneous electromagnetic ion cyclotron and bite formation. The red arrow indicates the time associated with the observation presented in Figure 2.5 where there was no evidence of an electromagnetic ion cyclotron-related feature. REPT = Relativistic Electron Proton Telescope.

b. The bite-out signature in the electron distribution corresponds spatially (L* region of 5.0 ± 0.2) to the EMIC wave and existed on a short time scale (a few hours). The feature formed between L* = 4.8 and L* = 5.2 in the dusk sector only 1 hour after the first EMIC wave observation. The feature was then eliminated or obscured by changing solar wind and geomagnetic conditions.

c. Scattering signatures like the one presented may provide a reliable way to remotely detect EMIC wave activity using *in situ* particle data.

d. While a multiday orbit averaged bite-out may be indicative of sustained EMIC wave activity, it might also be a response to changing solar wind conditions resulting in a magnetospheric reconfiguration, or global changes to electron populations, and caution should be taken in using such an overview plot to locate the EMIC wave activity. Ambiguities related to this effect can be addressed by developing a quantitative criterion for EMIC wave-driven pitch angle scattering signatures, which is explored in the next chapter.

CHAPTER 3

Statistical Observations of EMIC Wave-Driven Scattering Signatures

3.1 Introduction

The extent to which the EMIC wave scattering mechanism can drive loss of core radiation belt electron populations (≤ 2 MeV) is presently unclear, partly due to a historical lack of direct observations of relativistic electron scattering and the responsible EMIC wave activity. This chapter first introduces a methodology for investigating pitch angle scattering signatures ("bite-outs") using derived quantities from the co-located EMIC wave and local plasma conditions. This method is then used to conduct a statistical study of EMIC wave activity captured by the Van Allen Probes between February and May 2017. For these events, the energies and pitch angle ranges involved in electron scattering are presented. On average, EMIC wave-driven scattering of core electron populations occurs in 28% of events. By comparing expected pitch angle ranges for scattering to electron flux measurements co-located with the wave activity, it is determined that scattering signatures are found in 46% of those. These results suggest that EMIC waves are capable of driving scattering of core populations of electrons, and that these scattering signatures are observable in pitch angle flux data.

This chapter is organized in the following way. Section 3.2 describes the selection process for EMIC wave events and the criteria for determining whether or not a concurrent electron scattering signature is present. Section 3.3 presents the statistical results, including the typical energy ranges and pitch angle ranges involved in the scattering. Finally, Section 3.4 discusses possible conditions that may contribute to the formation of bite-out scattering signatures, and comments on the implications of this study.

3.2 Data and Methodology

This chapter uses data from the Van Allen Probes mission (Mauk et al., 2012), comprising two near-equatorially orbiting spacecraft (hereafter referred to as RBSP-A and RBSP-B). Data sets are selected from a four-month time period (February through May 2017) when the two RBSP spacecraft sweep through the dusk side of the magnetosphere, the preferred region for EMIC wave excitation (Fraser et al., 1996; Meredith et al., 2003; Yuan et al., 2010). Figure 3.1 shows the orbital configuration of the two spacecraft during the observational period.

3.2.1 EMIC Wave Event Selection

EMIC waves are identified using high-resolution, field-aligned magnetometer data from the Electric and Magnetic Fields Instrument Suite and Integrated Science (EMFISIS) instrument (Kletzing et al., 2013) on board the two RBSP spacecraft. Following Bortnik et al. (2007), an automated algorithm searches for candidate events in the wave power spectra below the local proton gyrofrequency. Requirements for candidate events include: wave power sufficiently above background (by a factor of 0.75), event duration longer than five minutes, and left-handed polarization. The upper hybrid frequency limit of the wave (closest to the ion gyrofrequency, corresponding to the minimum electron energy for gyroresonant interaction) is used to characterize the event. For events in which the wave frequency crosses over the gyrofrequency, the wave frequency is selected as 0.05 Hz below the gyrofrequency to prevent E_{min} from dropping unrealistically low due to inaccuracies of using the cold plasma approximation[1]. The gyrofrequency band is tracked for each event.

---

[1] see Appendix A: Supplemental Information for a discussion about the limits on EMIC wave frequency in the cold plasma approximation

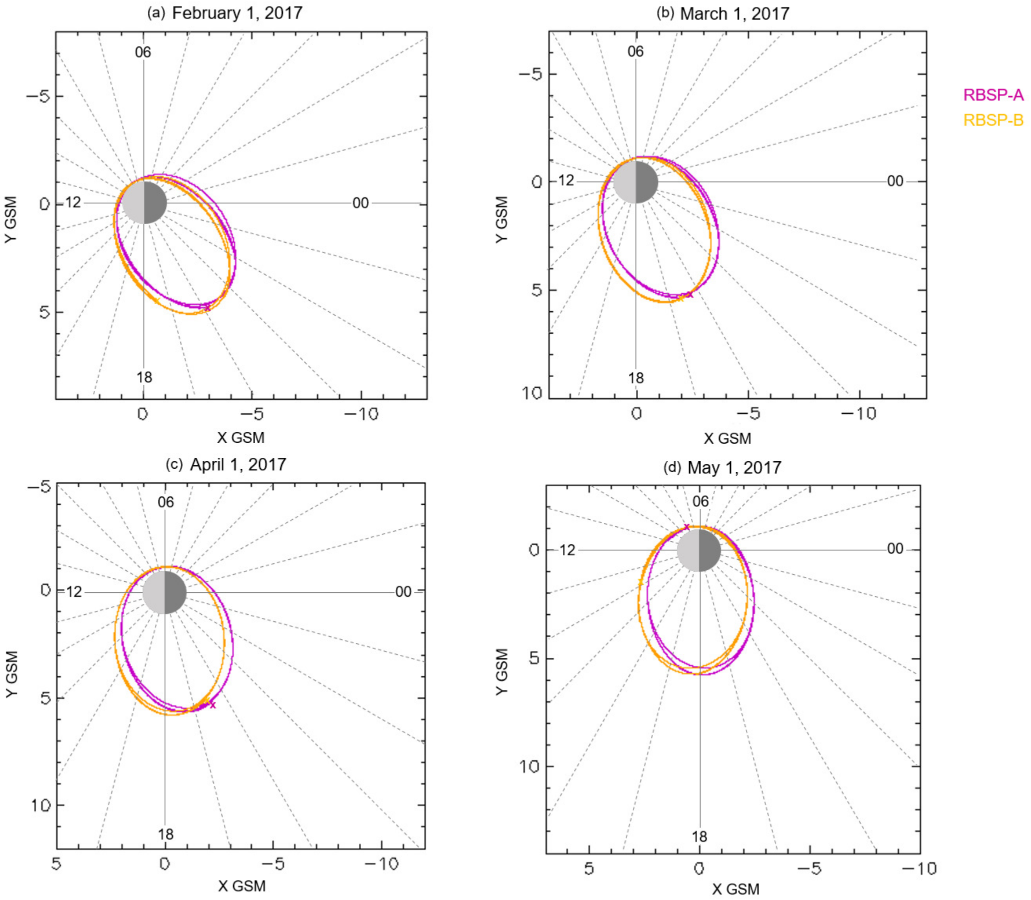

Figure 3.1: Orbital configuration of the Van Allen Probes (RBSP-A: magenta; RBSP-B: orange) during the four-month interval where events are collected. Each panel shows the first day of each month: (a) 1 February 2017, (b) 1 March 2017, (c) 1 April 2017, (d) 1 May 2017. The beginning position of each interval is marked by an "x".

3.2.2 Particle Data

Particle data used in this study comes from the Relativistic Electron Proton Telescope (REPT) instrument (Baker et al., 2012), as well as the Helium, Oxygen, Proton, Electron (HOPE) (Funsten et al., 2013) instrument. REPT is used to identify EMIC wave-driven scattering of electrons with relativistic energies (between 1.80 MeV and 5.20 MeV). This flux data is first smoothed using a 1-minute moving window average, then mirrored over $\alpha = 90°$ and finally normalized to the flux at $\alpha = 90°$. Measurements from HOPE are used to determine the local ion composition ratio for use in solving the wave dispersion relation. This data is also smoothed using a 1-minute moving window average.

3.2.3 Scattering Signature Methodology

Each EMIC wave event is compared to local electron pitch angle distributions to determine whether a scattering signature is present. This scattering signature is analyzed to determine how closely it matches with expectations from theory. The method for identifying and analyzing scattering signatures consists of five steps[2].

Step 1: Identify wave and plasma parameters

Step 1 involves identifying and extracting the full time series of relevant wave and plasma parameters, including the EMIC wave frequency ω, the background magnetic field (B_0), the ion composition ratio, and the background plasma density for the duration of the wave observation.

Step 2: Estimate the maximum resonant pitch angle

Step 2 uses the wave frequency along with local plasma parameters to solve the cold plasma dispersion relation (Equation 3.1) for the wave vector k in a multi-ion plasma.

$$\frac{c^2k^2}{\omega^2} = 1 - \frac{\omega_{pe}^2}{\omega(\omega + |\Omega_e|)} - \sum_{j=1}^{3} \frac{\omega_{pj}^2}{\omega(\omega - \Omega_j)} \tag{3.1}$$

The electron (ion) plasma frequency, $\omega_{pe(j)}$ (Equation 3.2), is solved using time series plasma density, N_0, from the Level 4 EMFISIS data, based on the upper hybrid frequency f_{uh} (Kurth et al., 2015). The electron (ion) gyrofrequency $|\Omega_{e(j)}|$ (Equation 3.3) is determined using the background magnetic field B_0 from EMFISIS measurements. When HOPE data for finding the local ion density ratio is not available, the typical ratio ([P: 0.7, He: 0.2, Ox: 0.1],(Lee & Angelopoulos, 2014b) is used.

$$\omega_{pe(j)} = \left(\frac{4\pi N_0 e^2}{m_{e(j)}}\right)^{1/2} \tag{3.2}$$

---

[2] See Section A.2 Supplemental Information for a demonstration of these steps

$$|\Omega_{e(j)}| = \frac{q_{e(j)} B_0}{m_{e(j)} c} \tag{3.3}$$

Using the reduced gyroresonant equation the approximate relationship between the minimum resonant energy (Equation 3.4) and k is determined.

$$E_{min} = \left(1 + \frac{\Omega_e^2}{c^2 k^2}\right)^{1/2} - 1 \tag{3.4}$$

It follows that the maximum resonant pitch angle, α_{max}, for a particle of energy $E > E_{min}$, is given by Equation 3.5.

$$\alpha_{max} = \cos^{-1}\left(\frac{|\Omega_e|}{ck} \frac{1}{E(E+2)}\right) \tag{3.5}$$

Therefore, by extracting a time series for k, the maximum resonant pitch angle is estimated for the duration of the wave event.

Step 3: Determine the flux loss at the pitch angle boundary

This step involves determining whether there is a loss of flux across the maximum resonant pitch angle boundary found in Step 2, which would indicate a loss of electrons consistent with expectations from the observed wave. This is referred to as the flux loss at the pitch angle boundary (Δf_b) and is calculated for the duration of the EMIC event in 5-minute intervals.

To solve the approximate (Δf_b) the flux below the boundary (α_{max-1}, the pitch angle bin below the bin containing α_{max}) is subtracted from the flux above the boundary (α_{max+1}, the pitch angle bin above the bin containing α_{max}) (Equation 3.6).

$$\Delta f_b = f(\alpha_{max+1}) - f(\alpha_{max-1}) \tag{3.6}$$

To distinguish a flux loss caused by the EMIC wave from a decrease due to other flux change effects (e.g. 90-degree peaked distributions created by drift shell splitting and radial diffusion), Δf_b is compared with a similar measurement, Δf_0, from a 5-minute flux interval measured 20 minutes before or after (depending on electron data availability) the EMIC wave. This interval is referred to as the undisturbed time interval. An interval is marked as a Pass (meaning the interval is a candidate scattering signature) if $\Delta f_b > \Delta f_0$, but a Fail if $\Delta f_b \leq \Delta f_0$. This results in a Δf Pass Rate calculated as the fraction of intervals at a given energy that are marked as Pass. This is repeated for each 5-minute interval and for each energy.

Step 4: Compare with undisturbed interval

In addition to a flux loss across the pitch angle boundary, a second indicator of scattering by EMIC waves comes from comparing the entire pitch angle distribution of the flux inside the EMIC wave interval with that in the undisturbed interval. It is also the case that the pitch angle range where scattering occurs is not the only pitch angle range impacted by scattering; some particles will be scattered to higher pitch angles, changing the normalized flux in that pitch angle range. For these reasons, a measurable change in the entire flux distribution from the undisturbed interval, not just a change at the pitch angle boundary, is expected.

Step 4 involves directly comparing the pitch angle distribution of the potential bite-out scattering signature to the undisturbed interval (also similarly normalized) using a Kolmogorov-Smirnov (K-S) test. This test quantifies the difference between two distributions and provides a K-S Statistic Significance Level (a value between 0 and 1) that indicates the similarity between the two distributions. For the purposes of this analysis, a statistic of ≤ 0.5 indicates the distributions are not similar, suggesting a local change has occurred. Similarly, a statistic of > 0.5 indicates that the distributions are similar, meaning no significant scattering has taken place. The K-S statistic is calculated for each energy at which scattering is expected and in the same 5-minute intervals used in Step 3. When the K-S statistic is ≤ 0.5 the interval is marked as Pass, noting it is a candidate scattering signature. As in Step 3, this results in a K-S Statistic Pass Rate calculated as the fraction of intervals at a given energy that are marked as a Pass. The results from either Step 4 or Step 3 independently are not necessarily indicative of a scattering signature. Combining these results from both in the next step is needed for increased confidence in the scattering identification.

Step 5: Scattering Signature Score (s)

After Step 4, each event is assigned a scattering signature score, s. The score is assigned using the results of Steps 3 and 4. The score, s, given by Equation 3.7, is representative of the fraction of 5-minute intervals throughout the wave duration in which both the change in flux across the pitch angle boundary and the K-S statistic Significance Level are marked as Pass, indicating a pitch angle distribution consistent with the expected scattering signature. In this equation, $R_{(K-S)i}$ is the Δf_b Pass Rate where the K-S Pass Rate is ≥ 0.5, n is the number of energies where the K-S Statistic Pass Rate is ≥ 0.5, and N is the number of energies evaluated. The score ranges between zero and one, where $s = 0$ indicates that there is no match with the expected signature, and $S = 1$ is a perfect match.

$$s = \frac{\sum_{i=0}^{i=n} R_{(K-S)i}}{N} \tag{3.7}$$

To demonstrate the range of scores for the events studied, three examples are presented. The first is the EMIC wave event studied in Chapter 2, comprising both helium-band and proton-band emissions. That event exhibits a clearly identifiable bite-out scattering signature (Figure 2.3 in Chapter 2). The original analysis performed on this event considered only eight points throughout the wave duration to solve for the α_{max} and used only the helium-band frequencies. The results closely matched what was visually observed in the electron flux pitch angle spectrograms. The event is re-analyzed here to examine the full wave duration and both the helium and proton bands. The analysis results in a scattering score of $s = 0.66$ for the helium-band wave and $s = 0.17$ for the proton band wave. The helium-band score is consistent with the co-located bite-out. These results also confirm that the bite-out was created predominantly by the helium-band wave.

Figure 3.2 shows an example of an EMIC wave event with a higher scattering score, $s = 0.90$. For this event (Event 91) the bite-out scattering signature is visually identifiable by a significant loss of flux at all energies corresponding to a strong helium band EMIC wave. The maximum pitch angle range estimation (black lines in 3.2a-3.2f) closely matches the visible bite-out in the flux distribution, except for the lower energies towards the midpoint of the event at 0530 UT. The maximum pitch angle estimation at this midpoint drops to lower pitch angles, which is inconsistent with what is seen in the pitch angle spectrograms. This

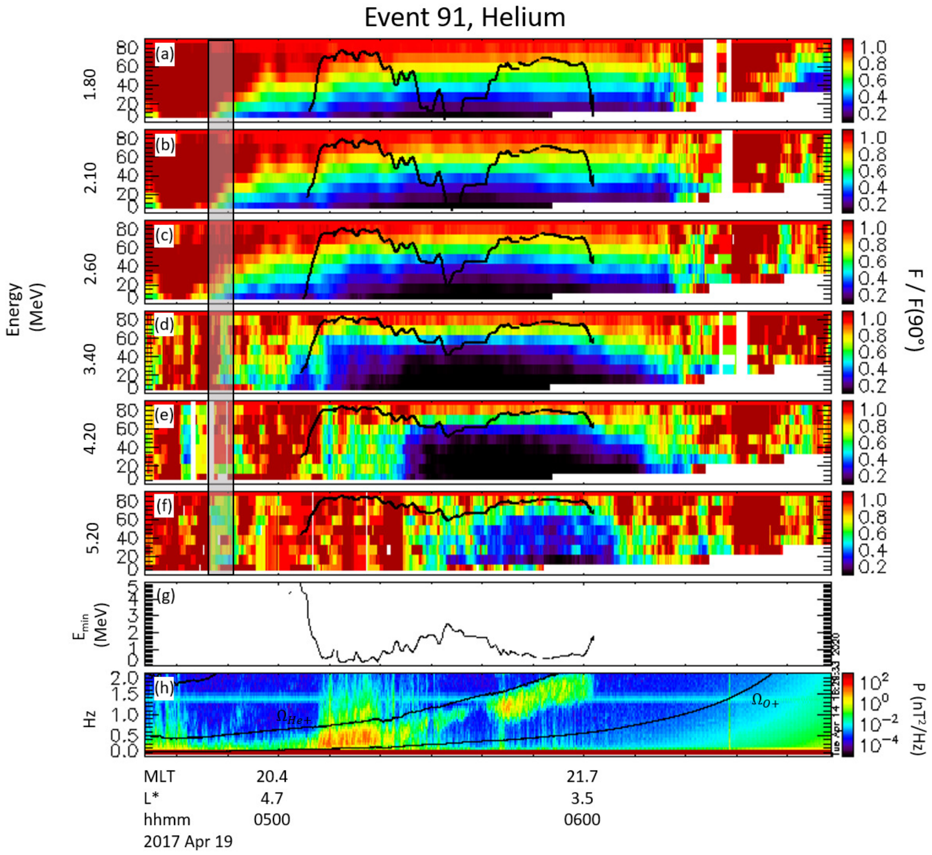

Figure 3.2: Example of an event with a high scattering score, where a helium band wave showed scattering of all energy electrons. The shaded region indicates the undisturbed flux used for scattering score calculation. Panels (a)-(f) show the normalized electron flux, panel (g) is the calculated minimum resonant energy, panel (h) is the wave power spectra.

drop corresponds to an increase in the minimum resonant energy, likely a result of a decrease in the wave power as well as an increase in the distance between the wave frequency and the helium gyrofrequency. One explanation of this inconsistency could be that the drop in wave power close to the noise level introduces increased error in the selection of the wave frequency. A second possibility is a temporary reduction in scattering as the wave power decreased that is not reflected in the electron pitch angle spectrogram, as the electron population may not have had time to recover. Despite this inconsistency, a majority of the electron flux shows a scattering signature consistent with expectations, hence a high scattering score. Table 3.1

Table 3.1: Event 91 “s” score results.

Energy (MeV)	Δf Pass Rate	K-S Statistic Pass Rate
1.80	0.875	1.0
2.10	0.875	1.0
2.60	0.875	1.0
3.40	0.875	1.0
4.20	0.875	1.0
5.20	0.875	1.0

s = 0.8958

shows the results of Steps 2 and 3 for this event, as well as the final score, s, to demonstrate how the final score is calculated. When Event 91 is compared with the event in Chapter 2, it can be seen that a stronger depletion (Event 91) results in a higher score.

In contrast to Event 91, Figure 3.3 (along with Table 3.2), provides an example of an event (Event 2) with a low scattering score where a certain level of scattering is taking place. The scattering signature estimate, however, does not well reproduce what is observed in the flux data. Two major differences between this wave event and the two previously discussed may contribute to this event's lower score: this helium-band wave is weaker than the one presented in Figure 3.2 and has a shorter duration (a few minutes). Scattering is not visually apparent in the distribution at the lower energies, but loss of flux at the higher energies is somewhat consistent with expectations. It is also noted that the electron pitch angle spectrograms for this event suffer from low counting statistics, potentially masking the scattering signature.

In the next section, this method is applied to a large set of observed EMIC waves and some explanations for the conditions that may contribute to the appearance of these bite-out scattering signatures are explored.

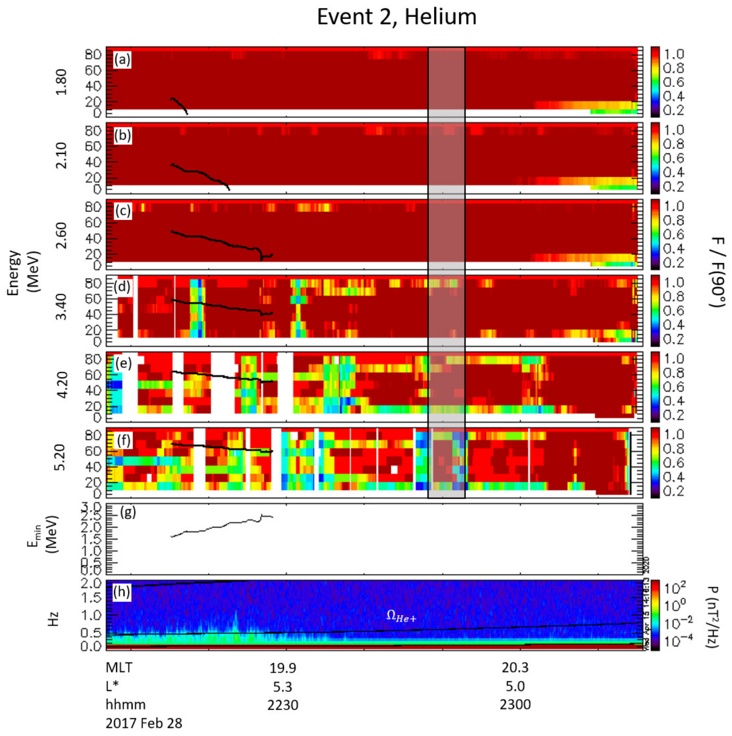

Figure 3.3: Example of an event with a low scattering score, where a helium band wave showed scattering only in the higher energies. The shaded region indicates the undisturbed flux used for scattering score calculation. Panels (a)-(f) show the normalized electron flux, panel (g) is the calculated minimum resonant energy, panel (h) is the wave power spectra.

3.3 Statistical Results

A total of 109 helium-band and 78 proton-band EMIC wave events are identified in the period between February through May 2017 that matched the criteria described in Section 3.2.1. The occurrence of these events is shown in Figure 3.4.

The steps outlined in Section 3.2.3 are followed to analyze each event for which sufficient wave and plasma data was available (e.g. events for which the background plasma density could be identified from the f_{uh}). This narrows the set to 129 events: 82 helium-band and 47 proton-band. These events took place during a time period of minimal geomagnetic activity. The majority of the events were associated with quiet time conditions, when the Dst was

Table 3.2: Event 2 “s” score results.

Energy (MeV)	Δf Pass Rate	K-S Statistic Pass Rate
1.80	0.0	0.0
2.10	1.0	0.0
2.60	1.0	0.5
3.40	0.5	1.0
4.20	0.5	0.5
5.20	0.0	0.0

s = 0.3333

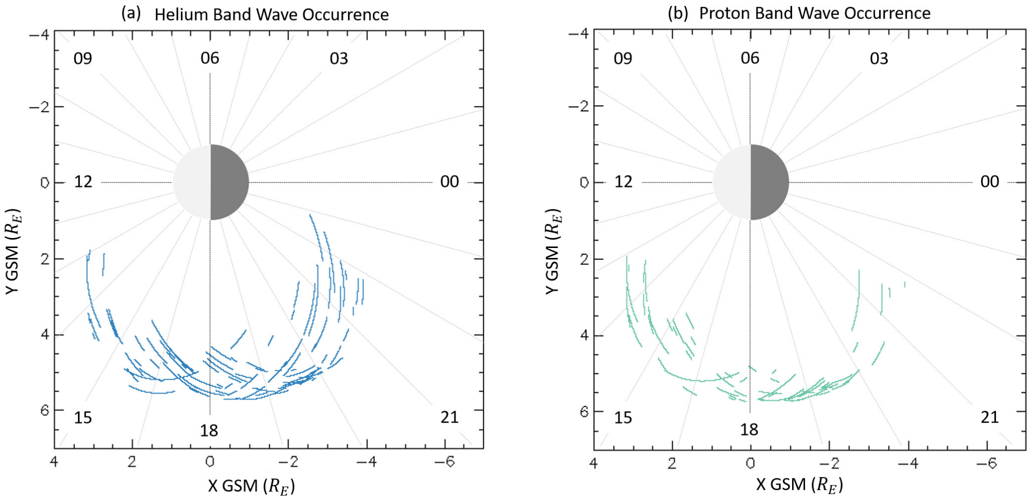

Figure 3.4: Distribution of detected helium-band (a) and proton-band (b) EMIC wave events above -50 nT[3].

The minimum resonant energy (E_{min}) is calculated for the full time series of the wave and the median E_{min} is extracted. The later is plotted as a function of the proton gyrofrequency in Figure 3.5.

The results show that 21 out of 82 (26%) helium-band events had a medium E_{min} that fell below 2.0 MeV; 15 out of 47 (32%) proton events had a median E_{min} that fell below 2.0

---

[3] see Appendix A.1 Supplemental Information for a description of the geomagnetic conditions during this interval.

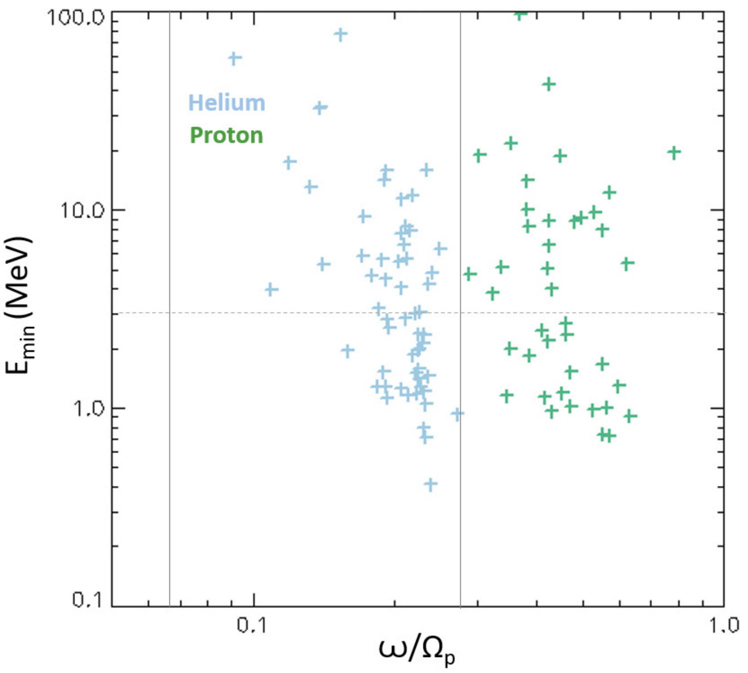

Figure 3.5: Median E_{min} for each EMIC event as a function of proton gyrofrequency. The first and second vertical gray lines represent the oxygen gyrofrequency and helium gyrofrequency, respectively.

MeV. In total, 28% of EMIC events have an E_{min} that allows scattering of electrons with energies below 2.0 MeV.

In many events the E_{min} does not stay constant throughout the duration of the wave observation, as it is extremely sensitive to a changing background density, background magnetic field, and proximity to the gyrofrequency (see black lines in Figure 3.2). Therefore, the median E_{min} does not always provide a complete description of the scattered population. For this, the full time series of the maximum scattered pitch angle, α_{max}, is needed.

Figure 3.6 shows the result of estimating α_{max} of all EMIC wave observations. The bottom panels (3.6b, 3.6d) show the percentage of total EMIC wave observations for which the predicted α_{max} falls in a particular pitch angle range, separately computed for each electron energy population considered. The top panels (3.6a, 3.6c) are the sum over all pitch angle bins in each energy to show the predicted occurrence of wave scattering at each energy.

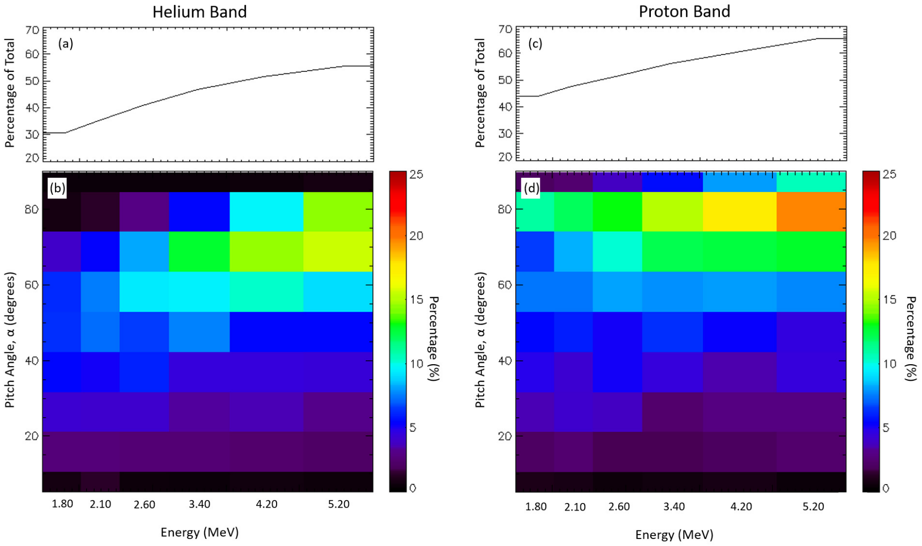

Figure 3.6: Maximum pitch angle occurrence rate as a function of electron energy for helium-band (a, b) and proton-band (c, d) events. Panels (a) and (c) show the percentage of total time that scattering can occur as a function of electron energy for all pitch angles. Panels (b) and (d) show the distribution of pitch angles.

The helium-band events (left) and proton-band events (right) have comparable results: for lower energy electron populations, the typical α_{max} is almost evenly distributed across all pitch angles. In contrast, higher energy electron populations have a typical α_{max} closer to ninety degrees. In general, the occurrence rate of α_{max} at mid-to-high pitch angles increases with increasing energy.

By focusing on the electron energies most consistent with the core population (1.80 MeV and 2.10 MeV), it is seen that, in general, scattering at each pitch angle is low (less than about 15% of the time) but roughly equally distributed over a wide range of pitch angles. This suggests that core electrons with higher pitch angles $\alpha \geq 60^\circ$ are just as likely to resonate with a wave as lower ($\alpha < 30^\circ$) and mid-range ($30^\circ \geq \alpha > 60^\circ$).

Although the probability of scattering at each fixed pitch angle range is low, integration over all pitch angles shows significantly higher percentages (3.6a, 3.6c) (i.e., between 30% and 40% for helium events and between 40% and 50% of the time for proton events). Although the occurrence rate of proton events is less than that of helium events, the likelihood of potential scattering at all energies and all pitch angles is higher for proton events than for helium events. These results suggest that by considering the minimum resonant energy based on the full duration of an EMIC wave event it becomes apparent that scattering of core electron populations is more likely than how often considering the only the median value suggests.

Next, Steps 3 and 4 are executed to determine whether the predicted scattering is consistent with what is observed in the REPT flux data. This analysis could only be performed for events where sufficient pitch angle data was available, which occurred in 96 events total (62 helium and 34 proton). The scattering score results are presented in Figure 3.7, separated into three categories.

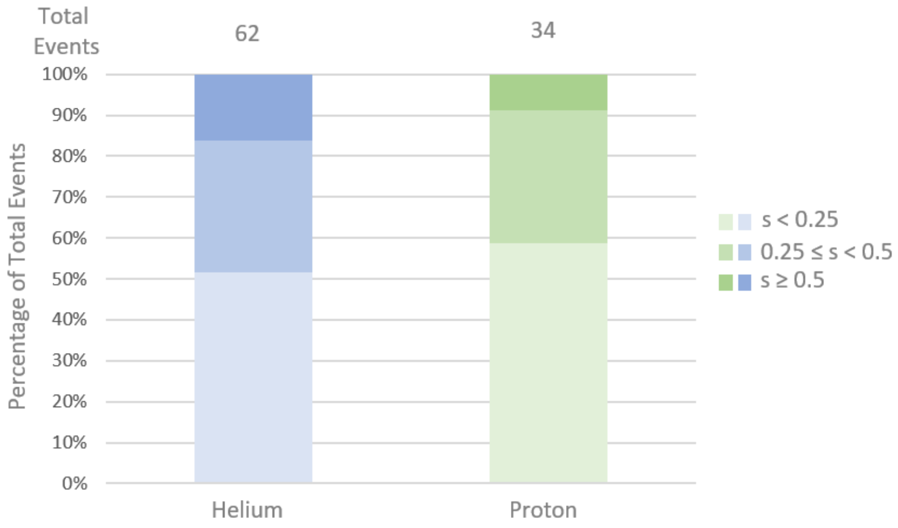

Figure 3.7: Scattering Score "s" for all events as a percentage of total, with the lighter shades representing lower scattering scores and the darker shades representing higher scattering scores.

Events that received a scattering signature score of less than s = 0.25 are categorized as having no observable bite-out scattering signature. Events with a score above $s \geq 0.25$ but less than s = 0.5 (similar the example shown in Figure 3.3) are considered as having some match with predicted scattering, and events with a score greater than or equal to 0.5 (like the example shown in Figure 3.2) are considered as having a good match. The helium and proton results have a similar distribution of events: between 50% and 60% of cases showed no match between the behaviour of the particle data and what was expected from the estimated pitch angle range, about 30% had some match, and 10-15% of events had a good match. Considering helium and proton events combined with $s \geq 0.25$, 46% of EMIC wave observations resulted in an identifiable scattering signature consistent with expectations from particle scattering from linear, cold plasma theory. In other words, under cold plasma assumptions, scattering of core electron populations is possible in anywhere between 30% of the time and 50% of the time, and the scattering observations imply that these assumptions hold true in nearly half of all EMIC wave events observed. These results indicate that EMIC waves may have a larger impact on core radiation belt variability than previously thought (Meredith et al., 2003; Usanova et al., 2014), since it appears the interaction is not limited to multi-MeV populations.

Next, the appearance of the EMIC wave-driven scattering signatures is compared with geomagnetic activity. As noted earlier, most events in this study took place during quiet conditions, with Kp rarely rising above 5. Figure 3.8 shows the distribution of scattering score results according to the geomagnetic Kp index. For both helium-band and proton-band events, as the Kp index increases, the fraction of events with scattering signatures increases. This suggests that even in the absence of strong geomagnetic storms, the formation and persistence of EMIC wave scattering signature increases with increasing geomagnetic activity.

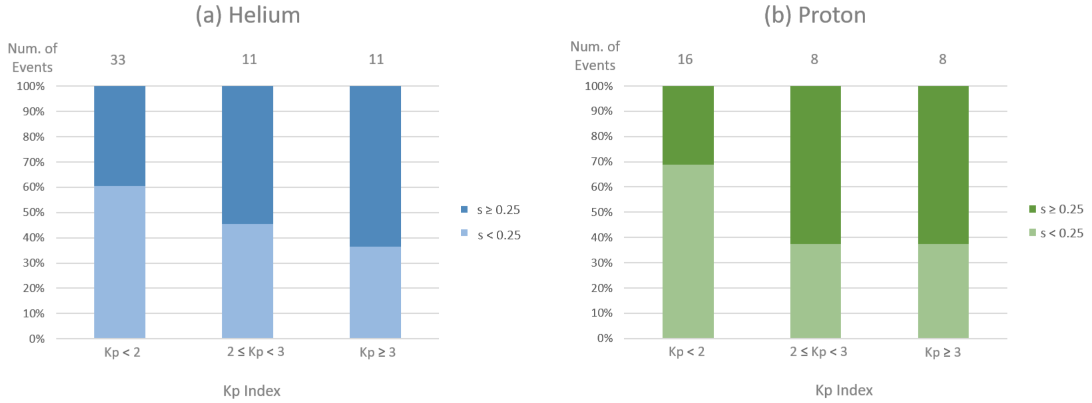

Figure 3.8: Scattering score as a function of Kp index for helium-band (a) and proton-band (b) events.

Finally, the relationship between scattering signatures and the average wave power of the corresponding EMIC event is considered. It has been suggested that more powerful waves might introduce non-linear scattering effects, such as phase trapping and phase bunching (Omura & Zhao, 2012, 2013). It is possible that these effects play a role in determining the formation of a scattering signature.

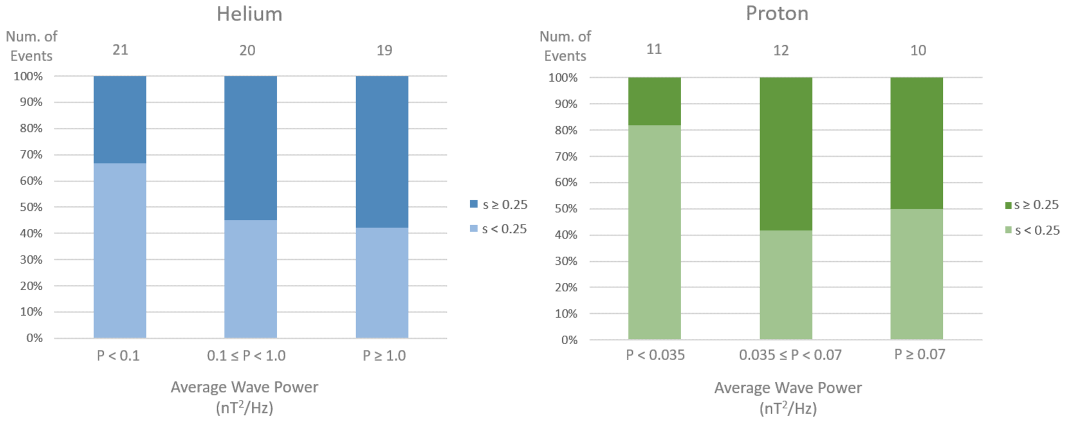

Figure 3.9: Scattering Score as a function of average wave power for helium-band (a) and proton-band (b) events.

Figure 3.9 explores that relationship for the events studied. For both helium and proton band events with greater average wave power (the two largest power categories), the fraction of scattering signatures was higher than for events with lower average wave power (the lowest power category).

Overall, these results suggest that scattering of core electrons by EMIC waves can occur in anywhere between 30% and 50% of observations when cold plasma assumptions are used. It is also found that scattering signature approximations from cold plasma theory are more consistent with observations under a higher Kp index and when the EMIC wave power is higher.

3.4 Discussion

This investigation statistically examines characteristics of EMIC wave-driven scattering of core radiation belt electrons. By considering the minimum resonant energy from EMIC wave properties, it is found that scattering of these populations (1.80 MeV and 2.10 MeV) is possible in 30% to 50% of EMIC wave events. It is also found that electron scattering at lower energies and higher pitch angles is more likely for proton-band events than for helium-band events. These results provide observational evidence of loss of core populations of relativistic electrons at low-to-moderate pitch angles.

The expected pitch angle scattering range was compared with what is observed in the flux data. It is found that approximately 46% of EMIC wave events are co-located with a bite-out scattering signature consistent with what is expected from our estimates ($s \geq 0.25$). A subset of these events, about 10% of all cases, match expectations with a scattering signature score greater than 0.50, indicative of strong pitch angle scattering. To my knowledge, this is the first time relativistic electron scattering signatures have been directly confirmed with the responsible driving EMIC waves on a statistical scale.

Electromagnetic ion cyclotron waves have been observed to be more prevalent and have larger amplitudes during geomagnetic storms (Blum et al., 2009; Halford et al., 2010; Ukhorskiy et al., 2010). The observations presented here, however, took place in the early months of 2017 when geomagnetic activity was generally low, and there were no significant geomagnetic storms. It is likely that EMIC wave-driven scattering of core electron populations would be increased during more active times. By comparing the scattering signature score with the Kp index, a positive relationship between the accuracy of the scattering estimates and increased geomagnetic activity was found. This result emphasizes the importance of including EMIC-wave effects in radiation belt modeling during periods of enhanced activity. It also suggests that EMIC waves captured during more active conditions are better candidates for future *in situ* observational study of this phenomenon.

These observations show a positive correlation between stronger EMIC waves and the appearance of scattering signatures. Stronger and larger amplitude EMIC waves have been previously linked to nonlinear scattering effects. Whether the introduction of nonlinear scattering increases or decreases scattering into the loss cone is currently under debate. These results support studies such as G. Wang et al. (2017) that have suggested that nonlinear effects can increase rapid electron loss.

It is also noted that cold plasma resonant interaction theory breaks down with the introduction of hot plasma effects. This breakdown is most often observable when the frequency of the EMIC wave comes near the gyrofrequency stop-band. In the EMIC wave selection criteria, this issue is mitigated in the E_{min} calculation by restricting the selection of the wave frequency to below the gyrofrequency. This does not, however, fully account for hot plasma effects. These results suggest that estimating scattering using cold plasma theory is accurate nearly 46% of the time. It would be worth expanding this analysis to include such effects in the future. Additionally, the results from solving the cold plasma dispersion relation may be improved with more accurate ion composition ratios.

Although the observations of scattering signatures presented in this study provide strong evidence for EMIC wave-driven scattering of core relativistic electron populations at low-to-midrange pitch angles, the lack of bite-out scattering signatures does not necessarily suggest that scattering and precipitation of relativistic electrons are not occurring. They may, indeed, be occurring but with energy and pitch angle ranges inconsistent with the estimations from cold plasma theory. To determine the extent to which precipitation is consistent with these scattering signatures requires an investigation of concurrent relativistic electron precipitation into the atmosphere. This is investigated in the next chapter.

CHAPTER 4

Relativistic Electron Precipitation Associated with Equatorial EMIC Wave-Driven Scattering Signatures

4.1 Introduction

In the previous chapters it was demonstrated that EMIC waves can create distinct scattering signatures in relativistic electron pitch angle distributions observed near the equator. While providing new and quantitative descriptions of the energy and pitch angle ranges affected by the responsible EMIC wave, these scattering signatures by themselves do not directly quantify the real radiation belt losses taking place. These losses can be determined by measurements of particles as they are precipitating into the atmosphere sampled using instrumentation located at the magnetic footpoints of the EMIC waves. This chapter uses datasets from such instruments on low-Earth polar orbiting spacecraft to extend the analysis of EMIC wave-driven scattering signatures to associations with relativistic electron precipitation (REP). This multi-point observation approach provides the first quantifiable tracing of the impacts of EMIC waves from their equatorial observation, through resulting *in situ* scattering signatures, and finally to electron precipitation into the atmosphere. These efforts not only confirm the connection between EMIC waves and REP events, but also provide new insights into the conditions that influence EMIC wave-driven radiation belt loss.

For many decades, precipitation of high-energy electrons into Earth's atmosphere has interested radiation belt scientists, and extensive investigation has begun to unravel the various mechanisms and conditions that drive it (see R. Millan and Thorne (2007), and Ripoll et al. (2020) and references therein). REP events characterized by localized bands or spikes, were first attributed to EMIC waves by Thorne and Kennel (1971), who suggested that pitch angle scattering resulting from wave-particle interactions can lead to particle loss to the atmosphere. Since then, numerous studies have provided strong supporting evidence for this hypothesis through direct observation of REP (R. Millan & Thorne, 2007; Miyoshi et al., 2008; C. Rodger et al., 2010; X. Li et al., 2014; Engebretson et al., 2015; Blum et al., 2015; Capannolo et al., 2018). For example, electron precipitation events, which may be responsible for radiation belt depletions of several orders of magnitude across short timescales, commonly occur during the main phase of geomagnetic storms (Morley et al., 2010), linking them to the conditions favorable for intense EMIC activity.

One indicator that has been used to identify EMIC wave-driven losses is the concurrent precipitation of tens of keV protons with MeV electrons. Carson et al. (2013) developed a detection algorithm using this technique to conduct a survey of twelve years' worth of precipitation data (from NOAA-POES satellites) and found 2,331 relativistic electron precipitation events characteristic of EMIC wave scattering. C. J. Rodger et al. (2015) used the same precipitation detection algorithm introduced in Carson et al. (2013) to identify a precipitation event, which when analyzed, was found to be consistent with an EMIC wave measured by the Van Allen Probes around the same time. More recently, Capannolo et al. (2018) analyzed three cases of EMIC wave-driven precipitation and found that characteristics of the precipitation events were consistent with quasilinear theory applied to the wave events in question. Chapter 2 demonstrated that EMIC waves can create distinct bite-out scattering signatures in equatorial electron pitch angle distributions, providing evidence for loss of MeV electrons. Various statistical studies between EMIC waves and precipitation events have provided even more compelling evidence that EMIC waves can drive relativistic electron precipitation. However, these studies also indicate that the coincidence rate between EMIC wave events and REP events is typically low. Qin et al. (2020), for example, found coincidence rates of REP to EMIC waves at 34%. In contrast, the results of the previous chapter showed that approximately 46% of EMIC wave events were accompanied by equatorial scattering signatures in relativistic electron pitch angle distributions, implying that coincidence rate might be higher.

Although efforts on this topic have led to significant confidence that EMIC waves can drive radiation belt losses, the reasons for typically low coincidence rates have not yet been fully resolved, even where there is strong evidence for EMIC wave-driven scattering. Zhang et al. (2016) for example, provided direct evidence of quasilinear relativistic electron scattering by an EMIC wave, yet no simultaneous precipitation of relativistic electrons and energetic ions was observed. Similarly, Usanova et al. (2014) confirmed narrowing of pitch angle distributions related to EMIC waves but was unsuccessful at observing corresponding relativistic electron precipitation. Attempts to explain this low coincidence rate have included insufficient instrumentation (precipitation rates below detector thresholds), limited scattered pitch angle and energy ranges (due to high E_{min}), low trapped fluxes before the scattering event, as well as inaccurate precipitation expectations resulting from a lack of understanding of the role of non-linear scattering.

Qin et al. (2020) attempted to explain these coincidence rates by investigating factors and conditions that lead to increased coincidence rates. Their results suggest that electron plasma density and proximity to the ion gyrofrequency might be leading factors. Others have suggested that the restriction of EMIC wave-electron gyroresonance to ultra-relativistic energies could limit the occurrence of EMIC wave-driven REP events. Even so, the connection to EMIC waves to the point of predictability remains unclear. In addition, which conditions and EMIC wave properties result in stronger precipitation events and, by extension, result in more significant radiation belt losses, is unknown.

The observations presented in this chapter address these questions by comparing relativistic electron precipitation events to quantitative, observable evidence of the scattering process taking place in the EMIC wave region. The EMIC wave events and resulting scattering signatures discussed in Chapter 3 are used to compare with evidence of relativistic electron precipitation into the atmosphere. This multi-point observation approach provides the first quantifiable tracing of the impacts of EMIC waves from their equatorial observation, through resulting *in situ* scattering signatures, and finally to electron precipitation into the atmosphere. These effort confirm the connection between EMIC waves and REP events and provide new insights into the conditions that influence EMIC wave-driven radiation belt loss. Whereas previous studies have successfully linked precipitation with EMIC waves, prior to the observations presented in this chapter, relativistic precipitation events have never been directly compared with quantitatively examined pitch angle scattering signatures.

4.2 Data

4.2.1 NOAA/POES and EUMETSAT/MetOp

The observations of relativistic electron precipitation presented in this chapter rely on data gathered by the National Oceanic and Atmospheric Administration (NOAA) Polar Orbiting Environmental Satellites (POES) and European Organization for the Exploitation of Meteorological Satellites (EUMETSAT) MetOp spacecraft. This investigation uses all five spacecraft available during the four-month interval of interest: MetOp1, MetOp2, NOAA15, NOAA18, and NOAA19. The NOAA/POES and EUMETSAT/MetOp spacecraft all carry the Space Environment Module (SEM-2) instrument package designed to measure energetic electrons and ions (Evans & Greer, 2000). Included in the SEM-2 suite is the Medium Energy Proton and Electron Detector (MEPED) capable of measuring electrons and protons between 30 keV and 200 MeV. On each spacecraft there are two sets of detectors, the 0° detector and the 90° detector, mounted perpendicular to each other. It is generally accepted that at high latitudes (greater than about $\sim 35°$) the 0° telescope captures the bounce loss cone and the 90° telescope observes the trapped radiation belt (Gamble et al., 2008; C. J. Rodger et al., 2010). As such, from here on out, the 0° telescope data is referred to as the precipitating data, and the 90° telescope data is referred to as the trapped data.

The MEPED instrument has multiple channels sensitive to different particle species and energies (see Table 4.1). The P6 channel, designed to measure protons with energy $E > 6900$ keV, suffers contamination of > 0.7 MeV electrons (Yando et al., 2011) making it useful for detecting relativistic electron spikes in the absence of relativistic proton spikes (M. I. Sandanger et al., 2009; R. M. Millan et al., 2010; Carson et al., 2013). Because the P5 channel does not have this same contamination it is used to confirm the absence of proton spikes which would otherwise make the P6 channel unusable for this electron identification.

Table 4.1: SEM-2 Channels

Channel	Proton Energies
P1	30 keV - 80 keV
P5	2500 keV - 6900 keV
P6	>6900 keV

EMIC wave-driven proton spikes are identified in P1 data.

4.3 Methods

4.3.1 Precipitation Event Selection

Signatures of REP events are searched for in NOAA/POES and EUMETSAT/MetOp SEM-2 data (full resolution data at a 2-second cadence) when the spacecraft have conjunctions with the Van Allen Probes at the times of EMIC wave observations. An EMIC wave conjunction interval is defined as the period of time when a POES or MetOp spacecraft is within an L-shell of L ±1.0, a magnetic local time of MLT ±1.5 hours, and a time of T ±1.0 hours of the EMIC wave event of interest.

Precipitation events are automatically detected within the conjunction intervals by the following process:

1: P6 (P1), both precipitating and trapped, data are loaded, degapped, and smoothed using a 6-second moving window average. The resulting electron (proton) time series are referred to as E_{6T} (P_{6T}) for the trapped population, and E_{6P} (P_{6P}) for the precipitating population.

2: P6 (P1), precipitating, data are smoothed using a 60-second moving window average. The resulting electron (proton) time series is referred to as E_{60} (P_{60}).

3: Within the E_{6T} time series, where the trapped electrons exceed $1.1 * 10^3$ counts/second is noted. This interval marks precipitation coming from the inner magnetosphere and is referred to as T_{IM}.

4: Within the overlap between T_{IM} and T_{conj} a trigger is applied to the electron (proton) data where E_{6P} (P_{6P}) exceeds E_{60} (P_{60}) by at least a factor of 2.

5: P6 and P1 data (both trapped and precipitating) are smoothed using a 30-second moving window average and the ratio of the precipitating-to-trapped flux is calculated. These are referred to as $RE15$ and $RP15$, respectively.

6: Within the overlap between T_{IM} and T_{conj} a trigger is applied for electrons (protons) when $RE15$ ($RP15$) is greater than 0.25.

An EMIC wave conjunction interval is counted as having a precipitation event if there is a trigger in the $RE15$ data. This is a signature of an increased precipitating-to-trapped electron ratio as a result of scattering towards the loss cone. The precipitation event criteria does not require simultaneous triggers in the electron count rate data or in the proton data. While a strong spike in the electron count data is a common signature used by other authors (Hyun et al., 2014; Clilverd et al., 2015; Yahnin et al., 2016) to identify scattering by EMIC waves, in cases where the trapped count rate is initially low, the precipitating counts will be low as well making it so that any increases in precipitating electrons is within the noise and difficult to detect. $RE15$ is immune to this problem and allows for identification of precipitation increases. The proton triggers are also somewhat unreliable, particularly in cases where any spike due to EMIC waves is obscured by signatures of curvature scattering. It should be noted that the precipitating-to-trapped ratio may be found to be greater than one. This is an unphysical effect resulting from radiation damage to the trapped detectors (Galand & Evans, 2000; M. I. Sandanger et al., 2015; Asikainen et al., 2012). While not used in the precipitation event criteria, the electron count, proton count, and proton ratio triggers are used in the event analysis.

4.3.2 Example Events

Shown below are three example REP events to demonstrate the use of the automatic detection process described in Section 4.3.1. These events correspond to the three scattering events presented as examples in Chapter 3. Figure 4.1 shows a positive REP event detection associated with the strong helium-band EMIC wave of Event 34 that resulted in a high scattering score. Panel (a) shows the electron count data (both precipitating and trapped), with the black dots indicating where the detection algorithm is triggered. Panel (b) shows the corresponding trigger for the electron ratio data when it exceeds 0.25. Panels (c) and (d) show similar triggers, indicating there was concurrent proton precipitation as well. Analysis of the wave and plasma properties performed in Chapter 3 suggested that this wave had a minimum resonant energy of ~ 2.0 MeV. A visually identifiable scattering signature was present in the REPT electron pitch angle distribution and its scattering score was calculated to be $s \geq 0.5$. This precipitation event was detected because of a precipitating-to-trapped electron ratio of $RE15 > 0.25$, and the evidence of precipitation of > 0.7 MeV electrons as well as the concurrent proton precipitation confirm real radiation belt losses.

Figure 4.2 presents a similar case. Event 91 is a strong helium-band wave that had a small E_{min} (~ 2.0 MeV). Like Event 34, this EMIC event is also associated with a scattering signature with $s \geq 0.5$. An associated REP event was positively identified by a trigger in $RE15$ which was accompanied by triggers in electron count rate, proton count rate, and $RP15$. This precipitation event is another example of real radiation belt losses resulting from an EMIC wave.

Figure 4.3, however, shows the case where Event 2, which was a weak EMIC wave and only resulted in a low scattering score, $s < 0.5$. This may suggest that EMIC waves that result in low scattering scores will not have associated REP events. The next section expands beyond these three examples to explore the connection between scattering signatures and REP events.

4.4 Observations

Between the months of February through May 2017 the Van Allen Probes collectively observed 147 EMIC wave events that met the criteria described in Chapter 3. Of these events, all but one had at least one conjunction interval with a polar orbiter. Since it is common that one EMIC wave event can have a conjunction with more than one polar orbiter, only the

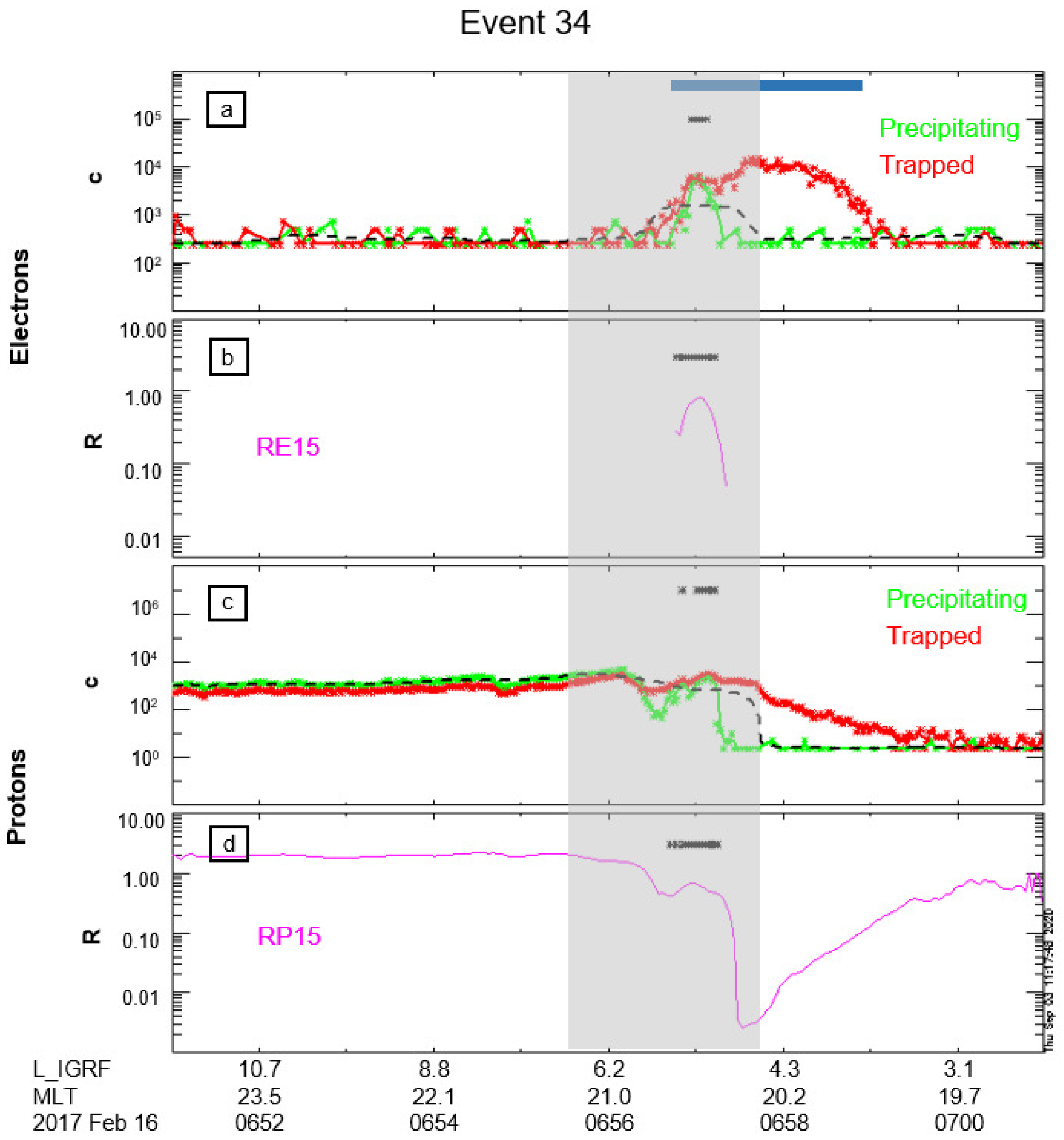

Event 34

Figure 4.1: Relativistic electron and keV proton precipitation associated with helium-band EMIC wave Event 34. Panels (a) and (c) are representative of the strength of the precipitation event for electrons and protons respectively, presented in counts per second. Black dashed line shows the 60 second smoothed precipitating data. The blue bar indicates the interval where the trapped electron flux is above 1.1E3, representative of the inner magnetosphere. Panels (b) and (d) show the precipitating-to-trapped ratios of electrons and protons, respectively. Black dots in each panel represent where the automatic detection triggered an event. The gray shaded region is the conjunction interval with the EMIC wave captured by RBSP.

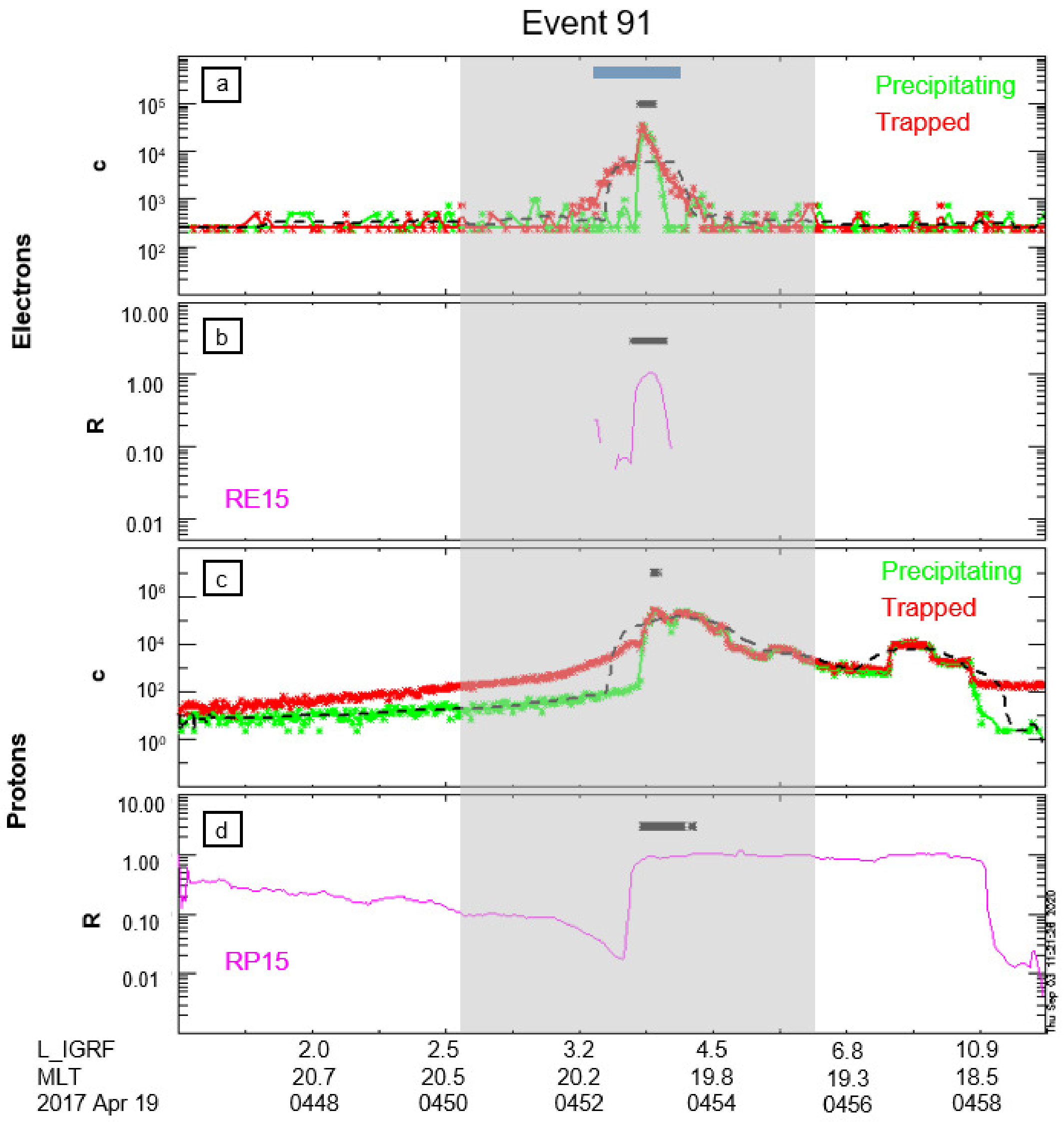

Figure 4.2: Relativistic electron and keV proton precipitation associated with helium-band EMIC wave event 91. Panels (a) and (c) are representative of the strength of the precipitation event for electrons and protons respectively, presented in counts per second. Black dashed line shows the 60 second smoothed precipitating data. The blue bar indicates the interval where the trapped electron flux is above 1.1E3, representative of the inner magnetosphere. Panels (b) and (d) show the precipitating-to-trapped ratios of electrons and protons, respectively. Black dots in each panel represent where the automatic detection triggered an event. The gray shaded region is the conjunction interval with the EMIC wave captured by RBSP.

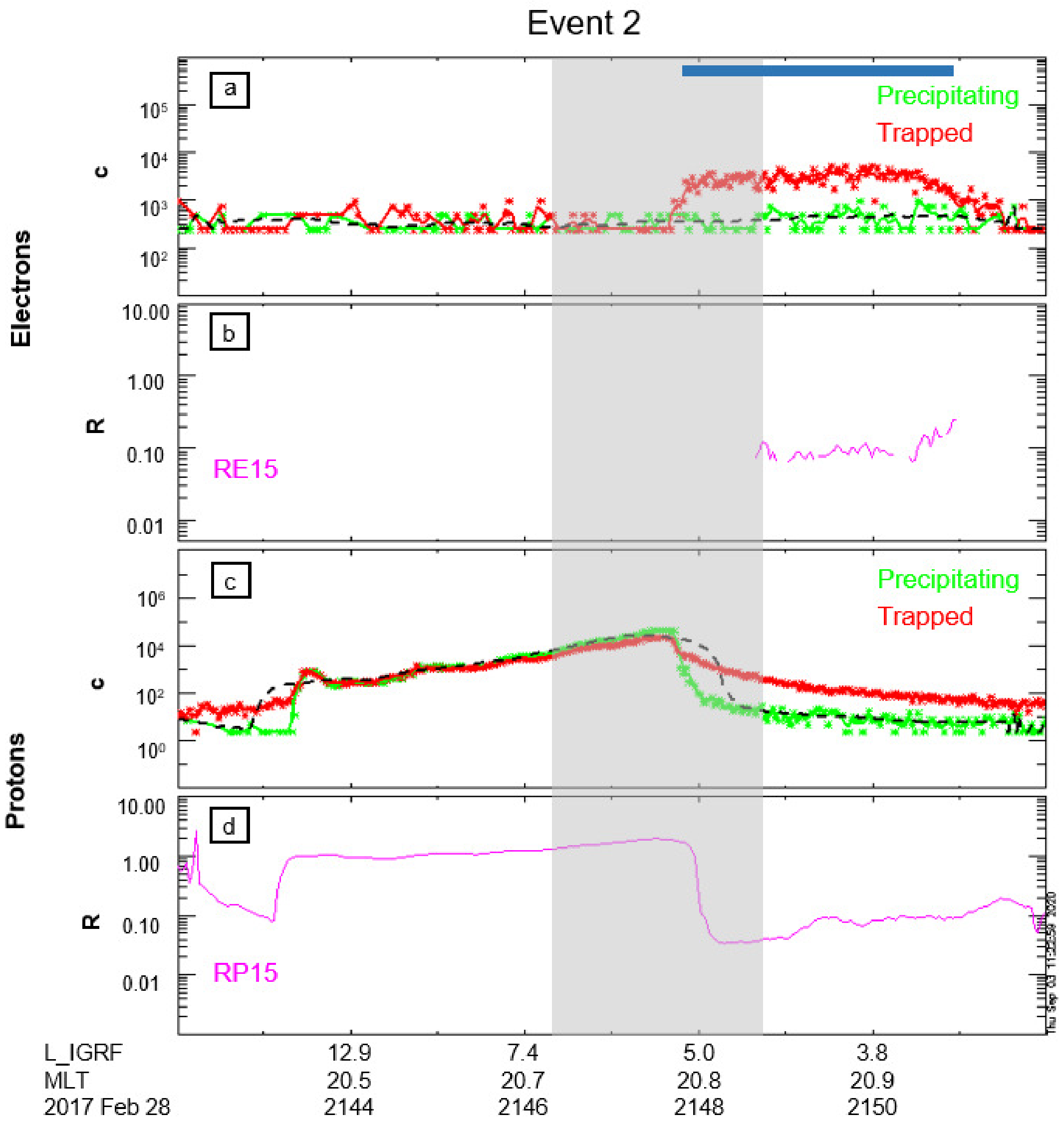

Figure 4.3: Relativistic electron and keV proton data associated with helium-band EMIC wave event 2, without an associated precipitation event. Panels (a) and (c) are representative of electrons and protons counts respectively. Black dashed line shows the 60 second smoothed precipitating data. The blue bar indicates the interval where the trapped electron flux is above 1.1E3, representative of the inner magnetosphere. Panels (b) and (d) show the precipitating-to-trapped ratios of electrons and protons, respectively. The gray shaded region is the conjunction interval with the EMIC wave captured by RBSP.

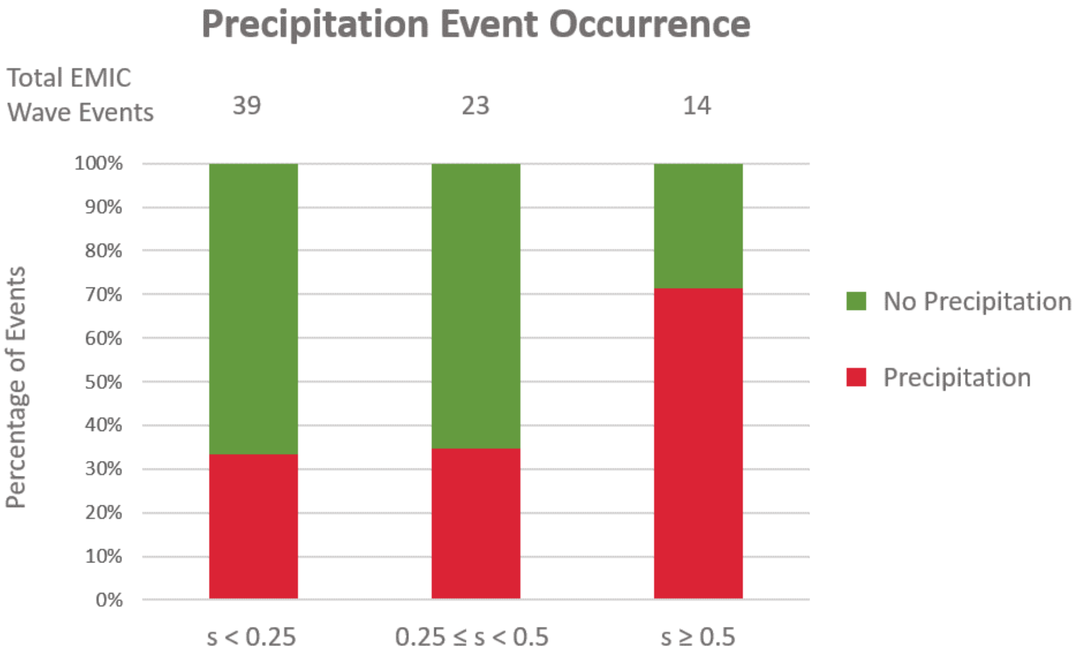

Figure 4.4: Precipitation event occurrence associated with EMIC wave-driven scattering signatures, categorized according to scattering score.

precipitation event with the highest precipitating electron count rate is used. Using the precipitation detection algorithm previously described it is found that 55 out of the 146 EMIC wave events, roughly 38%, are accompanied by a REP event on at least one spacecraft. Of the 55 events, 8 did not have a trigger in the electron count data (E_{6P}), 18 lacked a trigger in the proton count rate data (P_{6P}), and 3 had no trigger in the $RP15$ data.

Figure 4.4 compares the scattering score of EMIC wave events to the occurrence of precipitation. For the 39 events with low scattering scores ($s < 0.25$) less than 35% resulted in a REP event. Similarly, for EMIC events with mid-range scattering scores ($0.25 \leq s < 0.5$), almost 35% resulted in a REP event. Only in the category of high scattering scores, $s \geq 0.5$, is the fraction of precipitation events the majority at over 70%.

Figure 4.5 shows the relationship between the precipitation events and the scattering score, s, for the EMIC wave events. Note that if a particular EMIC wave event had emissions in both the helium band and proton band, and as such, a scattering score associated with each, the higher scattering score is used for this comparison. It is immediately clear that

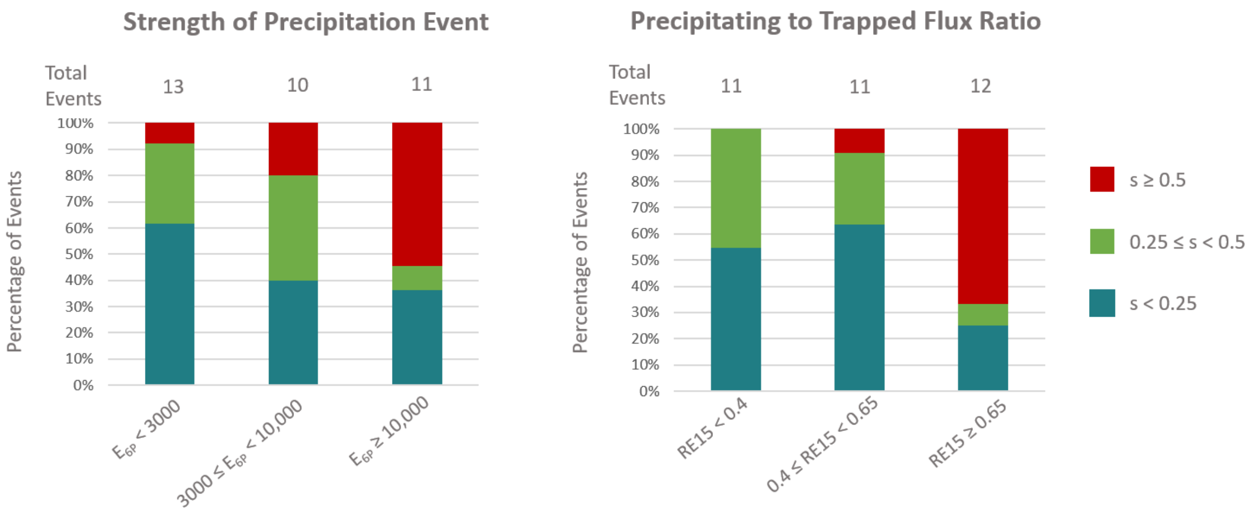

Figure 4.5: (Left) Strength of precipitation event E_{6P}, in counts per second, for EMIC wave events that resulted in relativistic electron precipitation, in association with scattering score, s. (Right) Precipitating-to-trapped ratio, RE15, for EMIC wave events that resulted in relativistic electron precipitation, in association with scattering score, s.

precipitation events with a higher electron count rate, E_{6P} and events with a higher electron precipitating-to-trapped flux ratio, $RE15$, were more likely to result from EMIC events with $s \geq 0.5$.

The median strength of all REP events is 4,390 counts/s, while the median strength of REP events associated with $s \geq 0.5$ EMIC events is 12,926 counts/s. Similarly, the median electron precipitating-to-trapped ratio, $RE15$, is 0.56 for all events and 0.95 for EMIC events with $s \geq 0.5$. For REP events that included triggers in the proton data, the median strength of proton precipitation is 22,052 counts/s for all events and 31,291 for EMIC events with $s \geq 0.5$. Unlike the electron ratio results, the proton ratio results, $RP15$, were nearly identical for the two categories: the median ratio, $RP15$ is 1.34 for all events and 1.35 for high s events.

Next, Figure 4.6 shows the relationship between the EMIC wave frequency proximity to the ion gyrofrequency and the scattering score for events where REP was positively identified. In this comparison a clear trend is seen. As the wave frequency approaches the ion

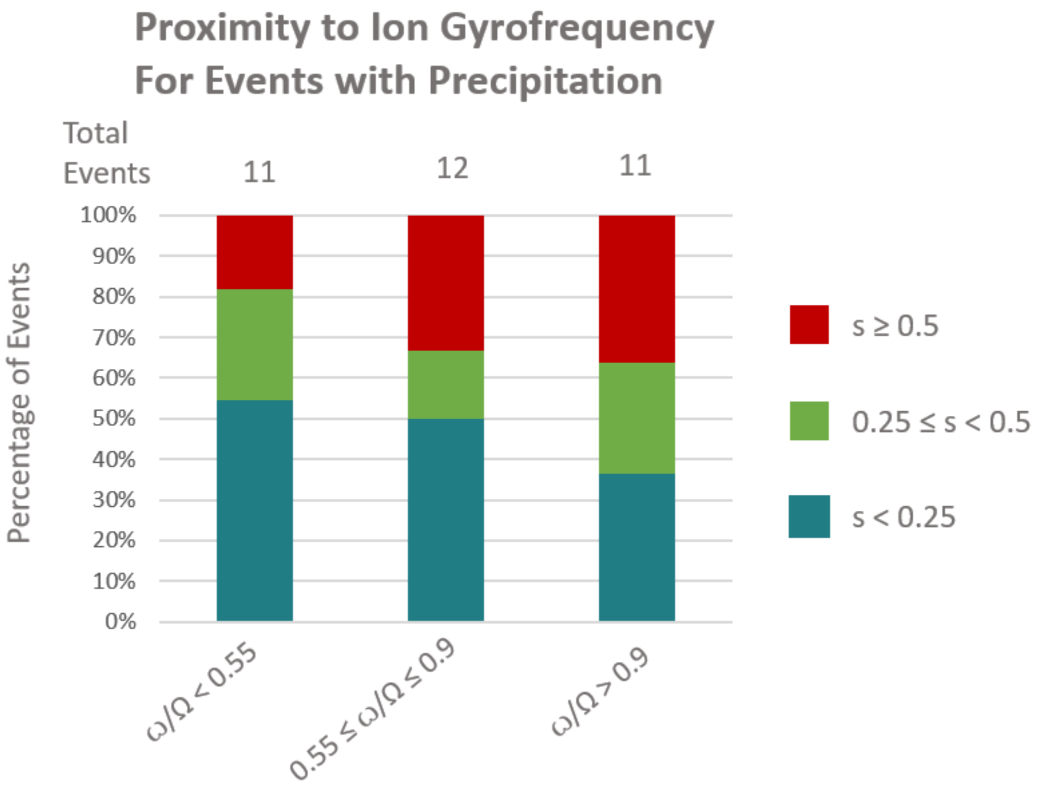

Figure 4.6: Proximity of EMIC wave frequency (ω) to the local ion gyrofrequency (Ω) for events that resulted in a precipitation event, in association with scattering score, s.

gyrofrequency the wave event is more likely to have a scattering score of $s \geq 0.5$. Similarly, for wave events further from the ion gyrofrequency, a low scattering score ($s < 0.25$) is more likely.

Figure 4.7 compares the REP events with the electron plasma density measured by EMFISIS on the Van Allen Probes. The left side of the figure compares the density with the REP event count rate. There is an almost even distribution of REP events between the lowest count rate and highest count rate, with the median count rate having the highest fraction of mid-range and high electron density. The right side of the figure compares the density with $RE15$. For the lowest values of $RE15$, there are no events associated with high density, and the fraction of low density events is roughly the same for the lowest $RE15$ and the highest $RE15$.

A more interesting relationship might exist between the precipitation events and the

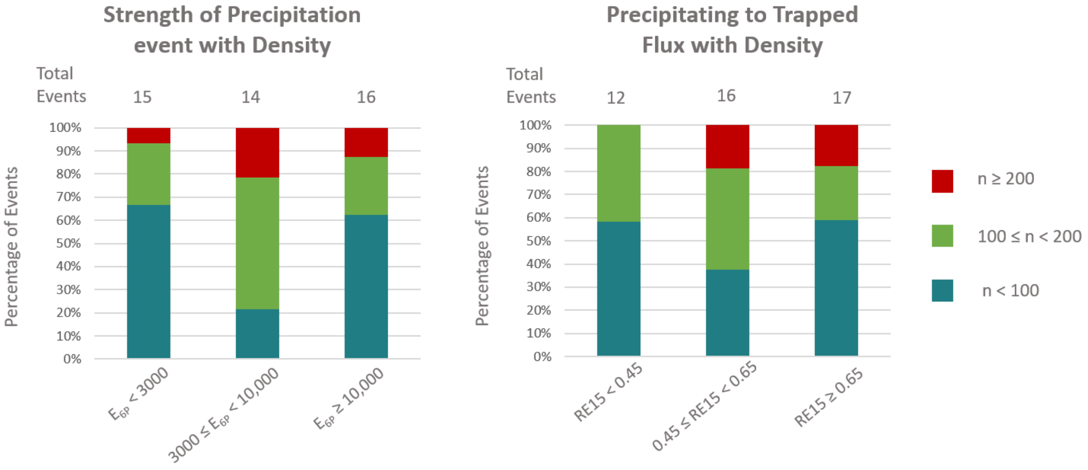

Figure 4.7: (Left) Strength of precipitation event c, in counts per second, in association with electron plasma density, $n(cm^{-3})$, measured by the EMFISIS instrument on RBSP. (Right) Precipitating-to-trapped ratio, R, of precipitation event, in association with electron plasma density measured by the EMFISIS instrument on RBSP.

ratio of the electron plasma frequency and the electron gyrofrequency (ω_{pe}/Ω_e). It has been suggested that minimum resonant energies reaching below 2.0 MeV might only be possible where $\omega_{pe}/\Omega_e \geq 10$, corresponding to regions of lower magnetic field strength and higher plasma density (Meredith et al., 2003; Summers & Thorne, 2003; Sandanger et al., 2007). Therefore, it may be reasonable to expect a positive correlation between a higher $RE15$ and a higher ω_{pe}/Ω_e, as a lower E_{min} should free up a larger portion of the electron population to be scattered. Figure 4.8 shows the trend between the precipitating-to-trapped electron ratio, *RE15*, and ω_{pe}/Ω_e, extracted from Level4 EMFISIS data. This figure shows that REP events with higher *RE15* were more likely to be associated with smaller ω_{pe}/Ω_e than events with lower RE15. Similarly, there were a higher proportion of events with high ω_{pe}/Ω_e for lower *RE15* than for higher *RE15*.

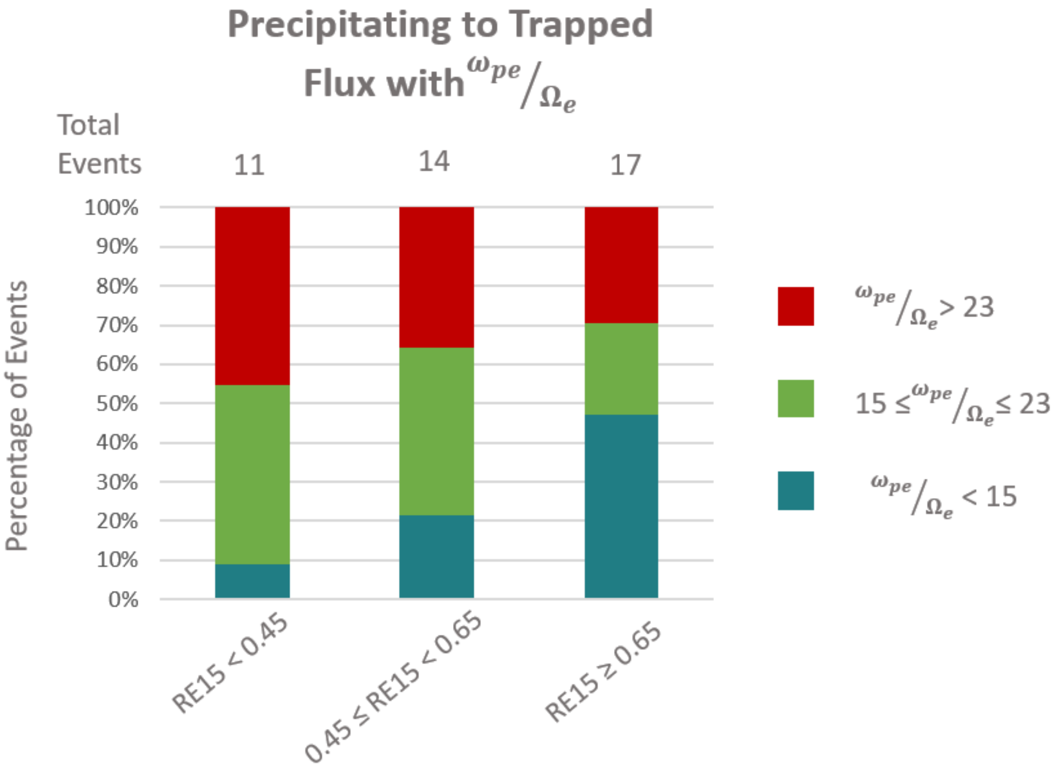

Figure 4.8: Precipitating-to-trapped ratio, RE15, of precipitation event, in association with the ratio of the electron plasma frequency to the electron gyrofrequency.

4.5 Discussion

This investigation sought out to provide direct quantitative evidence connecting EMIC wave-driven scattering signatures to real radiation belt losses. This was achieved by searching for evidence of relativistic electron precipitation in POES/MetOp data when the spacecraft were in conjunction with EMIC waves observed by the Van Allen Probes. The first notable result is that the EMIC wave to REP event coincidence rate found here is in general consistent with what has been reported in literature previously. Qin et al. (2019) reported a coincidence rate of 27%, while Qin et al. (2020) found a coincidence rate of 34% in an extended statistical analysis.

The increased rate reported here in comparison to these studies may have a number of explanations. For one, the event selection criteria used here does not depend on the precipitating count rate, as is traditionally used. Instead, it relies solely on an increase in the precipitating-to-trapped electron ratio as an indicator of scattering. Leaving out REP events that did not trigger the electron count rate would have resulted in a coincidence rate of 6% less. Another reason why the coincidence rate reported here might be higher than previously reported is that the selection criteria is independent of concurrent proton precipitation. While the concurrent precipitation of MeV electrons and 10s of keV protons is often used as an indicator of EMIC wave activity, it was left out in this study because it was found that in many cases, evidence of curvature scattering resulted in high precipitating count rates masking any spikes due to EMIC waves. Roughly one third of the electron precipitation events did not have concurrent proton precipitation. Leaving these events out would result in a decrease of the EMIC wave - REP coincidence rate by 13%. Confidence in the strategy to leave out this proton precipitation requirement and still be able to attribute the REP events to EMIC waves comes from the strict conjunction interval criteria that provides sufficient evidence that the REP event is a result of the EMIC wave. It is reasonable to suggest that requiring the concurrent spikes may result in an undercounting of the EMIC-wave - REP coincidence rate.

With the coincidence rate established, it becomes important to understand the conditions that influence the REP events. This is done by comparing the REP events with the EMIC wave-driven scattering signatures discussed in Chapter 3. In general it was found that strong relativistic electron precipitation events (measured by the precipitating count rate) are associated with EMIC waves that drove scattering signatures with higher s scores in the radiation belts. REP events were just as likely to occur for EMIC wave events with $s < 0.25$ as with $0.25 \geq s < 0.5$. The three case studies presented in the beginning of Section 4.4 are representative of this fact. Events 34 and 91, which both had scattering scores of $s \geq 0.5$ resulted in positive detection of a precipitation event, while Event 2, which has a low scattering score, did not. Since the scattering score is a measure of how well a scattering signatures is visually identifiable and how well its shape can be predicted by cold plasma theory, this result suggests that the more pronounced a scattering signature appears in the equatorial pitch angle distribution, the more significant the precipitation spike is. On the other hand, from the fact that there are REP events associated with low scattering score events, it is apparent that clear bite-out scattering signatures are not necessary for precipitation to occur. Precipitation may, in fact occur for these types of events. What is clear is that a high scattering score ($s \geq 0.5$) is a dominant factor in a REP event being observed. This is also supported by the fact that REP events with higher count rates and precipitating-to-trapped ratios were more likely to result from EMIC wave scattering events with high scattering scores.

Figure 4.6 may provide one reason why larger scattering scores result in more significant REP events. It is known that as the frequency of an EMIC wave approaches the ion gyrofrequency, the minimum resonant energy is decreased. Since the flux of a population of radiation belt electrons increases with decreasing energy, it follow that a lower E_{min} can result in greater counts of precipitating electrons. Figure 4.6 shows that higher scattering scores are most likely to result from waves closer to the gyrofrequency. Combining this observation with the relationship in Figure 4.5 suggests that higher scattering scores result in stronger precipitation in terms of count rate. This may explain why Qin et al. (2020) saw increased coincidence rates when the EMIC waves approach the ion gyrofrequency. What is interesting to note is that the more significant correlation between precipitation and scattering signatures exists with the proximity to the gyrofrequency, and not, as might be expected, with background plasma density. Previous studies have linked plasma density with REP, though it is likely that the dependence between the two is limited to the formation of the EMIC waves, and not on the ability of the EMIC waves to scatter relativistic electrons into the loss cone. The lack of a clear correlation in Figure 4.7 supports this idea.

The relationship in Figure 4.8 is at contrary to initial presumptions. It was expected that lower minimum resonant energies (which might result in higher *RE15*) should occur during periods of higher ω_{pe}/Ω_e (Meredith et al., 2003; Summers & Thorne, 2003; Sandanger et al., 2007). Figure 4.8 shows the opposite. This apparent contradiction can be explained by considering that lower ω_{pe}/Ω_e ratios have been associated with more active times (Agapitov et al., 2020). More active times were also connected to stronger scattering signatures in Chapter 3, and stronger scattering signatures were found to result in precipitation events with higher precipitating-to-trapped flux ratios in Chapter 4. By transitive logic, this suggests that more active times should result in higher precipitating-to-trapped flux ratios. This is confirmed in Figure 4.9, which shows a slight trend that there is an increased proportion of high AE intervals associated with high *RE15*. The weakness of the trend is likely due to the low number of events. It follows that as more active times are associated with lower ω_{pe}/Ω_e, lower ω_{pe}/Ω_e might actually be associated with higher *RE15*. This is in fact what is seen in Figure 4.8.

The EMIC wave - REP connection through the context of geomagnetic activity deduced here is consistent with many previous observations (Horne et al., 2009; Carson et al., 2013; Douma et al., 2018) and provides additional insight into why this is the case. The observations presented here suggest that REP events occur during active times, not only because of increased EMIC activity, but also due to an increased likelihood for the EMIC waves to result in notable scattering signatures. Since the observations in this study took place during relatively quiet conditions (no evidence of geomagnetic storms) it may be the case that the coincidence rate reported here may be used as a lower bound for estimating the impact that EMIC waves have on the radiation belts. Under more active conditions the coincidence rate using this methodology may be larger.

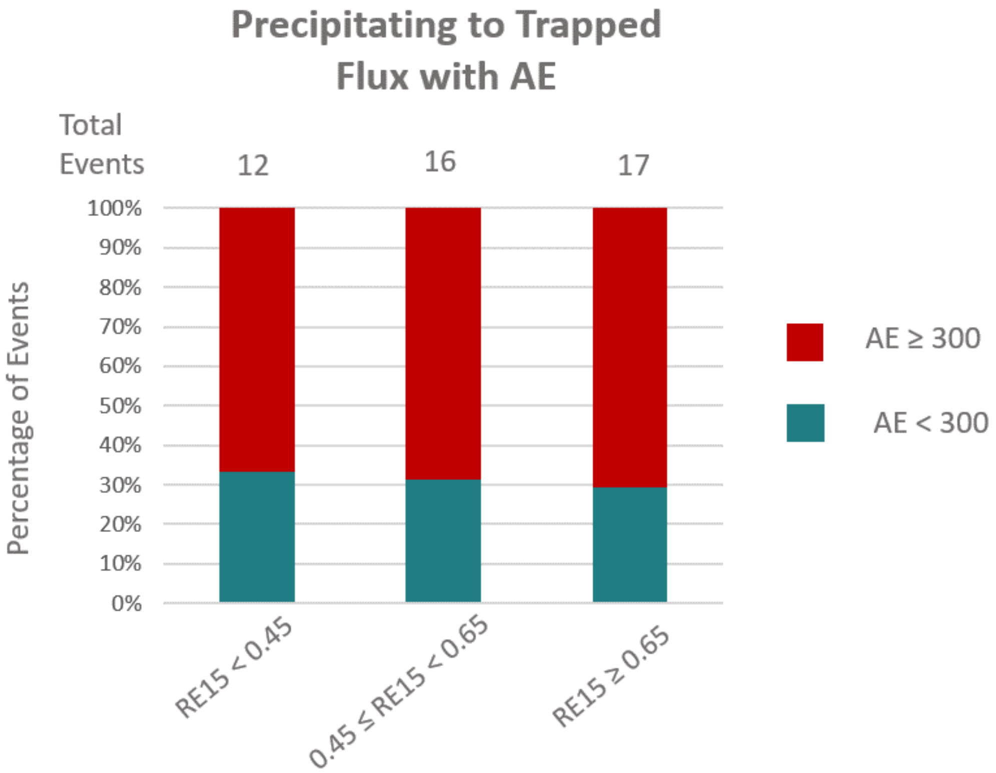

Figure 4.9: Precipitating-to-trapped ratio, RE15, of precipitation events in association with AE activity.

It was also found in Chapter 3, that EMIC waves with greater wave power resulted in higher scattering signatures. By a similar logic, stronger EMIC waves are more likely to result in stronger REP events. This is also consistent with previous observations, however, it remains unclear why this is the case. Since the wave power does not affect the pitch angle cutoffs of scattering, and the simultaneous observation of the waves and scattering signatures already implies strong diffusion timescales, it seems reasonable that the stronger precipitation related to stronger EMIC waves is not an artifact of E_{min} or diffusion timescale.

The key findings of this chapter are summarized as follows:

1. The coincidence rate between EMIC waves and REP events is 38%.
2. Relativistic electron precipitation events preferably occur for EMIC wave events that created scattering signatures with $s \geq 0.5$.
3. The strength of REP events in counts/s is typically greater for scattering signatures with $s \geq 0.5$.
4. The precipitating-to-trapped electron ratio, $RE15$, is typically greater for scattering signatures with $s \geq 0.5$.
5. The strength and $RE15$ of REP events is correlated with proximity to ion gyrofrequency while no significant correlation exists with electron plasma density.
6. Precipitation events are more likely to result from EMIC waves with larger wave power and those generated during more active geomagnetic conditions.

The concluding chapter will comment on the implications this has on the field of radiation belt dynamics and comment on the opportunity for future work.

CHAPTER 5

Conclusions and Future Work

5.1 Conclusions

This dissertation presents a comprehensive quantitative study statistically connecting EMIC wave-driven scattering signatures with radiation belt depletion. This was done by systematically addressing three key questions related to the physics of EMIC waves. The focus of Chapter 2 was to address the first question: *How is EMIC wave activity related to outer radiation belt relativistic electron pith angle distributions and observed fluxes?* A single EMIC wave event case study was presented. The EMIC wave event was a strong helium-band wave that was captured by RBSP-A in February 2017. The event occurred during a time of enhanced conditions preferential for EMIC wave growth. Observed simultaneously with the wave was an energy and pitch angle dependent bite-out scattering signature. To confirm that this bite-out was a result of pitch angle scattering by the observed EMIC wave, rough estimations of the minimum resonant energy and pitch angle scattering cutoffs were made using the cold plasma dispersion relation. The minimum resonant energy was found to be roughly ~ 2.0 MeV indicating that evidence of scattering should be present in the pitch angle distributions of electrons with energy $E \geq\sim 2.0$ MeV. Qualitatively, this matched what could be seen in the REPT data by eye. By overplotting the pitch angle cutoff estimations on the REPT data, it was found that the estimations were in good agreement with the bite-outs. This provided strong support that the bite-out was in fact created by the observed EMIC wave. By inspecting the drift shell region corresponding to the location of the wave ($L^* \pm 5.0$) a few hours before and after the main observation, it was found that the scattering signature developed over the course of a few hours during a period of sustained

EMIC activity. Three main conclusions were drawn from these observations in support of the motivating question:

1. Electromagnetic ion cyclotron waves and their effect on megaelectronvolt electrons are highly localized in L.
2. The presence of electromagnetic ion cyclotron waves can be inferred from their effect on the electron pitch angle distribution.
3. Electromagnetic ion cyclotron waves can have lasting impacts on radiation belt dynamics.

This new understanding about the impacts of relativistic electrons on the radiation belts can be directly observed in pitch angle distributions motivated the next inquiry.

Chapter 3 expanded the work done in Chapter 2 to a statistical analysis to address the second question: *Do EMIC waves drive scattering signatures of core populations* ($\leq\sim 2MeV$) *of outer radiation belt electrons, and what are the preferred conditions to influence these signatures?* In this line of questioning, core populations mean electrons with energies $E \leq\sim$ 2.0 MeV. From the case study in Chapter 2, it was seen that these core populations were in fact affected by the EMIC wave, but the interaction was limited to field aligned particles at these energies. This statistical investigation relied on the development of a standard measure of how well predicted pitch angle cutoffs predict an EMIC-wave driven scattering signature. This scattering signature score technique uses the same methods as the analysis in Chapter 2, but with some improvements and automation. The technique was applied to a set of EMIC waves captured by the Van Allen Probes during a period of 4 months when the spacecraft were near the dusk-side plasmasphere. The observations included a median minimum resonant energy that fell below 2.0 MeV in $\sim 28\%$ of EMIC wave events surveyed. In addition to determining the E_{min}, scattering signatures were identified and analyzed associated with the wave events. The key findings are summarized as:

1. EMIC waves are capable of driving loss of core electron populations about a third of the time during quiet conditions.
2. Approximately 46% of EMIC wave events were co-located with relativistic electron pitch angle scattering signatures.
3. The presence of scattering signatures is dependent on geomagnetic activity and wave

power, with increases in each being preferable for the creation of the signatures.

Lastly, Chapter 4 asks the final question needed to provide the end-to-end picture of EMIC wave-driven relativistic electron losses: *To what extent are EMIC wave-driven scattering signatures associated with relativistic electron precipitation events and what are the intensities of these precipitation events?* Chapter 4 took the EMIC events and scattering signatures identified in Chapter 3 and associated them with relativistic electron precipitation events observed by polar orbiting spacecraft. This additional dataset provides direct evidence of radiation belt losses resulting from the EMIC waves. The study was accomplished by automatically detecting precipitation events in conjunction with the EMIC events triggered by increases in the precipitating to trapped electron ratio. These precipitation events were compared with the scattering signatures determined in Chapter 3. The major conclusions of this chapter are:

1. The EMIC wave to relativistic electron precipitation event coincidence rate is 38%.
2. Precipitation events are preferentially identified for EMIC wave events that resulted in strong scattering signatures.
3. Stronger precipitation events are associated with EMIC waves closer to the ion gyrofrequency and with higher scattering scores.

In summary, this dissertation shows through direct quantitative evidence that EMIC waves can drive losses of core radiation belt electrons, and that these losses can be indirectly observed through bite-out scattering signatures and directly observed with associated relativistic electron precipitation. Figure 5.1 summarizes the end-to-end relationships of EMIC wave-driven relativistic electron losses discovered throughout this work.

5.2 Future Work

The research presented in this dissertation opens up new avenues for improved research into the impacts EMIC waves have on the radiation belts. Most immediately, this work demonstrates that EMIC wave activity as well as EMIC wave-driven losses can be inferred from relativistic electron pitch angle distributions. The localized nature of EMIC waves

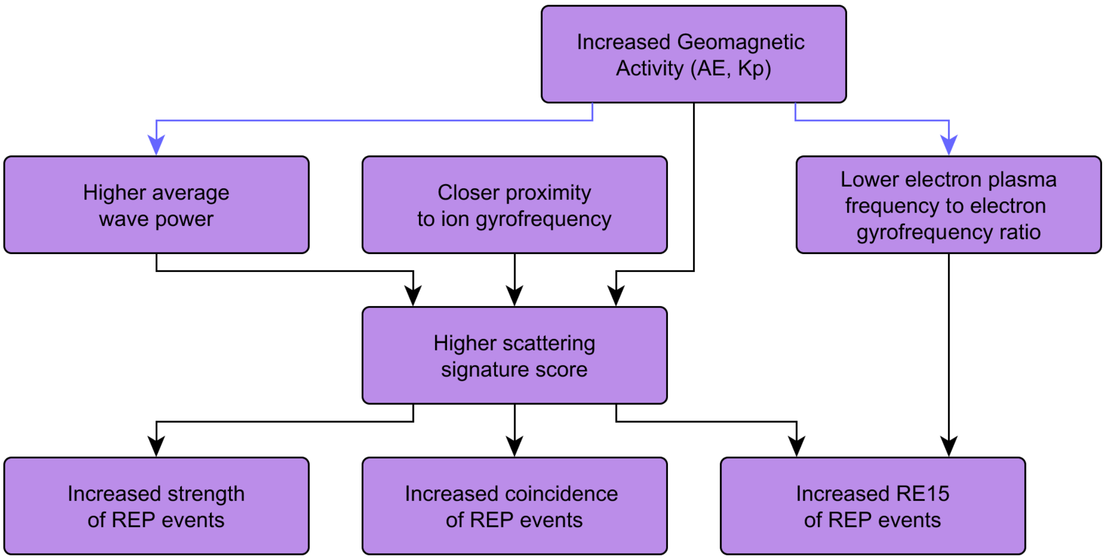

Figure 5.1: End-to-end description of the EMIC wave-driven relativistic electron loss process as determined in this work. Black arrows represent relationships uncovered by the studies presented in this dissertation, while the blue arrows represent relationships that were previously known and well supported.

makes them highly elusive and often difficult to capture and study. The technique of using scattering signatures as a proxy for EMIC activity can lead to increased opportunity to investigate radiation belt losses.

Related, there are significant opportunities for increased fidelity in predicting scattering signatures. The work presented here limited the analysis to cold plasma approximations, however, the inclusion hot plasma effects can improve the prediction of EMIC wave-scattering signatures. Additional improvements can come from increased precision in ion composition ratios (which are traditionally difficult to measure due to the cold temperature of the ions), plasma density estimations, as well as the inclusion of non-linear scattering effects. It has been suggested that non-linear interactions between EMIC waves and electrons may play a significant role in influencing scattering into the loss cone. Albert and Bortnik (2009), for example, found using a test particle analysis that non-linear interactions can lead to scattering away from the loss cone. This effect could explain why some EMIC wave events were not associated with expected scattering signatures. This effect is likely more significant with larger amplitude waves (Liu et al., 2010). On the other hand, some investigations have shown the potential for non-linear resonances to increase losses, particularly in cases of harmonic resonance (G. Wang et al., 2017). In future studies, it will be valuable to consider how these non-linear interactions relate to precipitation events.Such improvements can lead to increased accuracy of scattering signature predictions.

This increased accuracy can then be paired with newer and higher resolution measurements of precipitating electrons. Although useful for a first order indication of precipitation, the POES MEPED instrument suffers a number of issues that limit the comparison to scattering signatures that can be performed. As discussed in Chapter 4, the P6 detector is sensitive to electrons with energies $E > 0.7$ MeV (Yando et al., 2011). Above this lower bound energy, MEPED cannot distinguish further between different energy populations. A truer comparison between the scattering signatures captured by REPT and relativistic electron precipitation events could come from particle instrumentation designed with increased resolution of electrons in the energy range between 0.5 and 5.0 MeV. Additional shortcomings of the MEPED instrument come from not only a lack of sufficient angular resolution to extract a pitch angle distribution (the detectors have a field of view of $\pm 15^\circ$ (Evans & Greer, 2000)), but also from uncertainties in the pitch angle populations being measured by the two orthogonal detectors. C. Rodger et al. (2010) reported that the particle populations sampled by the detectors are dependent on location. The 0° detector, normally samples only the bounce loss cone, but at lower latitudes can sample the drift loss cone as well, potentially including populations of electrons that are becoming lost due to other processes besides EMIC wave-driven scattering. Additionally, at very high latitudes, the 0° detector cannot observe the full bounce loss cone, so reported fluxes will not fully correspond to the entire precipitating population. The 90° detector similarly lacks some consistency in the population it is sampling as well. At many locations, this detector samples a mix of trapped and precipitating particles, introducing some unreliability in using the detector as a pure measurement of trapped particles. A more recent analysis of the MEPED instrument performed by Selesnick et al. (2020) emphasizes the inaccuracies of using the 0° telescope to fully represent the precipitating electron population. In this study, angular response functions show that the 0° detector is more sensitive to electrons at high incident angles, corresponding to populations that can be measured by the 90° detector. This can result in an over estimation of the precipitating fluxes.

Many of these issues with comparing the scattering signatures with relativistic electron precipitation can be addressed by emerging and improved datasets. The EPD-E instrument, flying on the ELFIN Mission (Angelopoulos et al., 2020) that launched into low-Earth orbit in 2018, was designed to measure electron precipitation due to EMIC wave-driven scattering. This detector has an energy range of 50 keV - 5 MeV with a $\delta E/E \sim 40\%$ and an additional integral channel for greater than 5 MeV. The EPDE full-width half max of the detector response is 33.75°, providing an ideal data set for future studies comparing scattering signatures with relativistic electron precipitation events. The success of this mission also highlights the affordability and utility of expanding the number of low-Earth orbiting particle detectors which will broaden the opportunity for coincident EMIC wave and relativistic electron precipitation observations such as those presented in this dissertation.

Combining the knowledge gained from this dissertation with the new methods for analyzing scattering signatures and new data sets can lead to significant improvements in understanding the variability of the radiation belts. Ultimately, this leads to increased fidelity of space weather modelling and forecasting capabilities and improved situational awareness for our space-based assets.

APPENDIX A

Supplemental Information

A.1 Geomagnetic Conditions

The catalog of EMIC waves used in Chapters 3 and 4 were observed during the months of February through May of 2017. For most of this time period geomagnetic conditions were relatively calm (see Figure A.1). With the exception of three instances, the Sym-H parameter remained above -50 nT and showed no indication of major geomagnetic storms. The Kp index was typically below 4, also indicating quiet to moderate storm activity. The AE index shows multiple occurrences of increases in auroral activity, but only rising above 1000 nT at the end of May. The bottom panel of Figure A.1 shows the times when EMIC waves were observed by the Van Allen Probes for comparison with the geomagnetic conditions. In general, the occurrence of EMIC wave events clustered around increased AE activity, which is consistent with increased substorm injection that can drive the anisotropy need to excite EMIC waves. It is noted that at the time of the largest change in all geomagnetic parameters towards the end of May 2017, there was not sufficient data to determine scattering scores for the associated EMIC waves.

A.2 Scattering Signature Methodology

The following figures provide insight to the scattering signature methodology, using Event 34 as an example. Figure A.2 shows how the frequency of the EMIC was is automatically selected using the criteria described in Chapter 3. The black dots in the top panel show the frequency of the wave that is selected for the analysis. The middle panel shows the

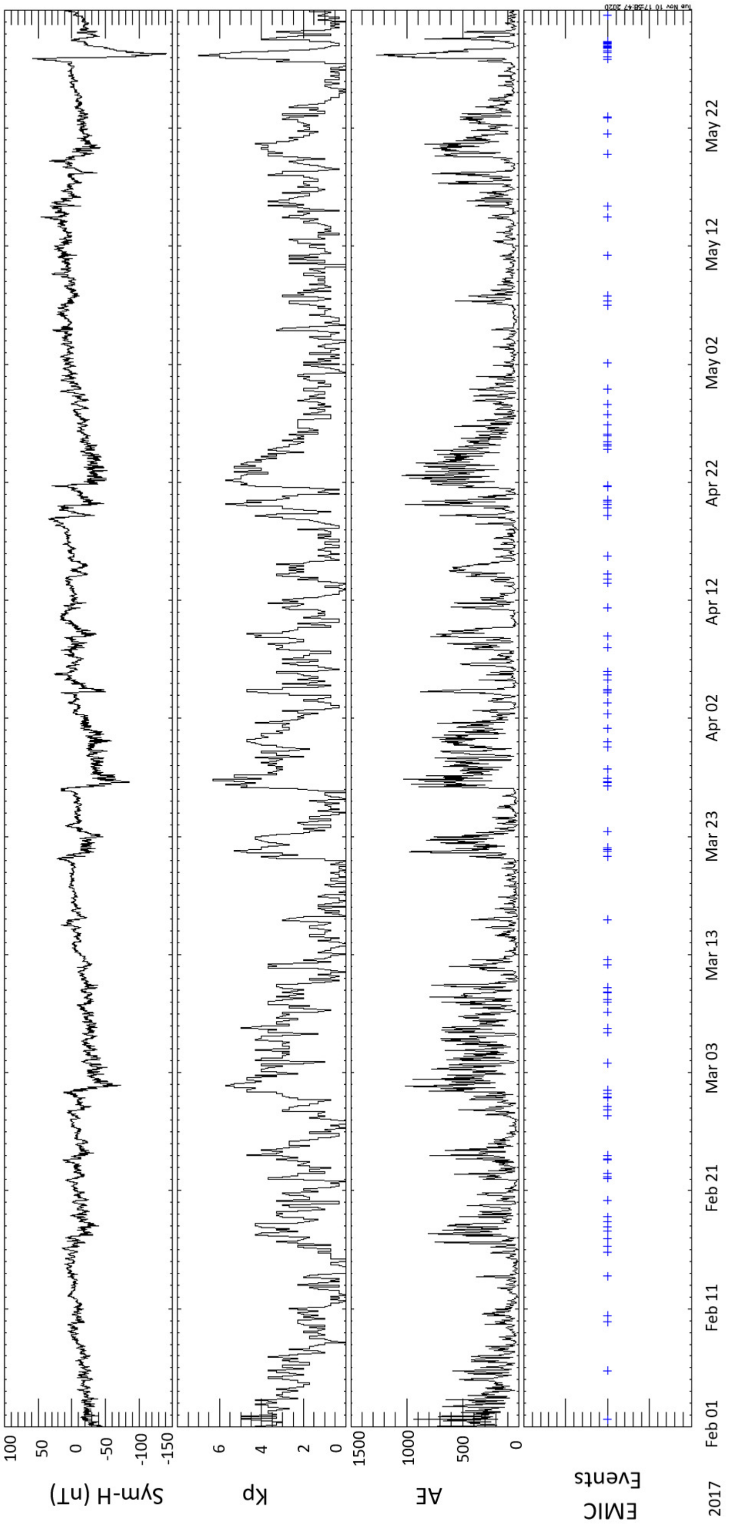

Figure A.1: Geomagnetic conditions during the four-month study. The blue '+' symbols indicate the times that EMIC waves were observed by either RBSP-A or RBSP-B.

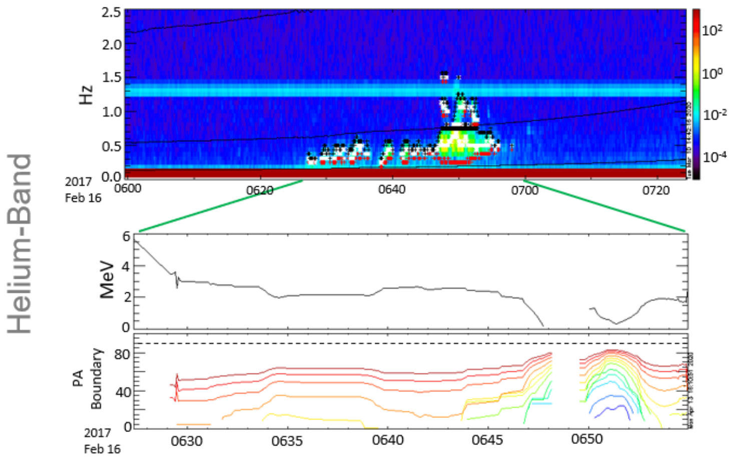

Figure A.2: Steps 1 and 2 of the scattering signature methodology applied to Event 34.

derived minimum resonant energy for the full duration of the helium-band wave. The bottom panel presents the resulting maximum pitch angle at different electron energies (red colors representing higher energies.)

Figure A.3 overplots the pitch angle cutoffs for both the helium-band (dashed lines) and proton-band (solid lines) waves on the pitch angle bite-out in the REPT data. It can be seen in this figure that the shape of the bite-out is mostly dictated by the helium-band wave.

Figure A.4 visually represents how the K-S statistic is determined, by showing the comparison between the bite-out distribution and the undisturbed distribution (pre-bite out). The left side of the panel shows the normalized flux as a function of pitch angle, while the right side shows the resulting K-S Significance Level. It is clear from this figure that the greater the difference between the bite-out distribution and the undisturbed distribution, the lower the significance level.

A.3 Temperature Effects on EMIC Wave Propagation

The excitation and propagation of EMIC waves is often described using assumptions that the wave exists in a cold (a few eV), uniform plasma (Albert, 2003; Summers & Thorne, 2003; Summers et al., 2007a, 2007b). Under this treatment, solving the dispersion relation (given

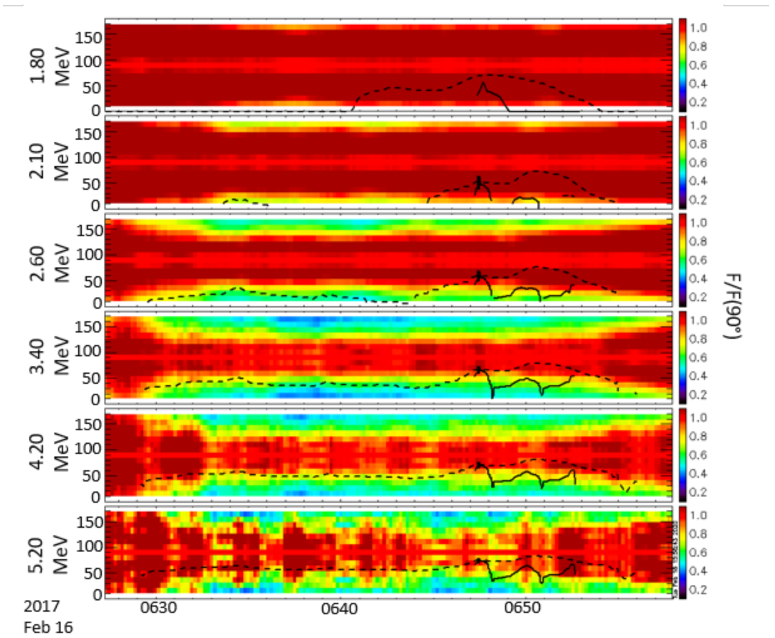

Figure A.3: Step 3 of the scattering signature methodology applied to Event 34. The dashed black lines are the pitch angle boundary estimates for the helium-band wave and the solid black lines are the pitch angle boundary estimates for the proton-band wave.

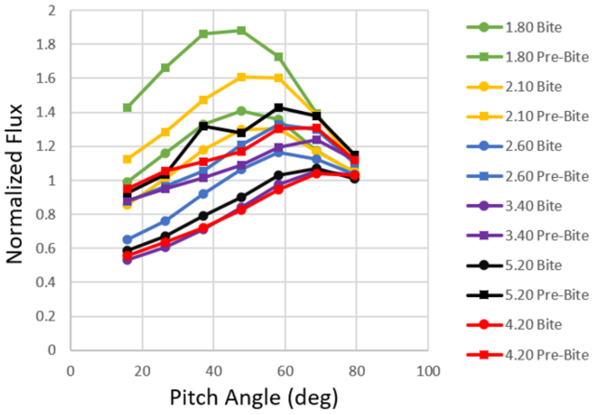

K-S Statistic Significance Level

1.80 MeV	0.02750
2.10 MeV	0.12870
2.60 MeV	0.42322
3.40 MeV	0.12866
4.20 MeV	0.00417
5.20 MeV	0.02750

Figure A.4: Step 4 of the scattering signature methodology applied to Event 34.

in Chapter 1 by Equation 1.3) for wave frequencies at or near the gyrofrequencies will result in imaginary values for the wave vector k. This suggests that within these frequency ranges, or stop-bands, field-aligned wave propagation is not possible. The location of the stop-bands can be roughly predicted if, among other variables, the ion density and electron density is known (Albert, 2003). Typically, these stop-bands start just before the ion gyrofrequencies and extend through the cutoff frequencies (Summers & Thorne, 2003). Outside of the stop-bands, as the wave frequency increases towards the ion gyrofrequency, the wave vector k approaches infinity which can result in an unrealistically low estimation of E_{min} if hot plasma affects are ignored.

Whereas the cold plasma approximation can provide a useful simplified description of EMIC wave propagation, the inclusion of hot plasma effects in some cases, for example, when the hot proton density becomes comparable to the cold plasma density, can significantly alter the estimation of the wave vector k. Silin et al. (2011) investigated the thermal effects on EMIC wave interaction with electrons using the kinetic dispersion relation, Equation A.1, where A_j is the temperature anisotropy and v_{Tj} is the thermal velocity.

$$\Omega^2 = c^2k^2 - \sum_j \omega_{pj}^2(A_j) - ((A_j+1)(\Omega_j - \Omega) - \Omega_j)\frac{Z(z_j)}{kv_{Tj}} \tag{A.1}$$

Using this treatment, Silin et al. (2011) found that when thermal effects are included, EMIC waves can be excited at the ion gyrofrequencies and within the stop bands. Additionally, k remains finite near the ion gyrofrequencies, preventing E_{min} from dropping unrealisitcally low. Chen et al. (2013) similarly evaluated the effects of using an improved dispersion relation that retained thermal terms, and compared the results to estimations from the CPA. This study found the CPA works well in H+ plasmas, but significant differences between the kinetic description and cold plasma description occur for He+ waves in a H+-He+ plasma near the helium gyrofrequency. As a result, Chen et al. (2013) suggests that estimations for k found using the CPA for wave frequencies near the helium gyrofrequency might be poor.

Throughout these chapters, estimations for the minimum resonant energy an pitch angle cutoffs for observed EMIC waves are based on solving the CPA for the wave vector k. The dispersion relation for the CPA was chosen not just for its relative simplicity, but also because it produced reasonable approximations for pitch angle cutoffs that could be verified by eye in test cases. As noted in Chapter 3, for EMIC waves that had frequencies at the ion gyrofrequencies, the wave frequency selected was 0.05 Hz below Ωj to avoid the CPA issues discussed above, while maintaining the computational simplicity provided by using the CPA. The selection of 0.05 Hz for subtracting from Ω_j was empirically chosen using a sample of test cases. In these test cases, this choice resulted in a frequency selection that was just outside the stop-band, providing a real solution for k for the majority of the wave duration. This technique allowed for the evaluation of more EMIC wave events that would have otherwise been unusable. It is noted, however, that future efforts in estimating EMIC wave scattering signatures might be improved by incorporating kinetic plasma effects in the approximation of k.

References

Adair, L., Angelopoulos, V., Sibeck, D., Zhang, X., & Halford, A. (2020). A statistical examination of emic wave-driven electron pitch angle scattering signatures. *submitted to: Journal of Geophysical Research: Space Physics*.

Agapitov, O., Mourenas, D., Artemyev, A., Claudepierre, S. G., Hospodarsky, G., & Bonnell, J. W. (2020). Lifetimes of relativistic electrons as determined from plasmaspheric hiss scattering rates statistics: Effects of ω_{pe}/ω_{ce} and wave frequency dependence on geomagnetic activity. *Geophysical Research Letters*, *47*(13), e2020GL088052. doi: 10.1029/2020GL088052

Albert, J. M. (2003, Jan). Evaluation of quasi-linear diffusion coefficients for EMIC waves in a multispecies plasma. *Journal of Geophysical Research*, *108*(A6), 9. doi: 10.1029/2002JA009792

Albert, J. M., & Bortnik, J. (2009, June). Nonlinear interaction of radiation belt electrons with electromagnetic ion cyclotron waves. *Geophysical Research Letters*, *36*(12), L12110.

Angelopoulos, V., Cruce, P., Drozdov, A., Grimes, E. W., Hatzigeorgiu, N., King, D. A., & et al. (2019, Jan 22). The Space Physics Environment Data Analysis System (SPEDAS). *Space Science Reviews*, *215*(1), 9. doi: 10.1007/s11214-018-0576-4

Angelopoulos, V., Sibeck, D., Carlson, C. W., McFadden, J. P., Larson, D., Lin, R. P., … Sigwarth, J. (2008, Dec). First results from the themis mission. *Space Science*, *141*, 453. doi: 10.1007/s11214-008-9378-4

Angelopoulos, V., Tsai, E., Bingley, L., & Shaffer, C. (2020). The ELFIN Mission. *Space Science Reviews*. doi: 10.1007/s11214-020-00721-7

Asikainen, T., Mursula, K., & Maliniemi, V. (2012). Correction of detector noise and recalibration of noaa/meped energetic proton fluxes. *Journal of Geophysical Research: Space Physics*, *117*(A9). doi: 10.1029/2012JA017593

Auster, H. e. a. (2008). *The themis fluxgate magnetometer* (Vol. 141; Tech. Rep.). doi: 10.1007

Baker, D. N., Blake, J. B., Callis, L. B., Cummings, J. R., Hovestadt, D., Kanekal, S., … Zwickl, R. D. (1994). Relativistic electron acceleration and decay time scales in the inner and outer radiation belts: Sampex. *Geophysical Research Letters*, *21*(6), 409-412. doi: 10.1029/93GL03532

Baker, D. N., Blake, J. B., Klebesadel, R. W., & Higbie, P. R. (1986). Highly relativistic electrons in the earth's outer magnetosphere: 1. lifetimes and temporal history 1979–1984. *Journal of Geophysical Research: Space Physics*, *91*(A4), 4265-4276. doi: 10.1029/JA091iA04p04265

Baker, D. N., Kanekal, S. G., Horne, R. B., Meredith, N. P., & Glauert, S. A. (2007). Low-altitude measurements of 2–6 mev electron trapping lifetimes at $1.5 \leq l \leq 2.5$. *Geophysical Research Letters*, *34*(20). doi: 10.1029/2007GL031007

Baker, D. N., Kanekal, S. G., Hoxie, V. C., Batiste, S., Bolton, M., Li, X., … Friedel, R. (2012, December). The Relativistic Electron-Proton Telescope (REPT) Instrument on Board the Radiation Belt Storm Probes (RBSP) Spacecraft: Characterization of Earth's Radiation Belt High-Energy Particle Populations. *Space Sci. Rev.*. doi: 10.1007/s11214-012-9950-9

Belian, R. D., Gisler, G. R., Cayton, T., & Christensen, R. (1992). High-z energetic particles at geosynchronous orbit during the great solar proton event series of october 1989. *Journal of Geophysical Research: Space Physics*, *97*(A11), 16897-16906. doi: https://doi.org/10.1029/92JA01139

Bingley, L., Angelopoulos, V., Sibeck, D., Zhang, X., & Halford, A. (2019). The evolution of a pitch-angle "bite-out" scattering signature caused by emic wave activity: A case study. *Journal of Geophysical Research: Space Physics*, *124*(7), 5042-5055. doi: 10.1029/2018JA026292

Blake, J. B., Carranza, P. A., Claudepierre, S. G., Clemmons, J. H., Crain, W. R., Dotan, Y., … Zakrzewski, M. P. (2013, June). The Magnetic Electron Ion Spectrometer (MagEIS) Instruments Aboard the Radiation Belt Storm Probes (RBSP) Spacecraft. *Space Sci. Rev.*. doi: 10.1007/s11214-013-9991-8

Blum, L. W., Halford, A. J., Millan, R., Bonnell, J. W., Goldstein, J., Usanova, M., … Li,

X. (2015, July). Observations of coincident EMIC wave activity and duskside energetic electron precipitation on 18–19 January 2013. *Geophysical Research Letters*, *42*(14), 5727–5735.

Blum, L. W., Macdonald, E. A., Gary, S. P., Thomsen, M. F., & Spence, H. E. (2009, Oct). Ion observations from geosynchronous orbit as a proxy for ion cyclotron wave growth during storm times. *Journal of Geophysical Research*, *114*(A10), A10214.

Bortnik, J., Cutler, J. W., Dunson, C., & Bleier, T. E. (2007). An automatic wave detection algorithm applied to pc1 pulsations. *Journal of Geophysical Research: Space Physics*, *112*(A4). doi: 10.1029/2006JA011900

Bortnik, J., Thorne, R. M., O'Brien, T. P., Green, J. C., Strangeway, R. J., Shprits, Y. Y., & Baker, D. N. (2006). Observation of two distinct, rapid loss mechanisms during the 20 november 2003 radiation belt dropout event. *Journal of Geophysical Research: Space Physics*, *111*(A12). doi: https://doi.org/10.1029/2006JA011802

Cao, Shprits, Y. Y., Ni, B., & Zhelavskaya, I. S. (2017). Scattering of ultra-relativistic electrons in the van allen radiation belts accounting for hot plasma effects. *Nature*.

Cao, X., Ni, B., Summers, D., Bortnik, J., Tao, X., Shprits, Y. Y., ... Wang, Q. (2017). Bounce resonance scattering of radiation belt electrons by h+ band emic waves. *Journal of Geophysical Research: Space Physics*, *122*(2), 1702-1713. doi: 10.1002/2016JA023607

Capannolo, L., Li, W., Ma, Q., Zhang, X.-J., Redmon, R. J., Rodriguez, J. V., ... Reeves, G. D. (2018). Understanding the driver of energetic electron precipitation using coordinated multisatellite measurements. *Geophysical Research Letters*, *45*(14), 6755-6765. doi: 10.1029/2018GL078604

Carson, B. R., Rodger, C. J., & Clilverd, M. A. (2013). Poes satellite observations of emic-wave driven relativistic electron precipitation during 1998–2010. *Journal of Geophysical Research: Space Physics*, *118*(1), 232-243. doi: 10.1029/2012JA017998

Chen, L., Thorne, R. M., & Bortnik, J. (2011, August). The controlling effect of ion temperature on EMIC wave excitation and scattering. *Geophysical Research Letters*, *38*(16).

Chen, L., Thorne, R. M., Shprits, Y., & Ni, B. (2013). An improved dispersion relation for parallel propagating electromagnetic waves in warm plasmas: Application to electron scattering. *Journal of Geophysical Research: Space Physics*, *118*(5), 2185-2195. doi: 10.1002/jgra.50260

Clausen, L. B. N., Baker, J. B. H., Ruohoniemi, J. M., & Singer, H. J. (2011). Emic waves observed at geosynchronous orbit during solar minimum: Statistics and excitation. *Journal of Geophysical Research: Space Physics*, *116*(A10). doi: 10.1029/2011JA016823

Clilverd, M. A., Duthie, R., Hardman, R., Hendry, A. T., Rodger, C. J., Raita, T., . . . Milling, D. K. (2015). Electron precipitation from emic waves: A case study from 31 may 2013. *Journal of Geophysical Research: Space Physics*, *120*(5), 3618-3631. doi: 10.1002/2015JA021090

Cornwall, J. M. (1965, Jan). Cyclotron instabilities and electromagnetic emission in the ultra low frequency and very low frequency ranges. *Journal of Geophysical Research*, *70*, 61.

Cornwall, J. M., Coroniti, F. V., & Thorne, R. M. (1970, Jan). Turbulent loss of ring current protons. *Journal of Geophysical Research*, *75*, 4699. doi: 10.1029/JA075i025p04699

Douma, E., Rodger, C. J., Clilverd, M. A., Hendry, A. T., Engebretson, M. J., & Lessard, M. R. (2018). Comparison of relativistic microburst activity seen by sampex with ground-based wave measurements at halley, antarctica. *Journal of Geophysical Research: Space Physics*, *123*(2), 1279-1294. doi: 10.1002/2017JA024754

Engebretson, M. J., Posch, J. L., Wygant, J. R., Kletzing, C. A., Lessard, M. R., Huang, C.-L., . . . Shiokawa, K. (2015). Van allen probes, noaa, goes, and ground observations of an intense emic wave event extending over 12 h in magnetic local time. *Journal of Geophysical Research: Space Physics*, *120*(7), 5465-5488. doi: 10.1002/2015JA021227

Evans, D., & Greer, M. (2000). Polar orbiting environmental satellite space environment monitor-2 instrument descriptions and archive data documentation. *Tech. rep., National Atmospheric and Oceanic Administration.*

Fraser, B. J., Grew, R. S., Morley, S. K., Green, J. C., Singer, H. J., Loto'aniu, T. M., & Thomsen, M. F. (2010, May). Storm time observations of electromagnetic ion cyclotron waves at geosynchronous orbit: GOES results. *Journal of Geophysical Research*, *115*, 05208. doi: 10.1029/2009JA014516

Fraser, B. J., Loto'aniu, T. M., & Singer, H. J. (2006, Jan). Electromagnetic ion cyclotron waves in the magnetosphere. In K. Takahashi, P. J. Chi, R. E. Denton, & R. L. Lysak (Eds.), *Magnetospheric ULF waves: Synthesis and new directions. geophysical monograph.* (Vol. 169, p. 195).

Fraser, B. J., & Nguyen, T. S. (2001). Is the plasmapause a preferred source region of electromagnetic cyclotron waves in the magnetosphere. *Journal of Atmospheric and Solar-Terrestrial Physics*, *63*, 1225–1247.

Fraser, B. J., Singer, H. J., Hughes, W. J., Wygant, J. R., Anderson, R. R., & Hu, Y. D. (1996, Jul). CRRES poynting vector observations of electromagnetic ion cyclotron waves near the plasmapause. *Journal of Geophysical Research*, *101*, 15331–15343. doi: 10.1029/95JA03480

Fritz, T. A., Alothman, M., Bhattacharjya, J., Matthews, D. L., & Chen, J. (2003). Butterfly pitch-angle distributions observed by isee-1. *Planetary and Space Science*, *51*(3), 205 - 219. doi: 10.1016/S0032-0633(02)00202-7

Funsten, H. O., Skoug, R. M., Guthrie, A. A., MacDonald, E. A., Baldonado, J. R., Harper, R. W., … Chen, J. (2013, March). Helium, Oxygen, Proton, and Electron (HOPE) Mass Spectrometer for the Radiation Belt Storm Probes Mission. *Space Sci. Rev.*. doi: 10.1007/s11214-013-9968-7

Galand, M., & Evans, D. (2000, 01). Radiation damage of the proton meped detector on poes(tiros/noaa) satellites. *NOAA Technical Report*.

Gamble, R. J., Rodger, C. J., Clilverd, M. A., Sauvaud, J.-A., Thomson, N. R., Stewart, S. L., … Berthelier, J.-J. (2008). Radiation belt electron precipitation by man-made vlf transmissions. *Journal of Geophysical Research: Space Physics*, *113*(A10). doi: 10.1029/2008JA013369

Gannon, J. L., Li, X., & Heynderickx, D. (2007, Apr). Pitch angle distribution analysis of radiation belt electrons based on combined release and radiation effects satellite medium electrons a data. *Journal of Geophysical Research*, *112*, 05212. doi:

10.1029/2005JA011565

Gendrin, R. (1983). Wave particle interactions as an energy transfer mechanism between different particle species. *Space Science Reviews*. doi: 10.1007/BF00175283

Halford, A. J., Fraser, B. J., & Morley, S. K. (2010, Dec). EMIC wave activity during geomagnetic storm and nonstorm periods: CRRES results. *Journal of Geophysical Research*, *115*, 12248. doi: 10.1029/2010JA015716

Halford, A. J., Fraser, B. J., Morley, S. K., Elkington, S. R., & Chan, A. A. (2016). Dependence of emic wave parameters during quiet, geomagnetic storm, and geomagnetic storm phase times. *Journal of Geophysical Research: Space Physics*, *121*(7), 6277–6291. (2016JA022694) doi: 10.1002/2016JA022694

Hendry, A. T., Rodger, C. J., & Clilverd, M. A. (2017). Evidence of sub-mev emic-driven electron precipitation. *Geophysical Research Letters*, *44*(3), 1210-1218. doi: 10.1002/2016GL071807

Hendry, A. T., Santolik, O., Kletzing, C. A., Rodger, C. J., Shiokawa, K., & Baishev, D. (2019). Multi-instrument observation of nonlinear emic-driven electron precipitation at sub–mev energies. *Geophysical Research Letters*, *46*(13), 7248-7257. doi: 10.1029/2019GL082401

Horne, R. B., Lam, M. M., & Green, J. C. (2009, Oct). Energetic electron precipitation from the outer radiation belt during geomagnetic storms. *Geophysical Research Letters*, *36*, 19104. doi: 10.1029/2009GL040236

Horne, R. B., & Thorne, R. M. (1993, Jun). On the preferred source location for the convective amplification of ion cyclotron waves. *Journal of Geophysical Research*, *98*, 9233.

Horne, R. B., & Thorne, R. M. (1997). Wave heating of he+ by electromagnetic ion cyclotron waves in the magnetosphere: Heating near the h+-he+ bi-ion resonance frequency. *Journal of Geophysical Research: Space Physics*, *102*(A6), 11457-11471. doi: https://doi.org/10.1029/97JA00749

Horne, R. B., & Thorne, R. M. (1998). Potential waves for relativistic electron scattering and stochastic acceleration during magnetic storms. *Geophysical Research Letters*, *25*(15), 3011–3014. doi: 10.1029/98GL01002

Hyun, K., Kim, K.-H., Lee, E., Kwon, H.-J., Lee, D.-H., & Jin, H. (2014). Loss of geosynchronous relativistic electrons by emic wave scattering under quiet geomagnetic conditions. *Journal of Geophysical Research: Space Physics*, *119*(10), 8357-8371. doi: 10.1002/2014JA020234

Jacobs, J. A., Kato, Y., Matsushita, S., & Troitskaya, V. A. (1964, Jan). Classification of geomagnetic micropulsations. *Journal of Geophysical Research*, *69*, 180. doi: 10.1029/JZ069i001p00180

Jordanova, V. K., Kozyra, J. U., & Nagy, A. F. (1996, Sep). Effects of heavy ions on the quasi-linear diffusion coefficients from resonant interactions with electromagnetic ion cyclotron waves. *Journal of Geophysical Research*, *101*, 19771. doi: 10.1029/96JA01641

Jun, C.-W., Yue, C., Bortnik, J., Lyons, L. R., Nishimura, Y., Kletzing, C., … Spence, H. (2019). A statistical study of emic waves associated with and without energetic particle injection from the magnetotail. *Journal of Geophysical Research: Space Physics*, *124*(1), 433-450. doi: 10.1029/2018JA025886

Keika, K. (2013, July). Global characteristics of electromagnetic ion cyclotron waves: Occurrence rate and its storm dependence. *Journal of Geophysical Research: Space Physics*, *118*(7), 4135–4150.

Kennel, C. F. (1969, Jan). Consequences of a magnetospheric plasma. *Review of Geophysics and Space Physics*, *7*, 379. doi: 10.1029/RG007i001p00379

Kennel, C. F., & Petscheck, H. E. (1966, Jan). Limit on stably trapped particle fluxes. *Journal of Geophysical Research*, *71*, 1.

Kletzing, C. A., Kurth, W. S., Acuna, M., MacDowall, R. J., Torbert, R. B., Averkamp, T., … Tyler, J. (2013, November). The Electric and Magnetic Field Instrument Suite and Integrated Science (EMFISIS) on RBSP. *Space Science Reviews*, *179*(1), 127–181.

Kurth, W. S., De Pascuale, S., Faden, J. B., Kletzing, C. A., Hospodarsky, G. B., Thaller, S., & Wygant, J. R. (2015). Electron densities inferred from plasma wave spectra obtained by the waves instrument on van allen probes. *Journal of Geophysical Research: Space Physics*, *120*(2), 904-914. doi: 10.1002/2014JA020857

Lee, J. H., & Angelopoulos, V. (2014b). Observations and modeling of emic wave properties in the presence of multiple ion species as function of magnetic local time. *Journal of Geophysical Research: Space Physics*, *119*(11), 8942-8970. doi: 10.1002/2014JA020469

Li, J., Ni, B., Ma, Q., Xie, L., Pu, Z., Fu, S., … Summers, D. (2016). Formation of energetic electron butterfly distributions by magnetosonic waves via landau resonance. *Geophysical Research Letters*, *43*(7), 3009-3016. doi: 10.1002/2016GL067853

Li, X., Millan, R., Hudson, M., Woodger, L., Smith, D., Chen, Y., … Spence, H. (2014, December). Investigation of EMIC wave scattering as the cause for the BARREL 17 January 2013 relativistic electron precipitation event: A quantitative comparison of simulation with observations. *Geophysical Research Letters*, *41*(24), 8722–8799.

Liu, K., Lemons, D. S., Winske, D., & Gary, S. P. (2010). Relativistic electron scattering by electromagnetic ion cyclotron fluctuations: Test particle simulations. *Journal of Geophysical Research: Space Physics*, *115*(A4). doi: https://doi.org/10.1029/2009JA014807

Ma, Q., Li, W., Thorne, R. M., Ni, B., Kletzing, C. A., Kurth, W. S., … Angelopoulos, V. (2015). Modeling inward diffusion and slow decay of energetic electrons in the earth's outer radiation belt. *Geophysical Research Letters*, *42*(4), 987-995. doi: 10.1002/2014GL062977

Mauk, B. H., Fox, N. J., Kanekal, S. G., Kessel, R. L., Sibeck, D. G., & Ukhorskiy, A. (2012, Sep). Science objectives and rationale for the Radiation Belt Storm Probes Mission. *Space Science Reviews*, 76. ((c) 2012: The Author(s)) doi: 10.1007/s11214-012-9908-y

McIlwain, C. (1961). Coordinates for mapping the distribution of magnetically trapped particles. *Journal of Geophysical research*, *66*, 3681.

Meier, M. M., Belian, R. D., Cayton, T. E., Christensen, R. A., Garcia, B., Grace, K. M., … Reeves, G. D. (1996). The energy spectrometer for particles (esp): Instrument description and orbital performance. *AIP Conference Proceedings*, *383*(1), 203-210. doi: 10.1063/1.51533

Meredith, N., Thorne, R., Horne, R., Summers, D., Fraser, B., & Anderson, R. (2003, Jan). Statistical analysis of relativistic electron energies for cyclotron resonance with EMIC waves observed on CRRES. *Journal of Geophysical Research*, *108*. doi: 10.1029/2002JA009700

Millan, R., & Thorne, R. M. (2007, Jan). Review of radiation belt relativistic electron losses. *Journal of Atmospheric and Terrestrial Physics*, *69*, 362-377.

Millan, R. M., Yando, K. B., Green, J. C., & Ukhorskiy, A. Y. (2010). Spatial distribution of relativistic electron precipitation during a radiation belt depletion event. *Geophysical Research Letters*, *37*(20). doi: 10.1029/2010GL044919

Min, K., Lee, J., Keika, K., & Li, W. (2012, May). Global distribution of emic waves derived from themis observations. *Journal of Geophysical Research*, *117*(A5), A05219. doi: 10.1029/2012JA017515

Miyoshi, Y., & Kataoka, R. (2005). Ring current ions and radiation belt electrons during geomagnetic storms driven by coronal mass ejections and corotating interaction regions. *Geophysical Research Letters*, *32*(21). doi: 10.1029/2005GL024590

Miyoshi, Y., Sakaguchi, K., Shiokawa, K., Evans, D., Albert, J., Connors, M., & Jordanova, V. (2008, Nov). Precipitation of radiation belt electrons by EMIC waves, observed from ground and space. *Geophysical Research Letters*, *35*, 23101. doi: 10.1029/2008GL035727

Morley, S. K., Ables, S. T., Sciffer, M. D., & Fraser, B. J. (2009, Sep). Multipoint observations of Pc1-2 waves in the afternoon sector. *Journal of Geophysical Research*, *114*(A9), A09205. doi: 10.1029/2009JA014162

Morley, S. K., Friedel, R. H. W., Spanswick, E. L., Reeves, G. D., Steinberg, J. T., Koller, J., … Noveroske, E. (2010, May). Dropouts of the outer electron radiation belt in response to solar wind stream interfaces: global positioning system observations. *Proceedings of the Royal Society A: Mathematical, Physical and Engineering Sciences*, 1–23. doi: 10.1098/rspa.2010.0078

Olson, W. P., & Pfitzer, K. A. (1982, Aug). A dynamic model of the magnetospheric magnetic and electric fields for July 29, 1977. *Journal of Geophysical Research*, *87*, 5943. doi: 10.1029/JA087iA08p05943

Omura, Y., & Zhao, Q. (2012). Nonlinear pitch angle scattering of relativistic electrons by emic waves in the inner magnetosphere. *Journal of Geophysical Research: Space Physics*, *117*(A8). doi: 10.1029/2012JA017943

Omura, Y., & Zhao, Q. (2013, August). Relativistic electron microbursts due to nonlinear pitch angle scattering by EMIC triggered emissions. *Journal of Geophysical Research: Space Physics*, *118*(8), 5008–5020.

Paulikas, G., & Blake, J. (1979). Effects of the solar wind on magnetospheric dynamics: Energetic electrons at the synchronous orbit. In *Quantitative modeling of magnetospheric processes* (p. 180-202). American Geophysical Union (AGU). doi: 10.1029/GM021p0180

Pickett, J. S., Grison, B., Omura, Y., Engebretson, M. J., Dandouras, I., Masson, A., ... Constantinescu, D. (2010, May). Cluster observations of EMIC triggered emissions in association with Pc1 waves near Earth's plasmapause. *Geophysical Research Letters*, *37*, 09104. doi: 10.1029/2010GL042648

Qin, M., Hudson, M., Li, Z., Millan, R., Shen, X., Shprits, Y., ... Kletzing, C. (2019). Investigating loss of relativistic electrons associated with emic waves at low l values on 22 june 2015. *Journal of Geophysical Research: Space Physics*, *124*(6), 4022-4036. doi: 10.1029/2018JA025726

Qin, M., Hudson, M., Millan, R., Woodger, L., & Shen, X. (2020). Statistical dependence of emic wave scattering on wave and plasma parameters. *Journal of Geophysical Research: Space Physics*, *125*(4), e2020JA027772. doi: 10.1029/2020JA027772

Reeves, G. D. (1998, Jun). Relativistic electrons and magnetic storms: 1992-1995. *Geophysical Research Letters*, *25*, 1817. doi: 10.1029/98GL01398

Reeves, G. D., McAdams, K. L., Friedel, R. H. W., & O'Brien, T. P. (2003, May). Acceleration and loss of relativistic electrons during geomagnetic storms. *Geophysical Research Letters*, *30*, 36. doi: 10.1029/2002GL016513

Remya, B., Sibeck, D. G., Halford, A. J., Murphy, K. R., Reeves, G. D., Singer, H. J., ... Thaller, S. A. (2018). Ion injection triggered emic waves in the earth's magnetosphere. *Journal of Geophysical Research: Space Physics*, *123*(6), 4921-4938. doi:

10.1029/2018JA025354

Remya, B., Sibeck, D. G., Ruohoniemi, J. M., Kunduri, B., Halford, A. J., Reeves, G. D., & Reddy, R. V. (2020). Association between emic wave occurrence and enhanced convection periods during ion injections. *Geophysical Research Letters*, *47*(3), e2019GL085676. doi: 10.1029/2019GL085676

Ripoll, J.-F., Claudepierre, S. G., Ukhorskiy, A. Y., Colpitts, C., Li, X., Fennell, J. F., & Crabtree, C. (2020). Particle dynamics in the earth's radiation belts: Review of current research and open questions. *Journal of Geophysical Research: Space Physics*, *125*(5), e2019JA026735. doi: 10.1029/2019JA026735

Rodger, C., Clilverd, M., Green, J., & Lam, M. M. (2010). Use of POES SEM-2 observations to examine radiation belt dynamics and energetic electron precipitation into the atmosphere. *Journal of Geophysical Research: Space Physics*, *115*(A4). doi: 10.1029/2008JA014023

Rodger, C. J., Clilverd, M. A., Seppälä, A., Thomson, N. R., Gamble, R. J., Parrot, M., … Ulich, T. (2010, Nov). Radiation belt electron precipitation due to geomagnetic storms: Significance to middle atmosphere ozone chemistry. *Journal of Geophysical Research*, *115*, 11320. doi: 10.1029/2010JA015599

Rodger, C. J., Hendry, A. T., Clilverd, M. A., Kletzing, C. A., Brundell, J. B., & Reeves, G. D. (2015). High-resolution in situ observations of electron precipitation-causing emic waves. *Geophysical Research Letters*, *42*(22), 9633-9641. doi: 10.1002/2015GL066581

Sandanger, Søraas, F., Aarsnes, K., Oksavik, K., & Evans, D. S. (2007, Dec). Loss of relativistic electrons: Evidence for pitch angle scattering by electromagnetic ion cyclotron waves excited by unstable ring current protons. *Journal of Geophysical Research*, *112*, 12213. doi: 10.1029/2006JA012138

Sandanger, M. I., Søraas, F., Sørbø, M., Aarsnes, K., Oksavik, K., & Evans, D. S. (2009, Jun). Relativistic electron losses related to emic waves during cir and cme storms. *Journal of Atmospheric and Solar-Terrestrial Physics*, *71*(10-11), 1126–1144. doi: 10.1016/j.jastp.2008.07.006

Sandanger, M. I., Ødegaard, L.-K. G., Nesse Tyssøy, H., Stadsnes, J., Søraas, F., Oksavik, K.,

& Aarsnes, K. (2015). In-flight calibration of noaa poes proton detectors—derivation of the meped correction factors. *Journal of Geophysical Research: Space Physics*, *120*(11), 9578-9593. doi: 10.1002/2015JA021388

Selesnick, R. S., & Blake, J. B. (2002). Relativistic electron drift shell splitting. *Journal of Geophysical Research: Space Physics*, *107*(A9), SMP 27-1-SMP 27-10. doi: 10.1029/2001JA009179

Selesnick, R. S., Tu, W., Yando, K., Millan, R. M., & Redmon, R. J. (2020). Poes/meped angular response functions and the precipitating radiation belt electron flux. *Journal of Geophysical Research: Space Physics*, *125*(9), e2020JA028240. doi: https://doi.org/10.1029/2020JA028240

Shprits, Y. Y., Chen, L., & Thorne, R. M. (2009, Mar). Simulations of pitch angle scattering of relativistic electrons with MLT-dependent diffusion coefficients. *Journal of Geophysical Research*, *114*, 03219. doi: 10.1029/2008JA013695

Shprits, Y. Y., Drozdov, A. Y., Spasojevic, M., Kellerman, A. C., Usanova, M. E., Engebretson, M. J., … Aseev, N. A. (2016). Wave-induced loss of ultra-relativistic electrons in the van allen radiation belts. *Nature Communications*. doi: 10.1038/ncomms12883

Shprits, Y. Y., Kellerman, A., Aseev, N., Drozdov, A. Y., & Michaelis, I. (2017). Multi-mev electron loss in the heart of the radiation belts. *Geophysical Research Letters*, *44*(3), 1204-1209. doi: 10.1002/2016GL072258

Silin, I., Mann, I., Sydora, R., Summers, D., & Mace, R. (2011). Warm plasma effects on electromagnetic ion cyclotron wave mev electron interactions in the magnetosphere. *J. Geophys. Res.*, *116*(A5). doi: doi:10.1029/2010JA016398

Spasojević, M., Frey, H. U., Thomsen, M. F., Fuselier, S. A., Gary, S. P., Sandel, B. R., & Inan, U. S. (2004, Feb). The link between a detached subauroral proton arc and a plasmaspheric plume. *Geophysical Research Letters*, *31*, 04803. doi: 10.1029/2003GL018389

Spasojevic, M., & Fuselier, S. A. (2009, Dec). Temporal evolution of proton precipitation associated with the plasmaspheric plume. *Journal of Geophysical Research*, *114*, 12201. doi: 10.1029/2009JA014530

Spence, H. E., Reeves, G. D., Baker, D. N., Blake, J. B., Bolton, M., Bourdarie, S., … Thorne, R. M. (2013). Science Goals and Overview of the Radiation Belt Storm Probes (RBSP) Energetic Particle, Composition, and Thermal Plasma (ECT) Suite on NASA‘s Van Allen Probes Mission. *Space Science Reviews*. doi: $10.1007/978-1-4899-7433-4_10$

Summers, D., Ni, B., & Meredith, N. (2007b, Jan). Timescales for radiation belt electron acceleration and loss due to resonate wave-particle interactions: 2. evaluation for VLF chorus, ELF hiss, and electromagnetic ion cyclotron waves. *Journal of Geophysical Research*, *112, A04207*.

Summers, D., Ni, B., & Meredith, N. P. (2007a). Timescales for radiation belt electron acceleration and loss due to resonant wave-particle interactions: 1. Theory. *Journal of Geophysical Research: Space Physics (1978–2012)*, *112*(A4), A04206.

Summers, D., & Thorne, R. (2003, Jan). Relativistic electron pitch-angle scattering by electromagnetic ion cyclotron waves during geomagnetic storms. *Journal of Geophysical Research*, *108*, 1143.

Summers, D., Thorne, R. M., & Xiao, F. (1998, Jan). Relativistic theory of wave-particle resonant diffusion with application to electron acceleration in the magnetosphere. *Journal of Geophysical Research*, *103*, 20487-20500.

Thorne, & Kennel, C. F. (1971). Relativistic electron precipitation during magnetic storm main phase. *Journal of Geophysical Research: Space Physics*, *76*(1).

Thorne, Smith, K. J., & Church, F. S. R. (1974). Intensity variation of elf hiss and chorus during isolated substorms. *Geophysical Research Letters*, *1*(5), 193-196. doi: 10.1029/GL001i005p00193

Tsurutani, B. T., & Lakhina, G. S. (1997, Nov). Some basic concepts of wave-particle interactions in collisionless plasmas. *Reviews of Geophysics*, *35*, 491. doi: 10.1029/97RG02200

Turner, D., Angelopoulos, V., & Shprits…, Y. (2012, May). Radial distributions of equatorial phase space density for outer radiation belt electrons. *Geophysical Research Letters*, *39*. doi: 10.1029/2012GL051722

Ukhorskiy, A. Y., Shprits, Y. Y., Anderson, B. J., Takahashi, K., & Thorne, R. M. (2010, May). Rapid scattering of radiation belt electrons by storm-time EMIC waves. *Geophysical Research Letters*, *37*, 09101. doi: 10.1029/2010GL042906

Usanova, M. E., Drozdov, A., Orlova, K., Mann, I. R., Shprits, Y., Robertson, M. T., ... Wygant, J. (2014). Effect of EMIC waves on relativistic and ultra relativistic electron populations: Ground Based and Van Allen Probes Observations. *Geophys. Res. Lett*, *41*. doi: 10.1002/2013GL059024

Van Allen, J. A., & Frank, L. A. (1959). Radiation around the earth to a radial distance of 107,400 km. *Nature*, *183*, 430–434. doi: 10.1038/183430a0

Vette, J. I. (1991, Nov). The ae-8 trapped electron model environment. *National Space Science Data Center/WDC-A-RS-91-24*.

Wang, D., Yuan, Z., Yu, X., Deng, X., Zhou, M., Huang, S., ... Wygant, J. R. (2015). Statistical characteristics of emic waves: Van allen probe observations. *Journal of Geophysical Research: Space Physics*, *120*(6), 4400-4408. doi: 10.1002/2015JA021089

Wang, G., Su, Z., Zheng, H., Wang, Y., Zhang, M., & Wang, S. (2017). Nonlinear fundamental and harmonic cyclotron resonant scattering of radiation belt ultrarelativistic electrons by oblique monochromatic emic waves. *Journal of Geophysical Research: Space Physics*, *122*(2), 1928-1945. doi: 10.1002/2016JA023451

Wang, H., He, Y., Lühr, H., Kistler, L., Saikin, A., Lund, E., & Ma, S. (2019). Storm time EMIC waves observed by swarm and van allen probe satellites. *Journal of Geophysical Research: Space Physics*, *124*(1), 293-312. doi: https://doi.org/10.1029/2018JA026299

Williams, D. J., & Smith, A. M. (1965). Daytime trapped electron intensities at high latitudes at 1100 kilometers. *Journal of Geophysical Research (1896-1977)*, *70*(3), 541-556. doi: 10.1029/JZ070i003p00541

Yahnin, A. G., Yahnina, T. A., Semenova, N. V., Gvozdevsky, B. B., & Pashin, A. B. (2016). Relativistic electron precipitation as seen by noaa poes. *Journal of Geophysical Research: Space Physics*, *121*(9), 8286-8299. doi: 10.1002/2016JA022765

Yando, K., Millan, R. M., Green, J. C., & Evans, D. S. (2011). A monte carlo simulation of the noaa poes medium energy proton and electron detector instrument. *Journal of Geophysical Research: Space Physics*, *116*(A10). doi: 10.1029/2011JA016671

Yuan, Z., Deng, X., Lin, X., Pang, Y., Zhou, M., Décréau, P. M. E., … Wang, J. (2010, Apr). Link between EMIC waves in a plasmaspheric plume and a detached sub-auroral proton arc with observations of Cluster and IMAGE satellites. *Geophysical Research Letters*, *37*, 07108. doi: 10.1029/2010GL042711

Zhang, X.-J., Li, W., Ma, Q., Thorne, R. M., Angelopoulos, V., Bortnik, J., … Fennell, J. F. (2016). Direct evidence for emic wave scattering of relativistic electrons in space. *Journal of Geophysical Research: Space Physics*, *121*(7), 6620-6631. doi: 10.1002/2016JA022521